EFFECTS OF RADIATION ON WASTE WATER CONTAINING ORGANIC POLLUTANTS

By

JHIMLI PAUL GUIN

CHEM01201104008

Bhabha Atomic Research Centre, Mumbai, INDIA

A thesis submitted to the

Board of Studies in Chemical Sciences

In partial fulfillment of requirements

for the Degree of

DOCTOR OF PHILOSOPHY

of

HOMI BHABHA NATIONAL INSTITUTE

February, 2015

Homi Bhabha National Institute

Recommendations of the Viva Voce Committee

As members of the Viva Voce Committee, we certify that we have read the dissertation prepared by Smt. Jhimli Paul Guin entitled "*Effects of Radiation on Waste Water Containing Organic Pollutants*" and recommend that it may be accepted as fulfilling the thesis requirement for the award of Degree of Doctor of Philosophy.

External Examiner - Prof. Rakesh Kumar	Date:	30.7.15
Chairman - Prof. K.L. Ramakumar	Date:	30.7.2015
Guide / Convener - Prof. Lalit Varshney	Date:	30/07/2015
Member 1 - Prof. D.B. Naik	Date:	29.7.2015
Member 2 - Prof. G.G. Pandit	Date:	30/7/2015
Member 3 - Prof. Y.K. Bhardwaj	Date:	30/07/2015

Final approval and acceptance of this thesis is contingent upon the candidate's submission of the final copies of the thesis to HBNI.

I hereby certify that I have read this thesis prepared under my direction and recommend that it may be accepted as fulfilling the thesis requirement.

Date: 11/8/2015

Place: Mumbai

(Lalit Varshney)

STATEMENT BY AUTHOR

This dissertation has been submitted in partial fulfillment of requirements for an advanced degree at Homi Bhabha National Institute (HBNI) and is deposited in the Library to be made available to borrowers under rules of the HBNI.

Brief quotations from this dissertation are allowable without special permission, provided that accurate acknowledgement of source is made. Requests for permission for extended quotation from or reproduction of this manuscript in whole or in part may be granted by the Competent Authority of HBNI when in his or her judgment the proposed use of the material is in the interests of scholarship. In all other instances, however, permission must be obtained from the author.

(Jhimli Paul Guin)

DECLARATION

I, hereby declare that the investigation presented in the thesis has been carried out by me. The work is original and has not been submitted earlier as a whole or in part for a degree / diploma at this or any other Institution / University.

(Jhimli Paul Guin)

List of Publications Arising from the Thesis

Journal

1. "Evaluation of efficiencies of radiolysis, photocatalysis and ozonolysis of simulated textile dye waste water", Jhimli Paul Guin, Y.K. Bhardwaj, D.B. Naik, Lalit Varshney; *RSC Advances*, **2014**, 4, 53921-53926.

2. "An insight into the effective advanced oxidation process for treatment of simulated textile dye waste water", Jhimli Paul Guin, D.B. Naik, Y.K. Bhardwaj, Lalit Varshney; *RSC Advances*, **2014**, 4, 39941-39947.

3. "Studies on oxidative radiolysis of ibuprofen in presence of potassium persulfate", Jhimli Paul (Guin), D.B. Naik, Y.K. Bhardwaj, Lalit Varshney; *Radiation Physics and Chemistry*, **2014**, 100, 38 - 44.

4. "An insight into the influence of low dose irradiation pretreatment on the microbial decolouration and degradation of Reactive Red - 120 dye"; Jhimli Paul, A.A. Kadam, S.P. Govindwar, Pranaw Kumar, Lalit Varshney; *Chemosphere*, **2013**, 90, 1348-1358.

5. "Radiolytic degradation of 4-nitrophenol in aqueous solutions: Pulse and steady state radiolysis study"; J. Biswal, Jhimli Paul, D.B. Naik, S.K. Sarkar, S. Sabharwal, *Radiation Physics and Chemistry*, **2013**, 85, 161-166.

6. "Decoloration and degradation of Reactive Red -120 dye by electron beam irradiation in aqueous solution", Jhimli Paul, K.P. Rawat, K.S.S. Sarma, S. Sabharwal; *Applied Radiation and Isotopes*, **2011**, 69, 982-987.

7. "High energy induced decoloration and mineralization of Reactive Red-120 dye in aqueous solution: A steady state and pulse radiolysis study", Jhimli Paul, D.B. Naik, S. Sabharwal; *Radiation Physics and Chemistry,* **2010**, 79, 770-776.

8. "One electron oxidation and reduction of Reactive Red -120 dye in aqueous solution: A steady state and pulse radiolysis study", Jhimli Paul, D.B. Naik, S.K. Sarkar, S. Sabharwal; *Radiation Physics and Chemistry*, **2010**, 79, 1225-1233.

Paper Presentations in International Conferences

1. "Advanced oxidation process on simulated reactive dye waste water"; Jhimli Paul Guin, D.B. Naik, Y.K. Bhardwaj, L. Varshney; Proceedings of AOP-2014, September 25-28, 2014, Munnar, Kerala, p. 84.

2. "Gamma radiolysis of synthetic azo dye mixture"; Jhimli Paul Guin, Y.K. Bhardwaj, L. Varshney; Proceedings of AOP-2014, September 25-28, 2014, Munnar, Kerala, p 85.

3. "Combined radiation and biological treatment for the decolouration of Reactive Red-120 dye"; J. Paul, A.A. Kadam, S.P. Govindwar, S. Sabharwal, L. Varshney; Proceedings of TSRP-2012, January 4-7, 2012, Mumbai, p. 146.
   [Received Harimohan Memorial Award for Best Poster Presentation in this international conference].

4. "Enhanced degradation of Reactive Red-120 dye using high energy electron beam irradiation"; Jhimli Paul, K.P. Rawat, K.S.S. Sarma, S. Sabharwal; 5th NAARRI International Conference on Radioisotopes and Radiation in Industry NIC 2010, December (2010), RP-8.

5. “Pulse and Steady State Radiolysis of Reactive Red-120”; Jhimli Paul, D.B. Naik, S. Sabharwal; Proceedings of 3rd Asia Pacific Symposium on Radiation Chemistry (APSRC-2010) and DAE BRNS 10th Biennial Trombay Symposium on Radiation & Photochemistry (TSRP-2010), Vol. 2 September, (2010), p. 15.

DEDICATIONS

This thesis is dedicated to

my husband

Saurav K. Guin

ACKNOWLEDGEMENTS

This thesis owes its existence to the help, support, and inspiration of many people. I would like to thank my guide and mentor, Prof. Lalit Varshney for his valuable guidance, support and encouragement during the course of this thesis work. Deepest gratitude is also due to the members of the HBNI Doctoral Committee Prof. K.L. Ramakumar, Prof. D.B. Naik, Prog G.G. Pandit and Prof. Y.K. Bhardwaj for their comments and useful suggestions for improvement in quality of the study.

Special thanks to Dr. S. Sabharwal, Shri K.S.S. Sarma, Shri K.P. Rawat, Dr. Avinash A. Kadam, Dr. S.P. Govindwar, Dr. Pranaw Kumar and Dr. Jayashree Biswal for extending their support at various stages to complete my work. I would also like to thank Mr. Mukesh Kumar for his kind support in carrying out electron beam experiments.

I express gratitude to Dr. K.A. Dubey and all other colleagues in the Radiation Research and Advanced Application Section for their wholehearted support, encouragement and co-operation. I would also like to thank my family, friends and colleagues for their constant support and encouragement.

.....*Jhimli Paul Guin*

CONTENTS

Synopsis	***i***
List of Symbols	***xi***
List of Abbreviations	***xv***
List of Figures	***xvii***
List of Tables	***xxvii***
CHAPTER 1 : Introduction	***1***
1.1. Environmental impact of organic pollutants	***3***
1.1.1. Textile dyes and their environmental concern	***3***
1.1.1.1. Classification of dyes	***3***
1.1.1.2. Discharge statistics of reactive dyes and other auxiliary chemicals in textile waste water	***6***
1.1.2. Pharmaceuticals and their environmental concerns	***7***
1.1.3. Nitrocompounds and their environmental concerns	***9***
1.2. Advanced Oxidation Processes (AOPs)	***10***
1.2.1. Radiation Technology	***11***
1.2.2. Photocatalysis	***11***
1.2.3. Ozonolysis	***12***
1.3. Interaction of High Energy Radiation with Matter	***14***
1.3.1. Gamma Radiation	***14***
1.3.1.1. Photoelectric Effect	***15***
1.3.1.2. Compton Scattering	***15***
1.3.1.3. Pair Production	***16***
1.3.2. Electrons	***16***
1.3.2.1. Elastic Collision	***17***
1.3.2.2. Inelastic Collision	***17***
1.3.2.3. Emission of Bremssstrahlung	***18***
1.3.3. Comparative radiolysis on the phase state of matters	***18***
1.3.4. Depth-dose profiles for gamma and electron beam irradiation	***19***

1.3.5. Radiation chemistry of water ***20***

1.3.6. Radicals of interest during radiolysis of water and their selective generation ***26***

CHAPTER 2 : Experimental ***29***

2.1. Linear Electron Accelerator (LINAC) ***31***

2.1.1. 7 MeV LINAC ***31***

2.1.1.1. Kinetic spectrophotometer ***32***

2.1.1.2. Analysis of the recorded signal ***32***

2.1.1.3. Corrected transient absorption spectra and molar absorptivity ***33***

2.1.1.4. Dosimetry for Pulse Radiolysis ***34***

2.1.2. 2-MeV Linear Electron Accelerator ***35***

2.1.2.1. Dosimetry of electron beam accelerator ***35***

2.1.3. 10 MeV Linear Electron Accelerator ***36***

2.2. Cobalt-60 Gamma Source [GC-5000] ***36***

2.2.1. Dosimetry for ^{60}Co Gamma Source ***37***

2.3. Chemical Oxygen Demand ***39***

2.4. Total Organic Carbon ***40***

2.5. Biological Oxygen Demand ***40***

2.6. UV-Visible spectrophotometer and pH meter ***41***

2.7. Gas chromatography mass spectrometry ***41***

2.8. High-performance liquid chromatography ***42***

2.9. Electrospray Ionization Mass Spectrometry ***42***

2.10 Fourier transformed infrared spectroscopy ***44***

2.11. Photocatalytic reactor ***44***

2.12. Ozone reactor ***45***

2.13. Chemicals and Reagents ***45***

2.14. Enzyme assay ***45***

2.14.1. Determination of laccase activity ***45***

2.14.2. Determination of tyrosinase activity ***46***

2.14.3. Determination of azoreductase activity ***46***

2.14.4. Determination of NADH-DCIP activity **46**

2.15. Method of sample preparation for the toxicity study of the treated dye solution on plants **47**

2.16. Micro-organisms and culture conditions **47**

2.17. Microbial treatment **47**

2.18. Preparation of the cell free extract **48**

CHAPTER 3 : Decolouration and Degradation of Reactive Red - 120 dye **49**

3.1. Radiolysis of aqueous solution of Reactive Red - 120 **51**

3.1.1. Structure of Reactive Red - 120 **51**

3.1.2. Radiolysis of RR-120 by Oxidising Radicals **54**

3.1.2.1. Reaction of RR-120 with Hydroxyl Radical ($^{\bullet}OH$) **54**

3.1.2.2. Reaction of RR-120 with Azide Radical ($N_3^{\bullet}$) **57**

3.1.2.3. Reaction of RR-120 with Chlorine Radical ($Cl_2^{\bullet-}$) **59**

3.1.3. Radiolysis of RR-120 by Reducing Radicals **63**

3.1.3.1. Reaction of RR-120 with Hydrated Electron (e_{aq}^-) **63**

3.1.3.2. Reaction of RR-120 with Isopropyl Radical ($(CH_3)_2C^{\bullet}OH$) **66**

3.1.3.3. Reaction of RR-120 with Formate Radical ($CO_2^{\bullet-}$) **69**

3.1.4. Radiolysis of Aerated RR-120 Solution **72**

3.1.5. Electron Beam Irradiation of Aerated RR-120 Solution **75**

3.2. Enhancement of the Biodegradability of RR-120 Solution by Radiolysis **79**

3.3. Combined Radiation and Microbial Treatment of aqueous RR-120 Solution **80**

3.3.1. Investigation on the mechanism of the decolouration and degradation in combined radiation and microbial treatment of aqueous RR-120 Solution **84**

3.3.1.1. FTIR analysis **84**

3.3.1.2. HPLC analysis **86**

3.3.1.3. ESI-MS analysis **88**

3.3.1.4. Enzyme analysis **91**

3.3.1.5. GC–MS analysis **93**

3.3.2. Discussion on the decolouration and degradation mechanisms of RR-120 for combined radiation-microbial treatment ***94***

3.4. Radiolysis of simulated textile dye waste water (STDWW) containing RR-120 ***99***

3.4.1 Decolouration and mineralization of STDWW by photocatalysis and ozonolysis ***100***

3.4.2. Decolouration and mineralization of STDWW by gamma radiolysis ***102***

3.4.3. Comparison of the process efficiencies of photocatalysis, ozonolysis and gamma radiolysis for the mineralization of STDWW. ***104***

3.4.4. Mechanism of mineralization of the components present in STDWW ***106***

3.4.5. The influence of the nature of neutralizing acid on the radiolysis of STDWW ***110***

3.4.6. Radiolysis of MSTDWW in the presence of $K_2S_2O_8$ ***112***

3.4.7. Photocatalysis of MSTDWW ***113***

3.4.8. Ozonolysis of MSTDWW ***115***

3.4.9. Comparison of the process efficiencies of radiolysis, photocatalysis, and ozonolysis for the mineralization of MSTDWW ***115***

3.4.9.1. In terms of the OCC ***115***

3.4.9.2. In terms of the cost of the energy source and other ancillary inputs ***117***

CHAPTER 4 : Decolouration of 4-Nitrophenol and Ibuprofen ***121***

4.1. Radiolysis of aqueous solution of 4-Nitrtophenol ***123***

4.1.1. Structure of 4-Nitrophenol ***123***

4.1.2. Pulse radiolysis of 4-NP ***124***

4.1.3. Steady state gamma radiolysis of 4-NP ***129***

4.2. Radiolysis of aqueous solution of Ibuprofen (IBP) ***130***

4.2.1. The variation of COD and TOC on gamma irradiation of aqueous IBP solution ***130***

4.2.2. Pulse radiolysis of IBP in the presence of radiolytically generated oxidizing species ***132***

4.2.3. Gamma radiolysis studies of IBP in presence of radiolytically generated oxidizing species ***139***

Summary ***141***

Bibliography ***145***

Synopsis

Organic pollutants are chemical compounds that contain carbon and have an adverse effect on the environment. The organic pollutants such as dyes, pesticides, surfactants, phenols etc. are resistant to the environmental degradation. The natural chemical, biological, and photolytic processes fail to degrade them. These recalcitrant organic pollutants can accumulate in the environment and do harm to animals and humans *[1]*. The anaerobic and aerobic biological processes are mostly employed for the treatment of such organic pollutants. However, these processes are slow and their treatment efficiencies are not always acceptable for the recalcitrant organic pollutants *[2]*. Conventional techniques such as adsorption, precipitation and flocculation, reverse osmosis, simply concentrates the organic pollutants from the solution phase to solid phase, which generates secondary wastes.

India with more than one billion population is a growing economy. It is essential that along with the industrial growth, environment should also be protected to the extent that it can support life without adverse effects. Water, an elixir of life, is one of the first victims of the environmental pollution. Use of water purification system in average Indian home and present quality of many other water resources are indicators of the poor quality of water for human consumption. To meet the consumption demands of water of a developing country like India, use of technologies that could treat and recycle waste water efficiently and economically need to be explored. Therefore, there is a pressing need to look for technological solutions which could efficiently and economically mitigate environmental issues related to waste water at larger scale.

Not meeting discharge limits, effluents from textile, pharmaceutical and other industries pollute water. These effluents contain not only dyes, pesticides and drugs but also several other organic contaminants. Nitroaromatic compounds are important building blocks for the large scale synthesis of pesticides, pharmaceuticals, plastics, azo dyes and explosives and pollute directly or indirectly the river and ground water. In the present study, we have chosen representative water polluting molecules namely (1) textile dye (Reactive Dye), (2) pharmaceutical drug, Ibuprofen (IBP) and (3) nitro compound, 4-nitrophenol (4-NP).

Radiation technology is gaining world over recognition as effective method to degrade varieties of organic pollutants in waste water *[3]*. Gamma radiation from isotopic source like Cobalt-60 and electron beam accelerators are generally used. In this process, energy from these sources is directly and indirectly deposited into the pollutants to degrade them. The extent of the degradation is affected by irradiation conditions and dose rate of the radiation source.

The advanced oxidation processes (AOPs), involving generation of hydroxyl radicals ($^{\bullet}OH$), are emerging out to be efficient and effective oxidation processes leading to complete degradation of organic pollutants with minimized productions of sludge, secondary waste and toxic intermediates. The fenton and photo-fenton processes *[4]*, photo-catalytic treatment *[5]*, electrochemical oxidation *[6]*, ultrasonic treatment *[7]*, combination of ozone and hydrogen peroxide *[8]* are some of the popular AOPs. Radiation technology using high energy ionizing radiation is also one of the promising AOPs, which can effectively degrade organic pollutants in aqueous solution with least secondary waste. Further, radiation technology can also be applied for the treatment of coloured and turbid solutions at room temperature.

In the present study, radiation effects on the aqueous solutions of the above mentioned organic compounds *viz.* reactive red 120 (RR-120), IBP and 4-NP have been investigated by using gamma and electron beam radiation with a primary objective of understanding their degradation and degradation mechanisms so that the process can be optimized for its effective utilization on industrial scale. Some AOPs along with irradiation were evaluated to improve overall efficiency and economics of the process. The thesis has been divided into four chapters.

Chapter 1: Introduction

This chapter has been divided into three sections.

Section 1: Environmental impact of organic pollutants

This section gives the literature review on the nature and environmental impact of the organic pollutants and other auxiliary chemicals present in waste water.

Section 2: Advanced Oxidation Processes (AOPs)

This section gives an overview of the AOPs used for the wastewater treatment. A general introduction of use of radiation technology for the treatment of the waste water is also briefly discussed in this section. The major advantages and limitations of use of radiation technology are included in this section.

Section 3: Radiation Chemistry of water

Water plays an important role in degradation of organic pollutants using radiation technology. Different types of radiation sources and fundamental reactions of radiolysis of water are discussed in this section.

Chapter 2: Experimental

The instruments and various techniques used in the present study are discussed in this chapter. It includes the brief principle and descriptions of instruments such as UV-Vis spectrophotometer, Chemical Oxygen Demand (COD) / Biological Oxygen Demand (BOD) / Total Organic Carbon (TOC) analyzer, pH meter, Fourier Transform Infra-Red (FTIR) Spectrophotometer, High Performance Liquid Chromatography (HPLC), Electron-Spray-Ionization (ESI-) and Gas-Chromatography (GC-) mass spectrometer. Methods and procedures used for gamma radiolysis, pulse radiolysis and electron beam irradiation are also described in this chapter.

Chapter 3: Decolouration and degradation of Reactive Red-120

The three sections of this chapter describe various results and discussions on irradiation of RR-120 using gamma radiation, electron beam and other AOPs such as ozonolysis and photocatalysis.

Section 1: Radiolysis of aqueous solution of Reactive Red - 120 (RR-120)

This section describes results of radiation induced decolouration and mineralization of the textile dye RR-120 on gamma radiolysis and electron beam irradiation under varying oxidizing and reducing radiolysis conditions. The mechanism of observed changes with various oxidizing and reducing radicals are explained by gamma radiolysis and pulse radiolysis experiments. Various reaction rates of the dye with these different radicals determined using pulse radiolysis are given. The bimolecular reaction rate constants were observed to be of the order of 10^{9}-10^{10} M^{-1} s^{-1}. The results of TOC determined at different doses under aerated and oxygen saturated solutions of the dye have been given. Similar studies were also carried out using electron beam irradiation. In addition, the study gives results of biodegradability which

was investigated by monitoring BOD_5/COD ratio. The biodegradability index of waste water, BOD_5/COD ratio was observed to be ≥ 0.3-0.5 indicating enhanced biodegradability of the irradiated dye solution.

Section 2: Effect of low dose pre-treatment irradiation on the microbial decolouration and degradation of Reactive Red-120 (RR-120) dye

The section deals with the results and discussions on low dose irradiation of aqueous solution of RR-120 dye combined with microbiological treatment using *Pseudomonas sp.* SUK1 under static incubation. The results indicated that there is an enhancement of biodegradation of aqueous RR-120, 150 ppm, dye solution irradiated at 0.5 and 1.0 kGy doses. The enhancement of biodegradation is attributed due to the enhanced enzymatic activity of microorganisms feeding on the fragmented dye molecules produced on irradiation. The degradation products were studied using HPLC, FTIR, ESI-MS and GC-MS. The treated dye solution tested on plants revealed that the combined radiation-microbial treatment of RR-120 did not produce any toxic effects. The results of this study indicated that combined use of radiation technology and microbial degradation is more effective and economic.

Section 3: Advanced oxidation process for treatment of simulated textile dye waste water

The real textile dye effluents not only contain dyes but also several other chemicals including surfactants, sequestering agent, pH-adjusting acids, inorganic salts etc. These auxiliary chemicals contribute to about 83% of the organic load and cause a negative impact to the aquatic lives by decreasing dissolved oxygen concentration in the water streams. A simulated textile dye waste water (STDWW) was prepared by mimicking the compositions of the dye bath used in dye industries and exposed to

different AOPs including radiation technology. This section discusses the results which indicated that it is better to use H_2SO_4 instead of acetic acid as a pH-adjusting agent for meeting stipulated discharge limits of treated waste water. Use of $K_2S_2O_8$ reduced the radiation dose requirement and brought the degraded STDWW below discharge limits of 250 ppm. The comparative results of gamma and electron beam radiolysis in the presence of $K_2S_2O_8$ with other AOPs *viz.* photocatalysis and ozonolysis in terms of oxygen-equivalent chemical-oxidation capacities (OCC) for 28% mineralization of STDWW were calculated as 0.08, 0.04, 6.29, 9.29 kg equiv. O_2 m^{-3} respectively.

The pulse radiolysis studies revealed that the favourable reaction of $SO_4^{\bullet-}$ (produced by the radiolysis of $K_2S_2O_8$) with SDBS (the most robust organic component of STDWW) producing benzyl and hydroxycyclohexadienyl type of radicals enhanced the extent of mineralization of STDWW during radiolysis in the presence of $K_2S_2O_8$.

Chapter 4: Degradation of Ibuprofen (IBP) and 4-nitrophenol (4-NP)

The two sections of this chapter describe various results and discussions on irradiation of IBP and 4-NP by using gamma radiation.

Section 1: The oxidative radiolysis of IBP in presence of $K_2S_2O_8$

This section describes results of gamma radiolysis of the aqueous solution of IBP, a model pharmaceutical compound, in the presence and absence of $K_2S_2O_8$. The extent of mineralization was investigated by measuring absorbance in the UV-visible spectra, decrease in the COD and the TOC content of aqueous IBP solution at different doses. The results indicated that gamma radiolysis, in presence of $K_2S_2O_8$, required much lesser radiation dose compared to IBP solutions without $K_2S_2O_8$ for the same extent of mineralization. Though the presence of $K_2S_2O_8$ increased the yield of the oxidizing radicals by a factor of 2.2, degradation was increased by ~5 times. The pulse radiolysis

study of IBP solutions was carried out under different radiolytic conditions to understand the mechanism of mineralization of IBP during gamma radiolysis in the presence of $K_2S_2O_8$. It was found that unlike $^{\bullet}OH$ radical, the $SO_4^{\bullet-}$ radical preferentially produced benzyl type of radicals via formation of benzene radical cation. The results concluded that the gamma radiolysis in the presence of $K_2S_2O_8$ can be one of the efficient AOPs for degradation of IBP present in aqueous solutions.

Section 2: Radiolysis of aqueous solution of 4-NP

This section describes the results of gamma radiolysis of aqueous solution of 4-NP under different radiolytic conditions. The extent of decolouration of N_2 purged 4-NP solutions containing tert-butanol at 2 kGy dose was found to be maximum. Solutions purged with N_2 alone gave minimum decolouration. The mechanisms of reactions of 4-NP with different oxidizing (*viz.* $^{\bullet}OH$, $N_3^{\bullet}$) and reducing radicals (*viz.* $(CH_3)_2C^{\bullet}OH$, e^-_{aq}) were also investigated by pulse radiolysis at pH 5.2 and 9.2. The results indicated that reaction between 4-NP and $^{\bullet}OH$ led to the formation of π-complexes, which subsequently decayed by first order process producing semiquinone radical at pH 5.2. On the other hand, the phenolate anion and the π complex were produced by the reaction between $^{\bullet}OH$ and 4-NP at pH 9.2. The formation of one electron oxidized species is also confirmed by the reaction between $N_3^{\bullet}$ radical with 4-NP at pH 5.2 and 9.2. The transient spectra of the reaction between 4-NP and $(CH_3)_2C^{\bullet}OH$ were similar to the transient spectra of the reaction between 4-NP and e^-_{aq}. The reducing nature of the electron adduct of 4-NP was studied by the electron transfer reaction with methyl viologen (MV^{2+}). The overall studies showed that gamma irradiation could be an efficient and promising method for the degradation of 4-NP in aqueous solutions.

Summary

The work carried out in this thesis indicates that radiation technology can be successfully used for degradation of organic pollutants such as RR-120 dye, ibuprofen and 4-nitrophenol present in waste water. It was observed that process efficiency and economics can be significantly improved when irradiation is done in combination with microbial degradation. Use of $K_2S_2O_8$ and H_2SO_4 was highly beneficial for reducing radiation dose requirement and achieving the discharge limits of the effluents. The increased mineralization efficiency of organic pollutants on irradiation was due to involvement of various transient species formed on irradiation of $K_2S_2O_8$ and particularly $SO_4^{\bullet-}$ and benzyl type of radicals. Considering all the factors, use of radiation technology for degradation of organic pollutants can be considered even better than other AOPs like ozonolysis and photocatalysis.

References

1. J. Pierce, Colour in textile effluents-the origins of the problem, *J. Soc. Dyers Color*, **110**, 1994, 131-133.

2. P. Frank, V. Zee, S. Villaverde, Combined anaerobic–aerobic treatment of azo dyes-A short review of bioreactor studies, *Water Res.*, **39**, 2005, 1425-1440.

3. J. Paul, D.B. Naik, S. Sabharwal, High energy induced decoloration and mineralization of Reactive Red 120 dye in aqueous solution: A steady state and pulse radiolysis study, *Radiat. Phys.Chem.*, **79**, 2010, 770-776.

4. H. Hansson, F. Kaczala, M. Marques, W. Hogland, Photo-Fenton and Fenton Oxidation of Recalcitrant Industrial Wastewater Using Nanoscale Zero-Valent Iron, *Int. J. Photoenergy*, 2012, 531076 (11 pages).

5. A.O. Ibhadon, P. Fitzpatrick, Heterogeneous Photocatalysis: Recent Advances and Applications, *Catalysts*, **3**, 2013, 189-218.

6. B.P. Chaplin, Critical review of electrochemical advanced oxidation processes for water treatment applications, *Env. Sci. Process.*, **16**, 2014, 1182-1203.

7. N.N. Mahamuni, Y.G. Adewuyi, Advanced oxidation processes (AOPs) involving ultrasound for waste water treatment: A review with emphasis on cost estimation, *Ultrason. Sonochem.*, **17**, 2010, 990-1003.

8. M. Bauman, A. Lobnik, A. Hribernik, Decolorization and Modeling of Synthetic Wastewater Using O_3 and H_2O_2/O_3 Processes, *Ozone Sci. Eng.*, **33**, 2011, 23-30.

List of Symbols

Symbol	Meaning
μ	: Linear attenuation coefficient
τ	: Cross section for photoelectic effect
σ	: Cross section for compton scattering
χ	: Cross section for pair production
β	: Ratio of velocity of light in a medium to the velocity of light in vacuum
λ	: Wavelength
ρ	: Density (in g cm^{-3}) of dosimeter solution
$\Delta\varepsilon$	: Extinction coefficient (in M^{-1} cm^{-1}) of ferric ions at the measuring wavelength
ΔA	: Observed absorbance
ΔA_D	: Change in absorbance of dosimeter solution before and after irradiation
ε_p	: Extinction coefficients of the parent molecule at a particular wavelength
ε_t	: Extinction coefficients of the transient at a particular wavelength
$(\Delta A)/G$	: Change in absorption per unit yield of the oxidant
$(\Delta OD)_{(SCN)2}^{\bullet-}$	: Change in absorbance of 10 mM SCN^- solution
$^{\bullet}H$	: Hydrogen atoms
$^{\bullet}OH$	: Hydroxyl Radical
A	: Absorbance
A_0	: Absorbance measured for unirradiated solution
A_D	: Absorbance measured for irradiated solution

A_{cell} : Area (in cm^2) of the photoreactor chamber

c : Velocities of light in vacuum

$Cl_2^{\bullet-}$: Chlorine Radical

$CO_2^{\bullet-}$: Formate Radical

C_t : Concentration of the transient produced

D : Absorbed dose per pulse

D_1 : Initial dissolved oxygen of sample dilution (in mg L^{-1})

D_2 : Final dissolved oxygen of sample dilution (in mg L^{-1})

e : Charge of the electron in electrostatic unit

E_0 : Standard reduction potential

e^-_{aq} : Hydrated electron

E_b : Binding energy of the electron

E_e : The energy of the recoil electron

E_e : Kinetic energy of electron

E_{KE} : Kinetic energy of the ejected electron

E_p : Kinetic energy of positron

E_γ : Energies of the deflected photons

E_v : Energy of the incident photon

G : Number of species formed (or destroyed) per 100 eV of the absorbed dose

G(P) : Yield (number of molecules per 100 eV) of ferric ions due to irradiation

$G_{(SCN)2}^{\bullet-}$: Yield of $SCN)_2^{\bullet-}$

G_T : Yield of radiolytic species

$HO_2^{\bullet}$: Perhydroxyl radicals

$HO_2^{\bullet}$: Perhydroxyl radical

I	: Initial activity (in Ci) of the ^{60}Co source
I_0	: Incident radiation intensity
I_1	: Intensity of the light passing to the solution before pulse
I_{abs}	: Absorbed light
I_2	: Intensity of the light transmitted to the solution after pulse
k	: Rate constant
k_φ	: The pseudo first order rate constant
L	: Length of the absorbing medium
l	: Optical path length
l_1	: Mean excitation potential of the atoms in the stopping material per cubic cm
m	: Mass of electron
m_0	: Rest mass of electron
N	: Avogadro number
N_0	: Number of atoms per cm^3 in the medium
$N_3^\bullet$	: Azide Radical
$O_2^{\bullet-}$	: Superoxide radical anions
p	: Decimal volumetric function of sample used
P	: Rated Power of the AOP system
R (in INR)	: Price of ^{60}Co source Ci^{-1}
t	: Time
$t_{1/2}$ (hour)	: Half-life of ^{60}Co
v_1	: Velocities of the bombarding electron in cm sec^{-1}
V	: Volume (in cm^3) of the photoreactor chamber
v	: Volume (in L) of MSTDWW treated in time t
v_{max}	: Maximum volume capacity (in L)

x	: Thickness of the material
Z	: Atomic number
z	: Charge on the electron
ΔA	: Relative absorbance of the products with reference to the parent absorption
$\Delta OD/G$	: Change in absorbance per unit G value
ΔOD_{λ}	: Change in absorption at any wavelength λ
ε	: Molar extinction coefficient
$\varepsilon_{(SCN)2}^{\bullet-}$	: Molar extinction coefficient of 10 mM SCN^- solution.
λ_{max}	: Wavelength at maximum absorption
S	: Stopping power (in erg g^{-1})
$(CH_3)_2C^{\bullet}OH$	: Isopropyl Radical

List of Abbreviations

Abbreviation	Meaning
4-NP	: 4-Nitrophenol
4-NPAT	: 4-Nitrophenate Anion
ABTS	: 2,2-azino-bis(3-ethylbenzothiazoline-6-sulphonic acid
AOP	: Advanced Oxidation Process
BOD_5	: Biochemical Oxygen Demand (Five-day)
C.I.	: Color Index
COD	: Chemical Oxygen Demand
COX-1	: Cyclooxygenase-1
COX-2	: Cyclooxygenase-2
CTP	: Cost(average) of Treatment Process of MSTDWW in Indian rupee
DCIP	: 2,6-dichlorophenol indophenol
DO	: Dissolved Oxygen
EB	: Electron Beam
EEC	: Electric Energy Consumed (in kWh) to degrade a contaminant in unit volume (in m^3)
ESI-MS	: Electro-Spray Ionization Mass Spectrometry
FTIR	: Fourier Transformed Infrared
GC-MS	: Gas Chromatography Mass Spectrometry
HPLC	: High-Performance Liquid Chromatography
IBP	: Ibuprofen
INR	: Indian Rupee
$K_2S_2O_8$	: Potassium Persulfate

KSCN	: Potassium Thiocyanate
LINAC	: Linear Electron Accelerator
MeV	: Million eV
MR	: Methyl Red
MSTDWW	: Modified Simulated Textile Dye Waste Water
MV^{2+}	: Methyl Viologen ion
NHE	: Normal Hydrogen Electrode
NSAID	: Non-Steroidal Anti-Inflammatory Drug
OD	: Optical Density
ppm	: Parts Per Million
R.F.	: Radio Frequency
RR-120	: Reactive Red - 120
SDBS	: Sodium Dodecyl-Benzene Sulfonate
SDS	: Sodium Dodecyl-Sulphate
STDWW	: Simulated Textile Dye Waste Water
^{t}Bu-OH	: Tertiary butanol
TOC	: Total Organic Carbon
WHO	: World Health Organization

List of Figures

Figure No.	Figure Caption	Page No.
Figure 1.1	The mechanism of cotton dyeing by reactive dye.	6
Figure 1.2	The mechanism of photocatalytic degradation of organic molecule.	12
Figure 1.3	The representation of the sequential processes of electrodeposition under the concentration and activation polarizations. Depth dose curves for irradiation of water by (a) ^{60}Co gamma radiation and (b) electron beam of (i) 1.8, (ii) 4.7 and (iii) 10.6 MeV energy.	20
Figure 1.4	Radiolysis products of water in the time scale of 10^{-16} - 10^{-7}s.	21
Figure 1.5	Distribution of ions and excited species along the track of fast primary electron and secondary electron; (*) represents the ions and radicals, (*) represents the excited species.	22
Figure 1.6	Effect of pH on the yield of the primary species during water irradiation.	24
Figure 2.1	Gamma Chamber 5000.	37
Figure 2.2	(a) Thermoreactor and (b) spectrophotometer for COD measurement.	39
Figure 2.3	Total organic carbon analyser.	40
Figure 2.4	Schematic of electrospray ionisation system.	43

Figure 2.5	*Incubated dye solution at 30 ± 2 ºC under static condition up to 96 h.*	***48***
Figure 3.1	*Azo and Hydrazone tautomeric forms of Reactive Red - 120.*	***52***
Figure 3.2	*UV-Visible spectra of aqueous solution of 40 μM RR-120 at (a) pH 7 and (b) pH 13.8.*	***52***
Figure 3.3	*Variation of OD at 450 and 550 nm of aqueous solution of 40 μM RR-120 as a function of pH*	***54***
Figure 3.4	*(a) Spectra of N_2O saturated 40 μM RR-120 solutions (at pH 7) (i) before radiolysis and after steady state radiolysis at (ii) 0.5 kGy, (iii) 1.0 kGy and (iv) 2.0 kGy. (b) ΔOD_λ and (c) transient absorption as a function of λ for N_2O saturated 95 μM RR-120 solution (at pH 7) during pulse radiolysis at pulse dose of 0.*	***55***
Figure 3.5	*Addition of $^{\bullet}OH$ to the aromatic ring of RR-120 forms cyclohexadienyl radicals, which react through disproportionation producing the dye molecule having an extra OH-group. R represents the residual part of RR-120.*	***57***
Figure 3.6	*(a) Spectra of N_2O saturated 40 μM RR-120 solutions (at pH 7) containing 20 mM NaN_3 (i) before radiolysis and after steady state radiolysis at (ii) 0.5 kGy, (iii) 1.0 kGy and (iv) 2.0 kGy. (b) ΔOD_λ and (c) transient absorption as a function of λ for N_2O saturated 100 μM RR-120 solution (at pH 7) containing 20 mM NaN_3 during pulse radiolysis at pulse dose of 0.01 kGy.*	***58***

Figure 3.7 *(a) Spectra of O_2 saturated 40 μM RR-120 solutions (at pH 1) containing 50 mM NaCl (i) before radiolysis and after steady state radiolysis at (ii) 0.5 kGy, (iii) 1.0 kGy and (iv) 2.0 kGy. (b) ΔOD_λ and (c) transient absorption as a function of λ for O_2 saturated 100 μM RR-120 solution (at pH 1) containing 50 mM NaCl during pulse radiolysis at pulse dose of 0.01 kGy.* ***60***

Figure 3.8 *Transient absorption as a function of λ for (i) O_2 saturated 100 μM RR-120 solution (at pH 1) containing 50 mM NaCl and (ii) N_2O saturated 100 μM RR-120 solution (at pH 1). Pulse dose = 0.01 kGy.* ***61***

Figure 3.9 *%decolouration of RR-120 during gamma radiolysis in presence of (i) $^{\bullet}OH$ (at pH 7), (ii) $^{\bullet}OH$ (at pH 1), (iii) $N_3^{\bullet}$ (at pH 7) and (iv) $Cl_2^{\bullet-}$ (at pH 1).* ***62***

Figure 3.10 *(a) Spectra of N_2 saturated 40 μM RR-120 solutions (at pH 7) containing 0.2 M ^{t}Bu-OH (i) before radiolysis and after steady state radiolysis at (ii) 0.05 kGy, (iii) 0.2 kGy and (iv) 0.33 kGy. (b) ΔOD_λ and (c) transient absorption as a function of λ for N_2 saturated 100 μM RR-120 solution (at pH 7) containing 0.2 M ^{t}Bu-OH during pulse radiolysis at pulse dose of 0.01 kGy.* ***64***

Figure 3.11 *The mechanism of radiolysis of RR-120 by e_{aq}^-. R represents the residual part of RR-120.* ***65***

Figure 3.12 *(a) Spectra of N_2O saturated 40 μM RR-120 solution (at pH 7) containing 0.2 M $(CH_3)_2CHOH$ (i) before radiolysis and after steady state radiolysis at (ii) 0.05 kGy, (iii) 0.2 kGy and (iv) 0.33 kGy. (b) ΔOD_λ and (c) transient absorption as a function of λ for N_2O saturated 200 μM RR-120 and 0.65 M $(CH_3)_2CHOH$ at pH 7 during pulse radiolysis at pulse dose of 0.01 kGy.* ***67***

Figure 3.13 *(a) Transient absorption as a function of λ and decay traces recorded at (b) 400 nm, (c) 560 nm and (d) 660 nm for the reaction of RR-120 with (i) e^-_{aq} and (ii) $(CH_3)_2C^\bullet OH$.* ***68***

Figure 3.14 *(a) Spectra of N_2O saturated 100 μM RR-120 solution (at pH 7) containing 50 mM HCOONa (i) before radiolysis and after steady state radiolysis at (ii) 0.05 kGy, (iii) 0.2 kGy and (iv) 0.33 kGy. (b) ΔOD_λ and (c) transient absorption as a function of λ for N_2O saturated 100 μM RR-120 and 50 mM $(CH_3)_2CHOH$ at pH 7 during pulse radiolysis at pulse dose of 0.01 kGy.* ***70***

Figure 3.15 *%decolouration of 40 μM RR-120 during gamma radiolysis in presence of (i) e^-_{aq}, (ii) $(CH_3)_2C^\bullet OH$ and (iii) $CO_2^{\bullet-}$ at pH 1.* ***71***

Figure 3.16 *(a) Spectra of (a) aerated (b) O_2 saturated and (c) N_2 saturated 40 μM RR-120 solutions (at pH 7) (i) before radiolysis and after steady state radiolysis at (ii) 0.5 kGy, (iii) 1.0 kGy and (iv) 2.0 kGy.* ***73***

Figure 3.17 *% decolouration of 40 μM RR-120 solution at different doses for air, O_2, N_2, ^{t}Bu-OH contained N_2 purged and N_2O saturated systems* ***74***

Figure 3.18 *% TOC removal of (a) aerated and (b) oxygen saturated 20 μM RR-120 solutions (at pH 7) during the steady state gamma radiolysis.* ***75***

Figure 3.19 *(a) Absorbance spectra of 68 μM RR-120 at pH 7 (i) before radiolysis and after electron beam irradiation with 2 MeV beam energy for (ii) 1.5 kGy, (iii) 2.5 kGy, (iv) 5.0 kGy and (v) 10.0 kGy dose. (b) % decolouration of (i) 68 μM, (ii) 100 μM and (iii) 130 μM of RR-120 solution at pH 7, respectively.* ***76***

Figure 3.20 *%COD removal (hollow circles) of (i) 100 μM and (ii) 130 μM of RR-120 aqueous solution (at pH 7) as a function of the applied electron beam irradiation dose. %TOC removal (hollow stars) of (a) (i) 100 μM and (b) 130 μM of RR-120 aqueous solution (at pH 7) as a function of the applied electron beam irradiation dose.* ***77***

Figure 3.21 *% decolouration of (i) RR-120-0, (ii) RR-120-0.5 and (iii) RR-120-1 during the microbial treatment.* ***81***

Figure 3.22 *% TOC removal of RR-120-0.5, RR-120-1, RR-120-0-B, RR-120-0.5-B and RR-120-1-B.* ***82***

Figure 3.23 *FTIR spectra of (a) RR-120-0, (b) RR-120-0.5, (c) RR-120-1 and (d) RR-120-0-B, (e) RR-120-0.5-B, (f) RR-120-1-B.* ***85***

Figure 3.24 *Chromatograms of (a) RR-120-0, (b) RR-120-0.5, (c) RR-120-1 and (d) RR-120-0-B, (e) RR-120-0.5-B, (f) RR-120-1-B.* ***87***

Figure 3.25 *Negative ion ESI-MS spectra of (a) RR-120-0, (b) RR-120-0.5 and (c) RR-120-1.* ***89***

Figure 3.26 *In-source fragments of RR-120-0 in negative ion ESI-MS.* ***90***

Figure 3.27 *Radiolytic fragments of RR-120 found ESI-MS.* ***90***

Figure 3.28 *UV–visible spectra of (a) RR-120-0, (b) RR-120-0.5 and (c) RR-120-1.* ***91***

Figure 3.29 *Biodegradation pathways of RR-120-0 dye solution adapted by Pseudomonas sp. SUK1.* ***97***

Figure 3.30 *Biodegradation pathways of RR-120-0.5 dye solution adapted by Pseudomonas sp. SUK1.* ***98***

Figure 3.31 *Mineralization of STDWW by (a) photocatalysis (b) ozonolysis.* ***101***

Figure 3.32 *Mineralization of STDWW on gamma radiolysis (a) without and (b) with $K_2S_2O_8$.* ***103***

Figure 3.33 *Variation in mineralization extent with OCC of (a) radiolysis (b) photocatalysis (c) ozonolysis (d) radiolysis in presence of $K_2S_2O_8$. Inset: mineralization extent at lower OCC (a) radiolysis (b) photocatalysis (c) ozonolysis (d) radiolysis in presence of $K_2S_2O_8$.* ***105***

Figure 3.34 *Transient absorption spectra for the reaction of SDBS with (a) $^{\bullet}OH$, (b) $SO_4^{\bullet-}$ and (c) $O^{\bullet-}$ at dose of 14 Gy per pulse* ***107***

Figure 3.35 *Reactions of SDBS with $^{\bullet}OH$ and $SO_4^{\bullet-}$.* ***108***

Figure 3.36 *Variation of pH as a function of dose during gamma radiolysis of STDWW in the (a) absence and (b) presence of $K_2S_2O_8$ and (c) MSTDWW in presence of $K_2S_2O_8$.* ***111***

Figure 3.37 *Mineralization of MSTDWW in the presence of 40 mM $K_2S_2O_8$ during (a) gamma radiolysis and (b) EB radiolysis.* ***112***

Figure 3.38 *Mineralization of MSTDWW over different durations in: (a) photocatalysis, (b) photocatalysis in the presence of 40 mM $K_2S_2O_8$, (c) photolysis in presence of 40 mM $K_2S_2O_8$, (d) ozonolysis, and (e) ozonolysis in the presence of 40 mM $K_2S_2O_8$.* ***114***

Figure 3.39	*Mineralization of MSTDWW with OCC for (a) photocatalysis, (b) photocatalysis in the presence of 40 mM $K_2S_2O_8$, (c) photolysis in presence of 40 mM $K_2S_2O_8$, (d) ozonolysis, (e) ozonolysis in the presence of 40 mM $K_2S_2O_8$, (f) gamma radiolysis in the presence of 40 mM $K_2S_2O_8$ and (g) EB radiolysis in the presence of 40 mM $K_2S_2O_8$.*	***117***
Figure 4.1	*Molecular structures of (a) 4-Nitrophenol and (b) 4-Nitrophenate anion.*	***123***
Figure 4.2	*(a) UV-visible absorbance spectra of 0.1 mM 4-NP at pH (i) 4.0, (ii) 5.0, (iii) 6.0, (iv) 6.5, (v) 7.0, (vi) 7.2, (vii) 7.4, (viii) 7.7, (ix) 8.0 and (x) 10.0. (b) Absorbance maxima at (i) 317 nm and (ii) 400 nm as a function of pH.*	***124***
Figure 4.3	*Spectra of the transients produced by the reaction between $^{\bullet}OH$ and 4-NP at pH (a) 5.2 and (b) 9.2.*	***125***
Figure 4.4	*The reactions between 4-NP and $^{\bullet}OH$.*	***125***
Figure 4.5	*Spectra of the transients produced by the reaction between $N_3^{\bullet}$ and 4-NP at pH (a) 5.2 and (b) 9.2.*	***126***
Figure 4.6	*Spectra of the transients produced by the reaction between e^-_{aq} and 4-NP at pH (a) 5.2 and (b) 9.2.*	***127***
Figure 4.7	*The reaction between e^-_{aq} and 4-NP at pH (a) 5.2 and (b) 9.2.*	***128***

Figure 4.8 *% decolouration at 317 nm of 4-NP as a function of dose in 0.1 mM 4-NP solution purged with (i) N_2, (ii) air, (iii) O_2, (iv) N_2O and (v) (1:1) N_2O:O_2.* ***130***

Figure 4.9 *(a, b) % COD removal and (c, d) % TOC removal in the absence (a, c) and in the presence (b, d) of $K_2S_2O_8$ during gamma radiolysis of IBP as a function of absorbed dose.* ***131***

Figure 4.10 *(a) ΔOD/G plot and (b) corrected absorption spectra of the transient absorption spectra for reaction of IBP with (i) $^{\bullet}OH$, (ii) $SO_4^{\bullet-}$ (iii) $O^{\bullet-}$ at 14 Gy/pulse.* ***134***

Figure 4.11 *Variation in the transient peak intensities at (i) 270, (ii) 315 and (iii) 330 nm, as a function of pH, by the reaction between IBP and $^{\bullet}OH$.* ***136***

Figure 4.12 *Reaction scheme of IBP with (a) $^{\bullet}OH$ and (b) $SO_4^{\bullet-}$.* ***136***

Figure 4.13 *Decay profiles of the transients absorbing at (a) 315 and (b) 270 nm for the reaction of IBP with (i) $^{\bullet}OH$ and (ii) $SO_4^{\bullet-}$.* ***138***

Figure 4.14 *Decay profiles of the transients absorbing at 270 nm for the reaction of IBP with $SO_4^{\bullet-}$ in (a) absence (i) and presence (ii) of O_2 and (b) at different concentrations of $K_2S_2O_8$.* ***138***

Figure 4.15 *The relative absorbance, with reference to the parent absorption (ΔA), of the products formed by steady state gamma radiolysis of IBP as a function of dose in (a) absence and (b) presence of $K_2S_2O_8$; (c) relative absorbance of the intermediate products with reference to the parent absorption per unit yield of the oxidant ((ΔA)/G of oxidant) at selected doses in the absence (dotted lines) and the presence (solid lines) of $K_2S_2O_8$.* ***140***

List of Tables

Table No.	Caption	Page No.
Table 1.1	*Advantages and limitations of AOPs.*	**12**
Table 1.2	*The reaction of formation of primary species inside spurs.*	**23**
Table 1.3	*Relevant reactions for predominantly producing rediolytic species of interest*	**27**
Table 2.1	*Specifications of 7 MeV LINAC*	**31**
Table 2.2	*Specifications of 2 MeV LINAC*	**35**
Table 2.3	*Specifications of 10 MeV LINAC*	**36**
Table 3.1	*% BOD_5 and BOD_5/COD ratio of 147 and 191 ppm aqueous RR-120 solutions at pH 7 for different radiation doses.*	**80**
Table 3.2	*Toxicity studies of 600 ppm RR-120-0 and metabolites produced from 600 ppm RR-120-0-B, RR-120-0.5-B and RR-120-1-B using Pseudomonas sp. SUK1.*	**84**
Table 3.3	*Activities of laccase, tyrosinase, azo reductase and NADH-DCIP reductase in control Pseudomonas sp. SUK1 cells and cells obtained from RR-120-0-B and RR-120-1-B.*	**92**
Table 3.4	*GC-MS analysis of the metabolites formed from RR-120-0-B, RR-120-0.5-B and RR-120-1-B solutions.*	**93**
Table 3.5	*Composition of STDWW*	**100**

Table 3.6 *Comparison of the cost of energy and ancillary chemicals for different AOPs.* ***118***

Table 4.1 *A comparative study of IBP mineralization during gamma radiolysis in the absence and the presence of* $K_2S_2O_8$. ***132***

CHAPTER 1

Introduction

1.1. Environmental impact of organic pollutants

Water, an elixir of life, is one of the first victims of the environmental pollution. The availability of the fresh water is only 2.7%, even though the surface of the earth is geographically covered with more than 70% water. The paucity of fresh water demands the technologies that could treat and recycle water efficiently and economically. The effluents from textile, pharmaceutical and other industries lead to extensive water pollution. In addition to dyes, pesticides and drugs, the industrial effluents also carry several other organic contaminants. The present work includes representative organic pollutants namely (1) dye (Reactive Red-120), (2) pharmaceutical drug (Ibuprofen) and (3) nitro compound (4-nitrophenol). The nitroaromatic compounds are important building blocks for the large scale synthesis of pesticides, pharmaceuticals, plastics, azo dyes and explosives and thus pollute directly or indirectly the river and ground water.

1.1.1. Textile dyes and their environmental concern

Synthetic dyes are extensively used in textile dyeing, paper printing, color photography, pharmaceutical, food and cosmetic industries *[1]*. The textile industries consume dyes for textile fibers like cotton and polyester. Increase in the number of the synthetic dyes used by textile industries has created an aquatic pollution alarm. The textile dyes as well as the dye intermediates with high aromaticity and low biodegradability have emerged as major aquatic pollutants *[2, 3]*.

1.1.1.1. Classification of textile dyes

A dye is a water soluble colored substance that has an affinity to the substrate to which it is being applied. Dyes contain chromophores, which places the electronic

energy levels of the molecules through a conjugated system of electrons in the visible wavelength of light. The common chromophores are -C=C-, -C=N-, -C=O,-N=N-, -NO_2, quinoid rings etc. Auxochromes are electron-withdrawing and/or electron-donating substituents present in the dye molecule. The auxochromes change the electronic energy levels of the dye, intensifies the colour and sometimes it fixes the dye molecule on the fiber. Common auxochromes include -NH_2, -COOH, -SO_3H and -OH groups. Each dye is designated by a C.I. (Color Index) generic name constituted from its method of application, color of the dye and a sequential number. The colourant also has a corresponding five-digit C.I. constitution number that uniquely identifies its chemical structure. The C.I. discerns the dyes for different classes of applications *[4]*.

Acid dye: Acid dyes are anionic compounds which are predominantly applied in dyeing fibres like wool, polyamide, silk and modified acryl. The acid dyes bind to the cationic NH_4^+ ions of the fiber. Most acid dyes are azo, anthraquinone or triarylmethane, azine, xanthene, nitro and nitroso compounds. Acid dyes are the largest class of dyes in the C.I.

Basic dye: Basic dyes are cationic compounds that are used for dyeing acid-group containing fibres, like modified polyacryl. Most of the basic dyes are diarylmethane, triarylmethane, anthraquinone or azo compounds.

Metal complex dyes: These dyes form strong complexes with metal atoms (usually chromium, copper, cobalt or nickel) in 1:1 and 1:2 dye:metal ratio. Metal complex dyes are usually azo compounds.

Direct dyes: Direct dyes are relatively large molecules with high van der Waals affinity for cellulose fibers. Direct dyes are mostly azo dyes with multiple azo bonds or phthalocyanine, stilbene or oxazine compounds.

Disperse dyes: Disperse dyes are scarcely soluble in water. The penetration of these dyes into synthetic fibers (cellulose acetate, polyester, polyamide, acryl, etc.) requires swelling of the fiber, either due to high temperatures (>120 °C) or with the help of chemical softeners. Disperse dyes are usually small azo or nitro compounds (yellow to red), anthraquinones (blue and green) or metal complex azo compounds.

Pigment dyes: Pigment dyes (i.e. organic pigments) represent a small fraction of widely applied insoluble and non-ionic group of colorants. Pigment dyeing is achieved from a dispersed aqueous solution prepared with the aid of dispersing agents. Most pigment dyes are azo compounds (yellow, orange, and red), metal complex phthalocyanines (blue and green) and anthraquinone or quinacridone pigment.

Vat dyes: Vat dyes are water-insoluble dyes that are particularly and widely used for dyeing cellulose fibers. The dyeing method is based on the solubility of vat dyes in their reduced (leuco) form. Reduced with sodium dithionite, the soluble leuco vat dyes impregnate the fabric. Next, oxidation is applied to bring back the dye in its insoluble form. Almost all vat dyes are anthraquinones or indigoids.

Reactive dyes: Reactive dyes are capable of forming a covalent bond between a carbon atom of dye molecule and -OH-, -NH, or -SH groups in fibers (cotton, wool, silk, nylon) under alkaline condition during dyeing process. The reactive group is often a heterocyclic aromatic ring substituted with a chloride atom, e.g. dichlorotriazine. The mechanism of cotton dyeing by reactive dye is shown in the Figure 1.1. Another common reactive group is vinyl sulphone. Most of the reactive dyes are azo or metal complex azo compounds, though anthraquinone and phthalocyanine reactive dyes are also available. In the C.I., the reactive dyes form the second largest dye class. The

estimated world production of synthetic dye is ~10^6 tons of which azo dyes contributed 70% *[5]*.

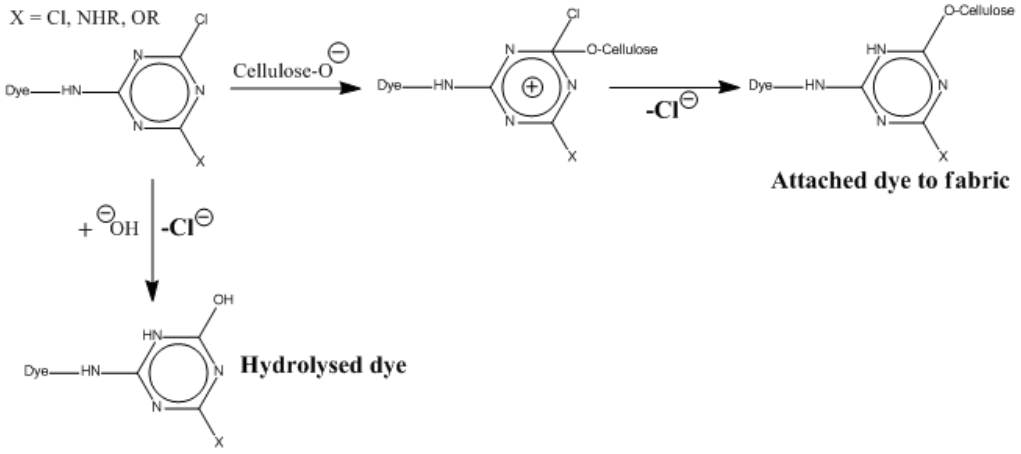

Figure 1.1 *The mechanism of cotton dyeing by reactive dye.*

1.1.1.2. Discharge statistics of reactive dyes and other auxiliary chemicals in textile waste water

The hydrolysis (i.e. inactivation) of the reactive groups is an undesired side reaction encountered during the dyeing process with reactive dyes (Figure 1.1). It lowers the degree of fixation of the dye molecule to the fabrics and thus cannot be further reused. It is estimated that 10% to 50% of the dye molecules do not react with the fabric due to the hydrolysis of dye molecule. Therefore, the recovery of dye from the effluent is not an option for reactive dyes. Therefore, the treatment process should lead to the final destruction or disposal of the hydrolyzed dyes. The concentration of water soluble brightly colored reactive azo dyes varies from 10-10000 ppm, depending on the strength of the dye and process of operation *[6, 7]*. The synthetic reactive dye is photolytically and biologically stable. The sulfonated azo dyes inhibit the rate of biodegradation *[8, 9]*. Further the higher azo bond energy compared to the solar photon energy makes the dye photolytically stable. The low BOD_5/COD ratio of most of the

dye solution indicates that removal of these dyes would be difficult by conventional methods such as biological processes *[10, 11]*.

Textile effluents are hazardous to the ecosystem, because of the implementation of intense colour to water from the bioresistant synthetic dye molecules even at very low concentrations. Moreover, the auxiliary chemicals (such as surfactants, sequestering agents, pH-adjusting acids, and inorganic salts) of the dye bath contribute to about 83% of the organic load of the textile effluent. The heavy organic load of the textile effluent causes a negative impact to aquatic lives, owing to the decrease in the dissolved oxygen concentration in the water stream. The chemical oxygen demand (COD), which is a measure of the organic load, varies in the range of 2900-3000 ppm in textile effluents. Since this is well above the permissible discharge limit (COD $\leq$ 250 ppm) set by the Central Pollution Control Board under the Ministry of Environment and Forest, Government of India, the development of an effective and efficient treatment process for textile effluents is highly necessary.

1.1.2. Pharmaceuticals and their environmental concern

The substance or combination of substances administered to human or animals either with a view to restoring or modifying physiological functions is termed as drug or pharmaceutical. The excretion from human and animal bodies is generally accepted as the principal source of human pharmaceuticals detected in the aquatic environment. The domestic waste water contains pain killers, beta-blockers, cholesterol lowering agent, antibiotics, anastatics, X-ray contrast media and anti-epileptics in concentrations up to tens of $\mu g\ L^{-1}$ which is much lower compared to detected concentrations in the effluents from pharmaceutical industry and hospitals. Discharges from manufacturing facilities are not believed to contribute significantly to the overall water pollution.

Discharge of active pharmaceutical ingredient via waste stream is generally avoided since it constitutes a valuable product. A common practice in pharmaceutical industry is to recover and reuse of the active ingredients. Otherwise, incineration treatment is applied. Therefore, undistributed or outdated products are unlikely to be a source of pharmaceuticals detected in the environment *[12]*. However, patients' disposals of unused, outdated or sold over-the-counter pharmaceuticals generally go into the domestic wastewater or solid waste.

Many variety of drugs are used according to their function or biological activities e.g. beta blockers, lipid lowering drugs, antibiotic, antifungal, antidiabetic, antiseptics, antihypertensives antidepressant, antipsychotic, antiphlogistics, analgesics and nonsteroidal anti-inflammatory drugs, usually abbreviated to NSAIDs. NSAIDs are a class of drugs that provides analgesic (pain-killing), antipyretic (fever-reducing) and anti-inflammatory effects and are consumed in significant quantity. These are among the most prevailing groups of pharmaceutical contaminants *[13]*. The term nonsteroidal distinguishes these drugs from steroids, which, among a broad range of other effects, have a similar anti-inflammatory action. As analgesics, NSAIDs are unusual in that they are non-narcotic and thus are used as a non-addictive alternative to nacrotics.

Certain NSAIDs, including ibuprofen (IBP), naproxen and aspirin, have become accepted as relatively safe and are available over-the-counter without prescription *[14]*. NSAIDs inhibit the activity of both cyclooxygenase-1 (COX-1) and cyclooxygenase-2 (COX-2), and thereby, the synthesis of prostaglandins and thromboxanes. It is thought that inhibiting COX leads to the anti-inflammatory, analgesic and antipyretic effects. However, some implications of long-term effects from IBP on the ecosystem have been evidenced *[15-18]*. Firstly, it is a persistent pollutant as it is not completely destroyed in a municipal water treatment plant. Long solid retention time promotes the adaptation

of different kinds of slower growing microorganisms that could have a greater capacity for removing IBP and its removal was only achieved after the growth of specific bacteria *[19, 20]*. Secondly, it adversely affects several aquatic plants and fungal species. Most importantly, it has been reported that IBP present at concentrations of 400-800 μM in drinking water along with other environmental pharmaceuticals might impede cell proliferation in human embryonic cells *[17]*. Recently, a study by World Health Organization (WHO) reported IBP as the leading contaminant among other pharmaceuticals *viz*. Erythromycin, Bleomycin etc. present in aquatic environment in United Kingdom *[14]*.

1.1.3. Nitrocompounds and their environmental concern

The nitro-substituted aromatic compounds are important building blocks for the large scale synthesis of pesticides, pharmaceuticals, plastics, azo dyes and explosives and also serve as precursors for the production of amino aromatic derivatives *[21-23]*. Therefore, nitro-compounds, especially nitrophenols, are widely used industrial organic compounds. Among the nitrophenols, o-nitrophenol, 2,4-dinitrophenol and 4-nitrophenol (4-NP) are listed as priority pollutants by the U.S Environmental Protection Agency *[24, 25]*. 4-NP is not only used extensively in manufacturing processes but is also a major metabolite in the hydrolysis of parathion and methyl parathion, which are two popular organophosphate pesticides used for agricultural crop protection *[26]*. The water soluble 4-NP pollutes rivers, groundwater, pesticide treated soils *[25, 27-28]*.

The majority of nitroaromatic compounds are highly toxic to micro-organisms. Further, the nitro groups or chloro-substituents reduce the electron density of the aromatic ring and thus impede electrophilic attack of oxygenases and oxidative degradation of nitroaromatic compounds *[29]*. The nitroaromatic compounds are

transformed by several microorganisms to azo, azoxy- and polymeric compounds, which are more toxic than the parent compounds *[22]*. 4-NP is toxic for aquatic life. It has high oxygen demand, 2.4 mg O_2 per mg of 4-nitrophenol. It can also combine with existing chlorine in drinking water producing chlorophenols, which are even more toxic and difficult to eliminate.

The present work is limited to the studies on three aquatic pollutant molecules viz. (1) textile dye (Reactive Dye-120), (2) pharmaceutical drug (Ibuprofen) and (3) nitro-compound (4-nitrophenol).

1.2. Advanced Oxidation Processes (AOPs)

The conventional effluent treatment plants employ physicochemical methods such as chemical precipitation, coagulation, reverse osmosis, activated carbon etc. *[30, 31]*. However, these physicochemical treatment processes suffer from the large amount of secondary sludge generation *[32]*. From this point of view, microbial treatment is more eco-friendly, cost-competitive alternative, with few limitations. Firstly, many synthetic organic pollutants are toxic to the micro-organisms and therefore, the efficiency of biodegradation depends on the molecular structure of these pollutants *[33, 34]*. Secondly, the process efficiency of the microbial treatment plant is not very effective owing to the time span of the biodegradation process. Finally, the aerobic treatment process is associated with production and disposal of large amounts of biological sludge, and wastewater treated by anaerobic treatment method does not bring down the pollution parameters to the satisfactory level.

The advancement of the water treatment processes is focused on the development of efficient processes for the oxidation of bio-recalcitrant organic compounds. Advanced oxidation process (AOP) involves in-situ generation of hydroxyl radicals

($^{\bullet}$OH) which can effectively oxidize the organic pollutants. After fluorine [standard reduction potential (E_0) = 2.889 V vs. Normal Hydrogen Electrode (NHE)], $^{\bullet}$OH is the second strongest known oxidant having E_0 of 2.72 V vs. NHE. The fenton, photocatalysis, sonolysis and ozonolysis are well studied AOPs, which showed strong ability to oxidise organic compounds leading to their decomposition and this limits the productions of sludge and toxic intermediates. Table 1.1 shows the advantages and limitations of some of the selected AOPs. Radiolysis using high energy ionizing radiation is upcoming as one of the promising AOPs for the degradation of varieties organic pollutants in aqueous solution. Among all the AOPs, radiation technology, photocatalysis, ozonolysis are used in this work.

1.2.1. Radiation Technology

The radiation chemistry implies the chemical effect of interaction of ionizing radiation with matter. The ionizing radiation may be either electromagnetic radiations e.g. X-rays, gamma(γ)-rays or particulate radiations, e.g. electrons, beta-particles, alpha-particles, protons, neutrons and fission fragments having energies 10 eV to several million eV (MeV). In this work, only high energy γ-ray and e-beam radiations have been used having energy several order magnitude greater than the usual bond energies capable of causing extensive ionization of the materials.

1.2.2. Photocatalysis

On illuminating the photocatalyst such as TiO_2 with UV light, the electrons from the valence bands (VB) are promoted to the conduction bands (CB) generating a hole in the valence band. The promoted electron in the conduction band reacts with the dissolved oxygen producing $O_2^{\bullet-}$ and $HO_2^{\bullet}$, whereas, the hole generated in the valence band can react with either with organic molecule or OH^- (Figure 1.2).The reaction of

the hole with OH^- produces $^{\bullet}OH$ radical, which can also oxidize the organic molecule *[45]*. The complete photocatalytic cycle is shown in reactions (1.1-1.5):

$$TiO_2 + h\nu\ (UV) \rightarrow TiO_2\ (e^-_{CB} + h^+_{VB}) \quad (1.1)$$

$$TiO_2\ (h^+_{VB}) + H_2O \rightarrow TiO_2 + H^+ + {}^{\bullet}OH \quad (1.2)$$

$$TiO_2\ (h^+_{VB}) + OH^- \rightarrow TiO_2 + {}^{\bullet}OH \quad (1.3)$$

$$TiO_2\ (e^-_{CB}) + O_2 \rightarrow TiO_2 + O_2^{\bullet-} \quad (1.4)$$

$$O_2^{\bullet-} + H^+ \rightarrow HO_2^{\bullet} \quad (1.5)$$

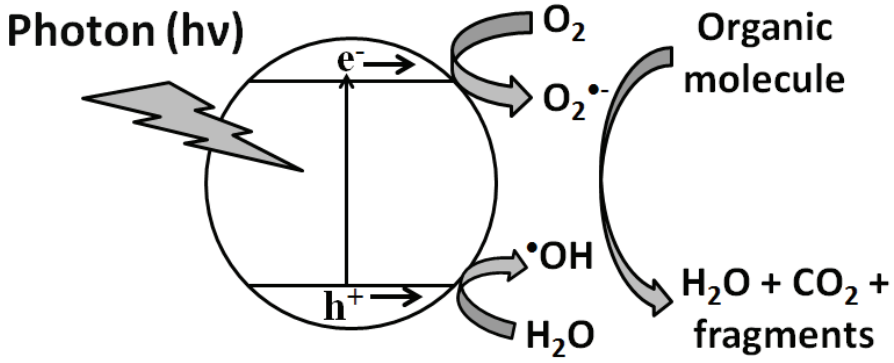

Figure 1.2 *The mechanism of photocatalytic degradation of organic molecule.*

The heterogeneous photocatalyst is used to decompose the aquatic organic pollutants. $Ti0_2$ is photoactive in the UV region (<400 nm) of the electromagnetic spectrum. In aqueous $Ti0_2$ suspension systems, $^{\bullet}OH$ is produced from the trapping of holes (after UV irradiation) at the surface hydroxyl groups. The photogenerated electrons are scavenged by the dissolved oxygen.

1.2.3. Ozonolysis

Ozone, which itself is a strong oxidant (E_0 = 2.07 V vs. NHE), can produce more powerful oxidant i.e. $^{\bullet}OH$ (E_0 = 2.72 V vs. NHE) under alkaline condition (pH 10) through reactions (1.6-1.8) *[46]*.

$$O_3 + H_2O \rightarrow 2\ {}^{\bullet}OH + O_2 \quad (1.6)$$

$$O_3 + OH^- \rightarrow O_2^{\bullet-} + HO_2^{\bullet} \quad (1.7)$$

$$O_3 + HO_2^{\bullet} \rightarrow 2O_2 + {}^{\bullet}OH \quad (1.8)$$

Table 1.1 *Advantages and limitations of AOPs*

Treatment Method	Advantages	Limitations	references
Fenton oxidation $Fe(II)/H_2O_2$	Effective degradation of organic compounds.	1. Addition of external reagent 2. pH in the acidic range to get maximum decolouration while textile process wastewaters usually have high pH 3. Sludge generation	*[35, 36]*
Photchemical oxidation H_2O_2/UV	Effective degradation of organic compounds; Iron catalyst-associated sludge generation is eliminated; No need to keep acidic pH.	1. UV catalyzed degradation requires frequent lamp maintainance, replacement and high power demand. 2. Efficiency decreases due to absorption of UV by coloured effluent (as H_2O_2 has poor UV absorption) and lesser penetration in waste water containing turbidity. 3. Excess H_2O_2 decreases the degradation reaction due to scavenging action.	*[36, 37]*
Photocatalytic oxidation TiO_2/UV	Effective degradation of organic compounds.	1. Relatively high band gap energy of TiO_2 (above 3.0 eV for rutile and 3.2 eV for anatase, corresponding to UV-A radiation) limits only 3-5% absorption of solar light 2. Using TiO_2 suspensions needs a post-treatment separation stage 3. Size and shape of TiO_2 nanoparticles are crucial parameters 4. Requires frequent lamp maintainance, replacement and high power demand. 5. Efficiency decreases due to lower penetration efficiency of UV light	*[38, 39]*
Ozone treatment	Good degradation of organics; Applied in gaseous state, no alteration of volume or no post treatment separation stage.	1. O_3 has lower oxidation potential (~2.0 V vs. NHE) 2. Operating cost and capital cost of ozone generation is much higher than other chemical oxidation techniques	*[40, 41]*
Electrochemical oxidation	Potential method of pollution control, offering high removal efficiency; Break-down compounds are non hazardous.	1. High electricity consumption 2. Limited life time of the electrode	*[42, 43]*
Sonolysis	Good degradation of organics.	1. Relatively inefficient with respect to the input energy 2. Energetic cost penalty usually assigned to sonochemical technology	*[44]*

1.3. Interaction of High Energy Radiation with Matter

The interaction of the ionizing radiation with matter depends on the nature (i.e., energy, particulate mass and charge) of radiation, phase state of the matters and the atomic number (electron density) of the interacting medium. The following subsections discuss the mechanisms of interaction of (i) electromagnetic radiation (γ-ray) and (ii) charged particle (electron) with absorbing material *[47-49]*.

1.3.1. Gamma Radiation

Electromagnetic radiation of nuclear origin having energy in the range of 40 keV to 4 MeV is termed as gamma rays (γ-rays). Passing through a material it gets attenuated and followed the Eq. 1.9.

$$I = I_o e^{-\mu x} \qquad (1.9)$$

Where, I_0 is the incident radiation intensity; x is the thickness of the material through which radiation has traversed and μ is called linear attenuation coefficient. μ is the sum of partial coefficients representing five processes of attenuation viz. (i) photoelectric effect, (ii) Compton effect, (iii) pair production, (iv) coherent scattering and (v) photonuclear reactions. Coherent scattering is of importance for low energy photons (<0.1 MeV) and in high Z materials, whereas photonuclear reactions are possible with photons of energies in the range of 2 to 8 MeV for low Z materials and in the region of 7-20 MeV for high Z materials. Therefore, first three processes are most important for gamma radiation emitted by ^{60}Co source (two photons of energies 1.33 MeV and 1.17 MeV), though the relative importance of each process depends on the atomic number of the absorbing material.

1.3.1.1. Photoelectric Effect

The photoelectric effect is the main mode of interaction for low energy photon. During interaction, the photon transfers its entire energy to a bound electron in an atom and that electron is ejected from the atom. If E_ν is the energy of the incident photon and E_b is the binding energy of the electron, the kinetic energy of the ejected electron E_{KE} is expressed as:

$$E_{KE} = E_\nu - E_b \qquad (1.10)$$

If the photon energy is sufficiently high, the probability of ejection of the most tightly bound electron of an atom (i.e. electron from the K-shell) is increased. The vacancy created by loss of an inner orbital electron is filled by an electron from a lower energy outer orbital with emission of X-rays. These X-rays may also eject another electron from the same atom (Auger effect). The cross section for the photoelectic interaction is denoted by τ.

1.3.1.2. Compton Scattering

Compton scattering occurs when a photon interacts with a free or loosely bound electron, so that the electron is accelerated and the photon is deflected with reduced energy. The energy of the recoil electron (E_e) is given by Eq. 1.11:

$$E_e = E_\nu - E_\gamma \qquad (1.11)$$

where E_ν and E_γ are the energies of the incident and deflected photons. These electrons cause ionization and excitation in the medium while deflected photon must undergo further Compton and photoelectric interaction. Compton scattering predominates for photon energies between 1-5 MeV for high Z materials and over a much wider range of energies in low Z materials. In water, Compton interaction is the predominant process

for photon energies from 30 keV to 10 MeV. The cross section for compton scattering is denoted by σ.

1.3.1.3. Pair Production

This process is the reverse of electron-positron annihilation phenomenon. It involves complete absorption of a photon with energy greater than 1.02 MeV (the energy of equivalent rest mass of electron positron pair) in the vicinity of an atomic nucleus with production of two particles, e^{-1} and e^{+}. Energy in excess of 1.02 MeV appears as kinetic energy of the pair (E_e and E_p)

$$E_v = E_e + E_p + 2\, m_e c^2 \qquad (1.12)$$

Momentum is shared by the recoiling nucleus. While the resulting positron ultimately combines with an electron releasing two γ-rays of energy 0.51 MeV in opposite direction and the electron interacts with the material as described earlier. From the energetic of this process, it is obvious that pair production can occur at photon energies greater than 1.02 MeV (=2 $m_e c^2$). The cross section for this reaction is denoted by χ.

Thus, depending on the incident photon energy, the photon gets attenuated. The total linear attenuation coefficient is given by Eq. 1.13.

$$\mu = \tau + \sigma + \chi \qquad (1.13)$$

where, τ, σ and χ are represented in cm^{-1}.

1.3.2. Electrons

Electron beam is produced by the electron beam accelerator. The most important processes by which charged particles including electron interact with matter are: (i) elastic scattering, (ii) inelastic collisions and (iii) emission of electromagnetic

radiation. The relative probability of each process depends mainly upon the energy of the electron, and to a smaller extent on the nature of the absorbing material.

1.3.2.1. Elastic Collision

The electron gets deflected by the electrostatic field of an atomic nucleus. This essentially leads to a change in the direction of motion of electron. This is more probable for electrons with low energy and absorbing material having high atomic number.

1.3.2.2. Inelastic Collision

Inelastic collision is the most probable interaction of electron with atoms of absorbing material. The average amount of kinetic energy lost (leading to excitation and ionization) per unit length by a fast electron through Coulomb interaction with atomic electrons in a medium is defined as the specific energy loss or stopping power (S in erg g^{-1}) of the medium and S is defined by the Bethe's equation *[50]* (Eq. 1.14)

$$S = -\frac{dE}{dx} = \frac{2\pi e^4 N_0 Z}{m_0 v_1^2}\left[\ln\frac{m_0 v_1^2 E}{2I^2(1-\beta^2)} - (2\sqrt{1-\beta^2} - 1 + \beta^2)\ln 2 + 1 - \beta^2 + \frac{1}{8}(1-\sqrt{1-\beta^2})^2\right] \quad (1.14)$$

where, e represents the charge of the electron in electrostatic unit and m_0 is the rest mass of electron in gm, c and v_1 are the velocities of light in vacuum and the bombarding electron in cm sec^{-1}, N_0 is the number of atoms cm^{-3} in the medium, β is the ratio of *v* to the velocity of light c in vacuum (and is numerically represented as $\beta = \sqrt{1 - \{m_0c^2 / (E - m_0c^2)\}^2}$, Z is the atomic number and I is the mean excitation potential of the atoms in the stopping material per cubic cm. For electron of energy E, the ratio of energy loss by radiation to the loss by collision is given by Eq. 1.15 where the various terms are mentioned earlier.

$$\frac{(dE/dl)_{rad}}{(dE/dl)_{col}} \approx \frac{EZ}{1600 m_e c^2} \qquad (1.15)$$

1.3.2.3. Emission of Bremssstrahlung

High energy electrons passing close to the nucleus of an atom are decelerated due to their interaction with the electric field of the nucleus and radiate electromagnetic energy as bremsstrahlung. The rate of bremsstrahlung i.e. the emission of X-radiations (of energy E) per unit length (L), is proportional to the square of the charge on the particle (z) and on the nucleus (Z) and the mass (m) of the particle, as represented in Eq. (1.16)

$$R = -\frac{dE}{dL} \approx \frac{z^2 Z^2}{m^2} \qquad (1.16)$$

Bremsstrahlung formation does not produce any significant changes in the stopping material unless it interacts subsequently with it. For electrons, bremsstrahlung emission is negligible below 100 KeV, but it increases rapidly with increasing electron energy, and it is the dominant mode of energy loss of electron having energy between 10-100 MeV.

1.3.3. Comparative radiolysis on the phase state of matters

The primary interactions of radiation are essentially independent of the phase state of the matters. However, the nature and yield of the products are often dependent on the physical state of the matter because of the variations in the density of the medium and mobility of the primary species and radicals in the different phases. The solid phase generally has the highest density. Therefore, the diffusion of the primary radicals in the solid phase is very slow resulting into prompt recombination. The gamma radiolysis in solid leads to the defects in the crystalline lattice and breaks

chemical bonds of the organic solids. On the other hand, the gaseous phase has generally lowest density. Therefore, the primary species produced by the radiolysis distribute homogeneously though out the gas. The liquid phase generally has the intermediate density compared to the solid and gaseous phase. Therefore, the nature of the radiolysis product depends upon the viscosity and dielectric constant of the liquid.

1.3.4. Depth-dose profiles for gamma and electron beam irradiation

The penetration of radiation energy into the absorbing material is represented by depth-dose curve, in which the relative adsorbed dose at a particular point is plotted as a function of the distance (depth) of that point from the irradiated face of the sample. Typical depth dose curves for irradiation of water by (a) gamma radiation and (b) electron beam irradiation are shown in Figure 1.3, which shows a gradual build up of adsorbed dose upto a maximum and followed by a decline of adsorbed dose with increasing the depth. The surface dose of electron beam is much higher compared to that of gamma radiation. The rate at which the dose increases from the surface to the maximum is therefore less pronounced for electron beams than for photon beams. Unlike in photon beams, the per cent surface dose for electron beams increases with electron energy. At lower energies, electrons are scattered more easily and through larger angles. This causes the dose to build up more rapidly and over a shorter distance. Scattering and continuous energy loss by electrons is the two processes responsible for the sharp drop-off in the electron dose at depths beyond the maximum. Bremsstrahlung produced in the head of the accelerator, in the air between the accelerator window and the patient, and in the irradiated medium is responsible for the tail in the depth dose curve [51].

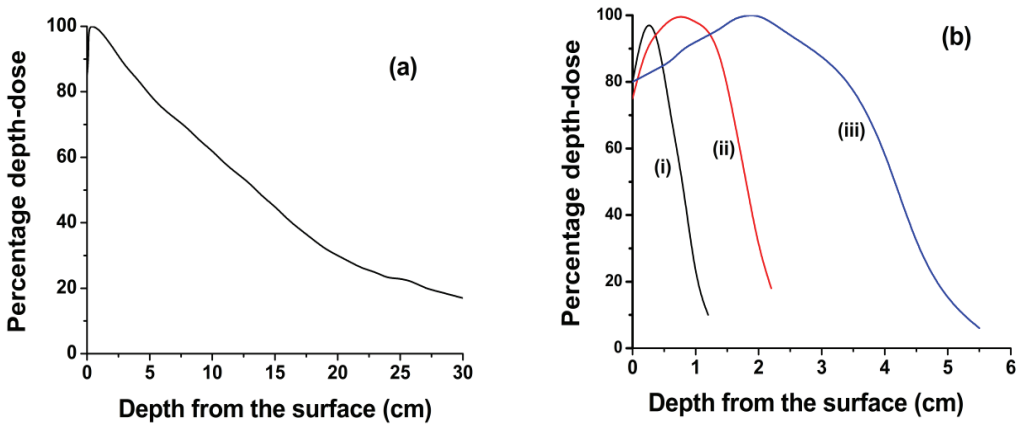

Figure 1.3 *Depth dose curves for irradiation of water by (a) ^{60}Co gamma radiation and (b) electron beam of (i) 1.8, (ii) 4.7 and (iii) 10.6 MeV energy.*

1.3.5. Radiation chemistry of water

The radiation chemistry is employed in this work to degrade the organic pollutants present in the water. Therefore, it is relevant to briefly discuss the radiation chemistry of water. The time scale of the events initiated by the absorption of radiation energy by water molecule can be summarized by Figure 1.4 *[52]*. The yield of the radical and molecular species is expressed in terms of G value, where G is the number of species formed (or destroyed) per 100 eV of the absorbed dose. The SI unit of G value is mol J^{-1}, which is equivalent to 9.65×10^{6} molecules $(100\ eV)^{-1}$. Hence, G values reported originally in terms of number of species per 100 eV can be converted to SI units by multiplying by 1.036×10^{-7}.

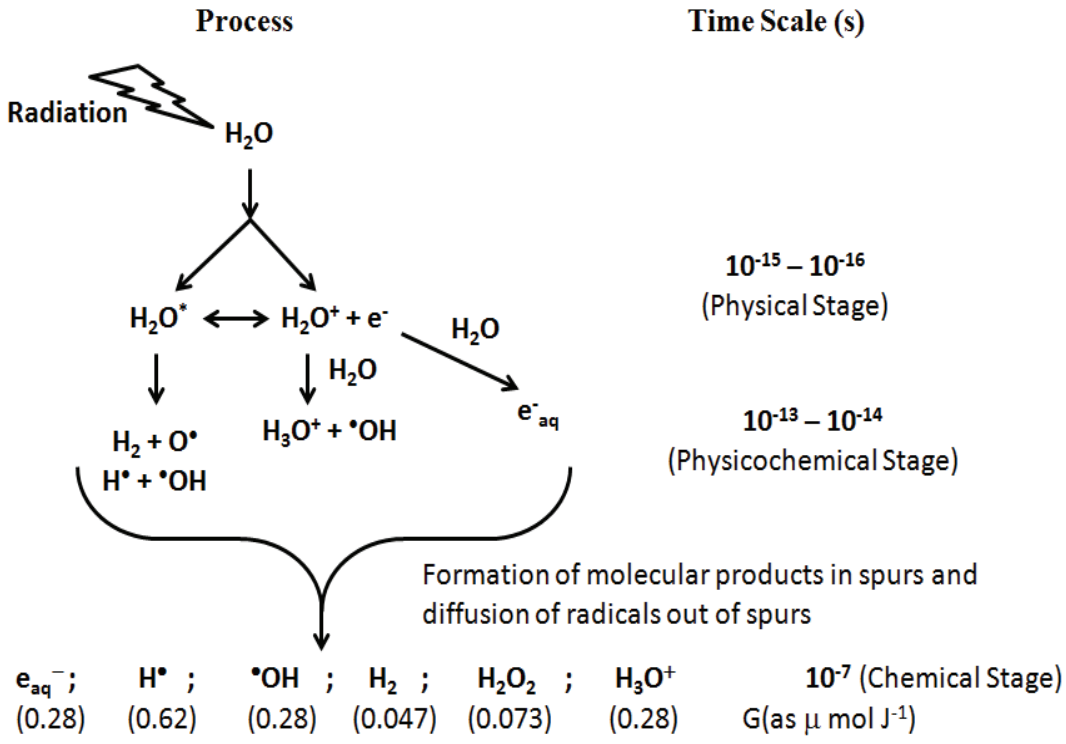

Figure 1.4 *Radiolysis products of water in the time scale of 10^{-16} - 10^{-7}s.*

The water molecule can be either ionized or excited upon interaction with high energy γ-ray photon from ^{60}Co or electron generated by an electron accelerator.

$$H_2O \rightarrow H_2O^+ + e^- \qquad (1.17)$$

$$H_2O \rightarrow H_2O^* \qquad (1.18)$$

After ionization of water, the positively charged ions are thought to be energetically unstable and undergo ion-molecule reaction in 10^{-14} seconds producing ${}^\bullet OH$ radical.

$$H_2O^+ + H_2O \rightarrow H_3O^+ + {}^\bullet OH \qquad (1.19)$$

Some of the H_3O^+ also recombine with e^- resulting into excited H_2O, which can auto ionize, dissociate or simply revert back to ground state.

$$H_2O^+ + e^- \rightarrow H_2O^* \quad (1.20)$$

$$H_2O^* \rightarrow H^\bullet + {}^\bullet OH \quad (1.21)$$

$$H_2O^* \rightarrow H_2O^+ + e^- \quad (1.22)$$

The e^- liberated in the ionization has sufficient energy to ionize further H_2O molecules. This leads to the formation of cluster of ions along the track of the ionizing particle (Figure 1.5).

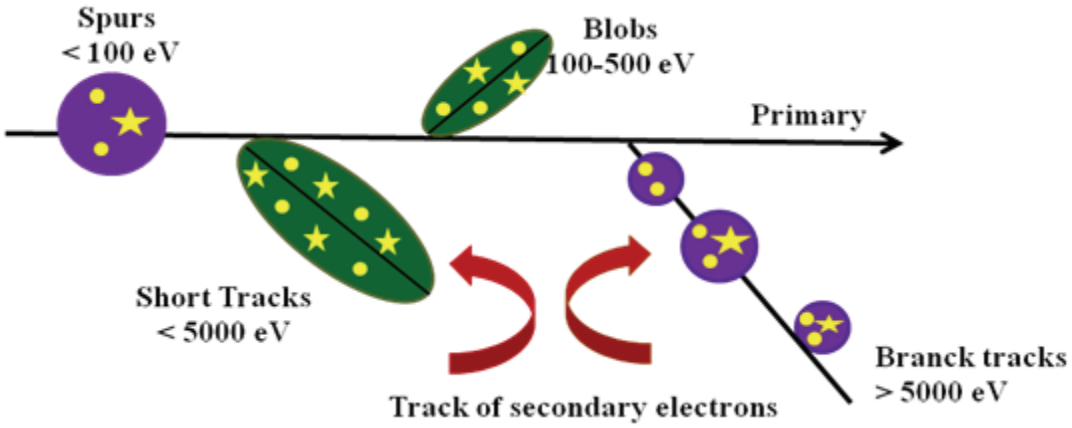

Figure 1.5 *Distribution of ions and excited species along the track of fast primary electron and secondary electron; (•) represents the ions and radicals, (★) represents the excited species.*

Eventually, the energy of liberated e^- falls below the ionization threshold of water and then it dissipates rest of its energy by exciting vibrational and rotational modes of the solvent molecules. Finally, it would be localized in a potential energy well long enough to become solvated as a result of molecular dipoles rotating under the influence of the negative charge, and thus get stabilized as hydrated electron (e^-_{aq}). The electrons are thermalised in about 10^{-13} s. Thus all the primary radicals and ionized species ($^\bullet OH$, $^\bullet H$, e^-_{aq}, H_3O^+) resulting from the initial ionization are concentrated in a small volume. This

small zone of reactive species is known as "*spur*" (Figure 1.5). Due to the small volume of the spur, $^{\bullet}OH$, $^{\bullet}H$ and e^{-}_{aq} exist very close to each other. Therefore, a part of theses radicals can react with one another to reform water or molecular products i.e. H_2 and H_2O_2, while the remaining radicals can escape into the bulk solution and become homogeneously distributed throughout the medium. This *spur expansion* is completed in about 10^{-7}s. Thus, in the nanosecond time scale, different processes ultimately produce charge species e_{aq}^{-} & H_3O^{+}; radicals $^{\bullet}OH$ & $^{\bullet}H$ and molecular products H_2 & H_2O_2 *[48, 49]*. These species are also known as the primary species. The reactions for the formation of the primary species inside spurs are listed in Table 1.2.

Table 1.2 *The reaction of formation of primary species inside spurs.*

Reactions	k / × 10^{10} M^{-1} s^{-1}
$e_{aq}^{-} + e_{aq}^{-} \rightarrow H_2 + 2OH^{-}$	0.6
$e_{aq}^{-} + {}^{\bullet}OH \rightarrow OH^{-}$	3.0
$e_{aq}^{-} + H_3O^{+} \rightarrow {}^{\bullet}H + H_2O$	2.3
$e_{aq}^{-} + {}^{\bullet}H \rightarrow H_2 + OH^{-}$	2.5
$^{\bullet}H + {}^{\bullet}H \rightarrow H_2$	1.3
$^{\bullet}OH + {}^{\bullet}OH \rightarrow H_2O_2$	0.5
$^{\bullet}OH + {}^{\bullet}H \rightarrow H_2O$	3.2
$H_3O^{+} + OH^{-} \rightarrow 2H_2O$	14.3

The yield of the primary species during radiolysis of water depends on the pH of the solution *[47, 53]*. The acid base properties of the primary species and also the reaction of these with H_3O^{+} and $^{\bullet}OH$ suggest that pH markedly influences the reactions occurring in irradiated water. Figure 1.6 shows the yield of the primary species as a function of the pH of the irradiated aqueous solution.

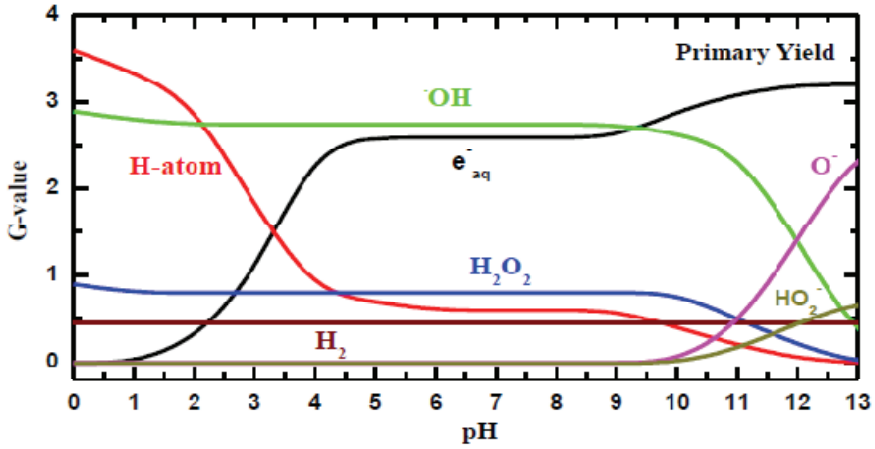

Figure 1.6 *Effect of pH on the yield of the primary species during water irradiation.*

At lower pH than 4, e^-_{aq} is rapidly scavenged by H_3O^+ resulting into H-atom. In the acidic region, due to high concentration of hydrogen ions, e^-_{aq} are scavenged within the spurs and tracks, thus the overall radical and molecular product yields in the acidic region are rather higher than in neutral and basic solutions. In basic region (pH > 11) $^{\bullet}OH$ radicals and H_2O_2 dissociate to give the oxide ion and a peroxide ion, respectively.

$$^{\bullet}OH + H_2O \leftrightarrow H_3O^+ + O^{\bullet -}; (pK_a = 11.9) \quad (1.23)$$

$$H_2O_2 + H_2O \leftrightarrow H_3O^+ + HO_2^-; (pK_a = 11.6) \quad (1.24)$$

The perhydroxyl radical ($HO_2^{\bullet}$) is a minor product when pure water is irradiated, but its yield increases in the presence of air or oxygen. It dissociates at pH > 4 to produce $O_2^{\bullet -}$, which is also an oxidizing radical.

$$HO_2^{\bullet} + H_2O \leftrightarrow H_3O^+ + O_2^{\bullet -}; (pK_a = 4.8) \quad (1.25)$$

The e^-_{aq} is a strong reducing agent (E_0 = -2.9 V vs. NHE). The reaction of e^-_{aq} with an organic molecule of interest can be monitored by using pulse radiolysis combined with kinetic spectrophotometer because of its intense and well separated

absorption band at 715 nm *[54, 55]*. The e_{aq}^- has sufficiently long half life in water, since the rate constant (k) of the reaction of e_{aq}^- with water is only 16 M^{-1} s^{-1} because water has no low lying vacant orbital to accept that electron.

H-atom ($^\bullet H$) does not get any importance in neutral and alkaline solution due to its low G value. However, it is a major reducing radical in acidic media. It is a less powerful reducing agent than e^-_{aq} having E_0 = -2.3 V *vs*. NHE. It is a weak acid (Eq. 1.26)

$$^\bullet H + H_2O \leftrightarrow e_{aq}^- + H_3O^+;\ (pK_a = 9.6) \qquad (1.26)$$

$^\bullet H$ can abstract one H-atom from organic molecules producing H_2 and it can adjoin to the double bond or to the aromatic ring. $^\bullet H$ absorbs at around 200 nm, which is normally not accessible with the available experimental facilities. Therefore, the reaction of $^\bullet H$ with organic molecule is monitored by competition kinetics method or from the formation kinetics of the reaction transient.

$HO_2^\bullet$ and its conjugate base, $O_2^{\bullet-}$ (Eq. 1.25) are important secondary radicals formed in O_2 saturated aqueous solution according to *Eqs. 1.27 & 1.28*. A comparative evaluation of the properties of $HO_2^\bullet$ and $O_2^{\bullet-}$ suggests that $O_2^{\bullet-}$ (E_0 = -0.155 V vs. NHE) is a stronger reducing agent than $HO_2^\bullet$ (E_0 = -0.05 V vs. NHE) *[56]*.

$$^\bullet H + O_2 \rightarrow HO_2^\bullet \qquad (1.27)$$

$$e_{aq}^- + O_2 \rightarrow O_2^{\bullet-} \qquad (1.28)$$

$^\bullet OH$ is the main oxidizing radical (E_0 = 2.72 V *vs*. NHE in acidic solution and $E_0^{'}$ = 1.89 V *vs*. NHE in neutral solution) produced upon water radiolysis *[57]*. $^\bullet OH$ has a weak absorption having absorption maxima (λ_{max}) at 230 nm and molar extinction coefficient (ε) = 530 M^{-1} cm^{-1} at 230 nm *[58]*. Therefore, it is difficult to determine the

rate constant of reaction of $^{\bullet}OH$ with an organic molecule by following only the decay of $^{\bullet}OH$. The rate constant of that reaction is rather measured either by a completion kinetic method or by pulse radiolysis by following the formation of the transient product, which has sufficiently high ε. $^{\bullet}OH$ is less selective than H-atoms for H-abstraction reaction, because the formation energy of H-OH bond (489 kJ mol^{-1}) is 57 kJ mol^{-1} more exothermic compared to the formation energy of H-H bond (432 kJ mol^{-1}). $^{\bullet}OH$ has following acid-base reaction (Eq. 1.23).

$O^{\bullet-}$ reacts more slowly compared to $^{\bullet}OH$ with several inorganic ions. The $^{\bullet}OH$ behaves as an electrophile, while $O^{\bullet-}$ behaves as a nucleophile. Thus, $^{\bullet}OH$ can readily add to π-system; while $O^{\bullet-}$ can not add to π-system.

1.3.6. Radicals of interest during radiolysis of water and their selective generation

Radiolysis of water produces charge species e_{aq}^{-}, $O_2^{\bullet-}$, H_3O^{+}; radicals $^{\bullet}OH$, $^{\bullet}H$, $HO_2^{\bullet}$ and molecular products H_2 & H_2O_2. Therefore, both the oxidizing and reducing species exist in the irradiated water. To extend the range of pulse and steady-state radiolysis experiments for chemical applications, it is desirable to modify the reaction system dominated by either oxidizing or reducing species. This can be achieved by two ways; (i) inter conversion of the primary species into a single kind of secondary radicals; and (ii) converting the unwanted primary radicals into relatively un-reactive secondary radicals. Table 1.3 shows the relevant reactions for predominantly producing rediolytic species of interest.

Table 1.3 *Relevant reactions for predominantly producing rediolytic species of interest.*

Predominant Radical of interest	Solute/ Purging gas	Reaction	Eq.	E_0 (V vs. NHE)
$^{\bullet}OH$	N_2O	$e_{aq}^- + N_2O \rightarrow N_2 + O^{\bullet -} \rightarrow OH^- + {}^{\bullet}OH$	(1.29)	2.72
$N_3^{\bullet}$	N_3^-	$N_3^- + {}^{\bullet}OH \rightarrow N_3^{\bullet} + OH^-$	(1.30)	1.3
$Cl_2^{\bullet -}$	NaCl	$Cl^- + {}^{\bullet}OH \rightarrow HOCl^{\bullet -}$ $HOCl^{\bullet -} + H^+ \rightarrow H_2O + Cl^{\bullet}$ $Cl^{\bullet} + Cl^- \rightarrow Cl_2^{\bullet -}$	(1.31) (1.32) (1.33)	2.1
$SO_4^{\bullet -}$	$S_2O_8^{2-}$	$e^-_{aq} + S_2O_8^{2-} \rightarrow SO_4^{\bullet -} + SO_4^{2-}$	(1.34)	2.6
e^-_{aq}	tert-butanol/N_2	$(CH_3)_3COH + {}^{\bullet}OH \rightarrow (CH_3)_2C^{\bullet}H_2OH + H_2O$	(1.35)	-2.9
$(CH_3)_2C^{\bullet}OH$	$(CH_3)_2CHOH$ /N_2O	${}^{\bullet}OH + (CH_3)_2CHOH \rightarrow H_2O + (CH_3)_2C^{\bullet}OH$ ${}^{\bullet}H + (CH_3)_2CHOH \rightarrow H_2 + (CH_3)_2C^{\bullet}OH$	(1.36) (1.37)	-1.8
$CO_2^{\bullet -}$	HCOONa/ N_2O	$HCOO^- + {}^{\bullet}OH\ ({}^{\bullet}H) \rightarrow CO_2^{\bullet -} + H_2O\ (H_2)$	(1.38)	-1.9

CHAPTER 2

Experimental

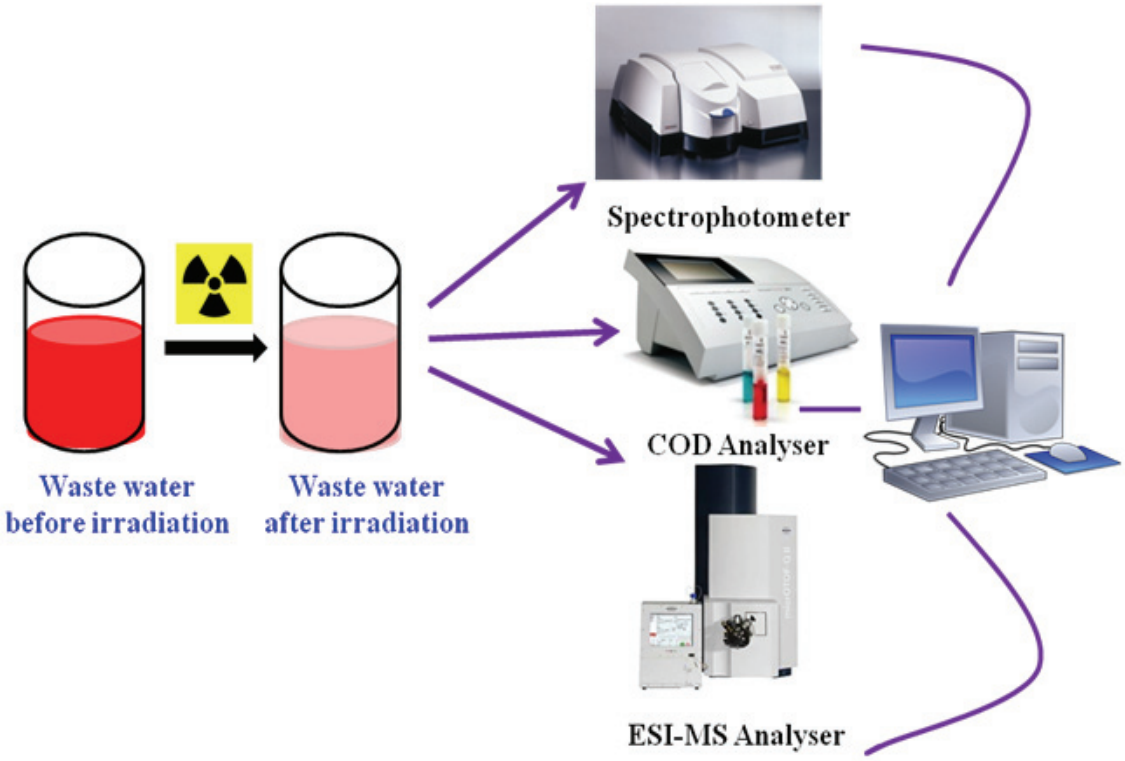

The following experimental techniques or procedures were employed during the course of the study.

2.1. Linear Electron Accelerator (LINAC)

2.1.1. 7 MeV LINAC

A 7 MeV nanosecond LINAC pulse radiolysis technique was used to determine fast reaction kinetics. A highly short intense pulse of beam current of electrons is given to a system to achieve a non-equilibrium situation in which significant concentration of transient species is produced in a short time interval and these transient species are monitored following the changes in their optical absorption *[59]*. The LINAC assembly available at the institution is from M/s Viritech, U.K. (formerly M/s Radiation Dynamics, U.K.). The essential components of a 7 MeV LINAC are (i) electron gun and (ii) wave guide. A 2 μs electron pulse of energy 43 keV is generated in electron gun and these electrons are allowed to enter into the wave guide in a phase synchronous with the radio frequency (R.F.) field (generated by magnetron). The electrons are accelerated in vacuum (10^{-8} mbar) into the wave guide to the final energy of 7 MeV. The parameters for 7 MeV LINAC during the experiment are summarized in Table 2.1.

Table 2.1 *Specifications of 7MeV LINAC*

Electron energy	Pulse Width (ns)	Peak current (mA)	RF Frequency (MHz)
7 MeV	500	90	3000

2.1.1.1. Kinetic spectrophotometer

The transient behaviour in pulse radiolysis is monitored by the most popular technique of absorption spectroscopy. The different units of the analyzing set-up consists of (i) 450 W Xenon arc lamp as the analyzing light source (wavelength range 250-850 nm), (ii) Optical components like electromechanical shutter (to prevent photodecomposition of the samples during the passive mode), light filters, lenses and mirrors, monochromator (with usable range of 180-850 nm with a dispersion of 3 nm mm^{-1}) and photomultiplier detector (with spectral response in the working range of 200-900 nm and rise time of detection of 75 ns) and (iii) recorder i.e., oscilloscope, computer and printer.

2.1.1.2. Analysis of the recorded signal

The transient signal obtained is plot of signal (mV), which is proportional to intensity of the absorbed light (I_{abs}), versus time. These signals are converted into optical density (O.D.) using Eq. 2.1.

$$O.D. = \log\frac{I_1}{I_2} \qquad (2.1)$$

where, I_1 is the intensity of the light passing to the solution before pulse and I_2 is the intensity of the light transmitted to the solution after pulse. After substituting I_0 by DC (mV), which is the difference of the PMT output under identical conditions with and without the analyzing light and I_t by [DC(mV) - Signal(mV)], Eq. 2.1 turns to Eq. 2.2.

$$O.D. = \log\left(\frac{DC(mV)}{\{DC\ (mV) - Signal\ (mV)\}}\right) \qquad (2.2)$$

To obtain the absorption spectrum of a transient species, the O.D. value is plotted as a function of the wavelength of the analyzing light at a selected time.

2.1.1.3. Corrected transient absorption spectra and molar absorptivity

A fraction of the parent molecules is lost in a radiation chemical reaction. The transient absorption is given by Eq. 2.3

$$\Delta A = (\varepsilon_t - \varepsilon_p)\, C_t\, l \qquad (2.3)$$

where, ΔA is observed absorbance, ε_t and ε_p are the extinction coefficients of the transient and the parent molecule at a particular wavelength, C_t is the concentration of the transient produced and l is the optical path length. When the absorptions due to the parent molecule and the transient formed overlap, the observed absorbance does not represent the true characteristics of the transient. Thus, a correction term for the amount of parent molecules depleted needs to be included in the calculation.

The molar absorptivity of a transient can be estimated as follows. The concentration of the transient of interest is obtained from the absorbed dose, measured by thiocyanate dosimetry. Under identical condition, the two absorbances are related by Eq. 2.4.

$$\frac{A^{\lambda}_{sample}}{(G.\varepsilon)^{\lambda}_{sample}} = \frac{A^{500nm}_{dosimeter}}{(G.\varepsilon)^{500nm}_{dosimeter}} \qquad (2.4)$$

In case the parent molecule also has absorption at wavelength λ, then Eq. 2.3 is modified as Eq. 2.5.

$$\varepsilon^{\lambda}_{sample} = \varepsilon^{\lambda}_{parent} + \frac{A^{\lambda}_{sample}}{G_{sample}} \cdot \frac{(G\varepsilon)^{500nm}_{dosimeter}}{A^{500nm}_{dosimeter}} \qquad (2.5)$$

2.1.1.4. Dosimetry for Pulse Radiolysis

An aerated aqueous solution of 20 mM potassium thiocyanate (KSCN) is used to measure the absorbed dose per pulse. Amongst the primary radicals produced, $^{\bullet}H$ and e^{-}_{aq} are scavenged by the dissolved oxygen. The $^{\bullet}OH$ oxidizes CNS^{-} ions producing $(SCN)_2^{\bullet-}$ according to Eqs. 2.6 & 2.7.

$$CNS^{-} + {}^{\bullet}OH \rightarrow CNS^{\bullet} + OH^{-} \qquad (2.6)$$

$$CNS^{\bullet} + CNS^{-} \rightarrow (CNS)_2^{\bullet-} \qquad (2.7)$$

The G.ε value for this species is reported to be 2.15×10^{4} M^{-1} cm^{-1} or 2.23×10^{-4} m^2 J^{-1} with G = 2.9 at 500 nm for 100 eV energy absorbed *[60]*. From the measured absorbance (A), the absorbed dose per pulse (D) is computed from Eq. 2.8.

$$D = \frac{A.N.100}{G\varepsilon.1000} \text{ eV cm}^{-3} \qquad (2.8)$$

The above equation is simplified by substituting appropriate numerical values of G, ε and N (Avogadro number), one can get

$$D = 2.8 \,.\, A.\, 10^{18} \text{ eV cm}^{-3} \qquad (2.9)$$

The absorbed dose in the units of Gy is obtained by multiplying the value of A by a factor 448.6. Generally the maximum dose obtained from a 25 ns pulse is 10 Gy and that for a 2 μs pulse is about 120 Gy.

2.1.2. 2 MeV Linear Electron Accelerator

The pulse linear electron beam accelerator of ILU-6 type is obtained from Budker Institute of Nuclear Physics, Russia. The accelerator is based on resonator cavity inductively coupled to a self-excited RF generator (120 MHz) and can be operated up to energy 2 MeV and average 20 kW power with a repetition rate of 50 Hz *[61]*. The machine is designed to deliver an average dose of about 33 kGy s^{-1} at the centre. The machine is housed in a shielded cell having a labyrinth with separate entry and exit ports where power roller conveyor system has been installed for the material transport in & out of the irradiation zone. The electrons are injected in the cavity and accelerated in a single step to attain the energy of 2 MeV. A vacuum of 10^{-6} torr is maintained in the cavity. The output beam is extracted in to the atmosphere in pulse form with 500 μs and each pulse is scanned over a length of 100 cm.

2.1.2.1. Dosimetry of electron beam accelerator

Dosimetry was performed using a FWT60 radiochromic film dosimeter calibrated using graphite calorimeter *[62]*. ILU- 6 pulse accelerator parameters during the experiment were as follows:

Table 2.2 *Specifications of 2 MeV LINA*C

Electron energy (Mev)	**Pulse Repetition frequency (Hz)**	**Average bean current current (mA)**	**Beam power (kW)**	**conveyor speed (cm s^{-1})**
2	50	1.2	20	10

2.1.3. 10 MeV Linear Electron Accelerator

A 10 MeV RF electron LINAC was also used in the present study. The electron beam at 50 keV in electron gun with LaB_6 cathode is injected into the on-axis coupled cavity LINAC which accelerates the electron to a maximum energy to 10 MeV. Dose rate was maintained at 10 kGy/pass. 10 MeV accelerator parameters during the experiment were as follows:

Table 2.3 *Specifications of 10 MeV LINAC.*

Electron energy (MeV)	Pulse Repetition frequency (Hz)	Average bean current current (mA)	Beam power (kW)	conveyor speed (cm s^{-1})
10	300	33	1	1.67

2.2. Cobalt-60 Gamma Source [GC-5000]

γ-ray emitting ^{60}Co radioisotope is produced by irradiating natural cobalt (^{59}Co) in the form of pellets or small slugs or thin disks in nuclear reactor by $^{59}Co(n,\beta)^{60}Co$ reaction. It gives uniformly active material which emits β particle followed by two γ-rays of energy 1.33 MeV and 1.17 MeV. The walls of the metal container filters out β radiation emitted by ^{60}Co. Gamma irradiation of the samples were carried at room temperature using Gamma Chambers *GC-5000,* which were supplied by the Board of Radiation & Isotope Technology, Mumbai, India. Figure 2.1 shows one of the gamma chambers used for our studies. The gamma chamber mainly consists of a set of stationary ^{60}Co sources placed in a cylindrical cage surrounded by a lead shield provided around the source to keep external radiation field well within the permissible limits. The material for irradiation is placed in

an irradiation chamber located in the vertical drawer inside the lead flask. The particular gamma source used in the experiments produces a dose rate of 3 or 2.5 kGy hr^{-1}.

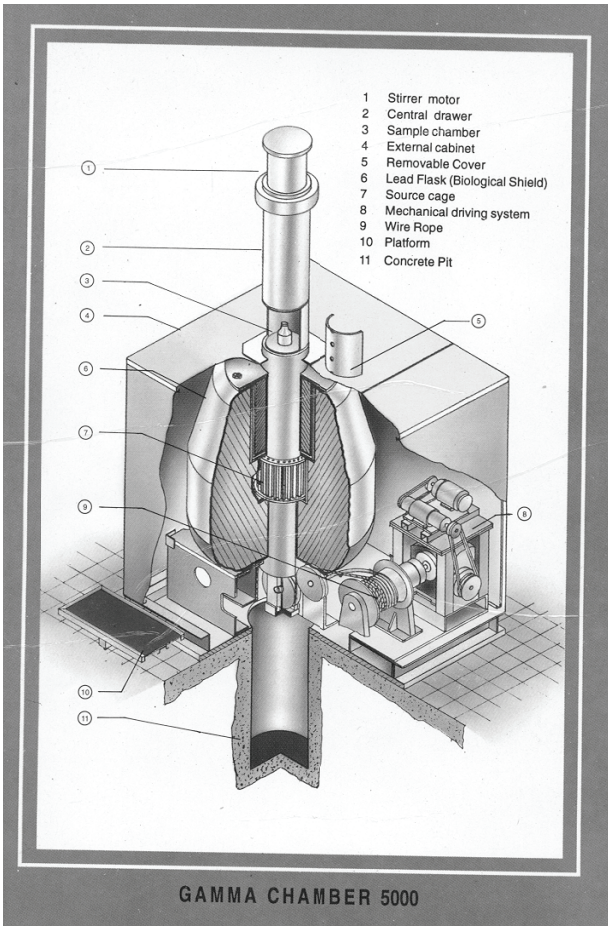

Figure 2.1 *Gamma Chamber 5000.*

2.2.1 Dosimetry for ^{60}Co Gamma Source

In general, Fricke (ferrous sulfate) dosimeter is used for the dose measurement of ^{60}Co γ source *[63]*. The principle involved is the radiation induced oxidation of ferrous ion to ferric ion at low pH and in presence of oxygen. The standard dosimetric solution

contains 1 mM ferrous sulfate, 1 mM NaCl in 0.4 M H_2SO_4 (pH 0.46). The solution is saturated with oxygen. The reactions involved are given in Eqs. 2.10-2.16.

$$e_{aq}^- + H^+ \rightarrow {}^\bullet H \qquad (2.10)$$

$${}^\bullet H + O_2 \rightarrow HO_2^\bullet \qquad (2.11)$$

$${}^\bullet OH + Fe^{2+} \rightarrow OH^- + Fe^{3+} \qquad (2.12)$$

$$HO_2^\bullet + Fe^{2+} \rightarrow HO_2^- + Fe^{3+} \qquad (2.13)$$

$$HO_2^- + H^+ \rightarrow H_2O_2 \qquad (2.14)$$

$$H_2O_2 + Fe^{2+} \rightarrow OH^- + {}^\bullet OH + Fe^{3+} \qquad (2.15)$$

$$G(Fe^{3+}) = 2\,G(H_2O_2) + 3\,[G(e_{aq}^-) + G({}^\bullet H) + G(HO_2^\bullet)] + G({}^\bullet OH) \qquad (2.16)$$

The $G(Fe^{3+})$ is calculated as 15.5 by substituting the G values of the primary radicals. The spectrophotometric method is mostly used to measure the concentration of ferric ion formed by comparing the absorbance of the irradiated and non-irradiated dosimeter solutions at the wavelength at which ferric ion shows maximum absorption (about 304 nm). The optical readings should be taken soon after irradiation so that adventitious oxidation of the solutions is minimized. The mean absorbed dose (D_D) for the volume occupied by dosimeter solution is given by Eq. 2.17.

$$D_D = \frac{9.684x10^6 \Delta A_D}{\Delta\varepsilon l \rho G(P)} Gy \qquad (2.17)$$

where, ΔA_D is the change in absorbance of dosimeter solution before and after irradiation. G(P) is yield (number of molecules per 100 eV) of ferric ions due to irradiation, $\Delta\varepsilon$ is

extinction coefficient (M^{-1} cm^{-1}) of ferric ions at the measuring wavelength, ρ is the density (g cm^{-3}) of dosimeter solution, l is the path length (cm).

2.3. Chemical Oxygen Demand

The COD test is commonly used to measure the amount of organic compounds in water. It is expressed in milligrams of oxygen consumed per liter (mg L^{-1}) of solution. Sometimes, it is also expressed in ppm (parts per million). The organic compound is fully oxidized to carbon dioxide and water by a strong oxidizing agent under high temperature. In this method, the solution containing organic compound is digested at 120°C in presence of $K_2Cr_2O_7$ and H_2SO_4 in a closed reactor called "thermoreactor" and then the amount of consumed $K_2Cr_2O_7$ (which is equivalent to the amount of O_2 consumed for the oxidation) is determined by spectrophotometrically (Figure 2.2).

Figure 2.2 *(a) Thermoreactor and (b) spectrophotometer for COD measurement.*

The amount of equivalent oxygen required for oxidising an organic compound ($C_nH_aO_bN_c$) to carbon dioxide, ammonia, and water is given by Eq. 2.18.

$$\boldsymbol{C_nH_aO_bN_c + \left(n + \frac{a}{4} - \frac{b}{2} - \frac{3}{4}c\right) O_2 \rightarrow nCO_2 + \left(\frac{a}{2} - \frac{3}{2}c\right) H_2O + cNH_3} \qquad (2.18)$$

In the present studies, the COD of the solutions were measured by using Spectroquant® Pharo 300 COD analyser from M/s. Merck, Germany.

2.4. Total Organic Carbon

Total organic carbon (TOC) represents the amount of carbon bound in an organic compound. The TOC analysis of a solution has three main steps viz. (i) acidification and purging with inert gas (removes inorganic carbon), (ii) photocatalytic oxidation of carbon content to CO_2 and (iii) detection and quantification of CO_2 by non-destructive infrared method. The TOCs of the solutions were measured in this study by using ANATOC II TOC analyser from SGE Australia (Figure 2.3).

Figure 2.3 *Total organic carbon analyser.*

2.5. Biological Oxygen Demand (BOD)

Biochemical oxygen demand is the amount of dissolved oxygen needed by aerobic biological organisms in water to degrade organic molecules present in water at certain temperature over a specific time period. The BOD value is most commonly expressed in milligrams of oxygen consumed per litre of sample water during 5 days of incubation at 20 °C. BOD measures the amount of the biodegradable fraction of the organic molecules

present in the polluted water. BOD was measured by using Eutech DO meter (Cyberscan DO6000) from M/s. Merck, Germany. The BOD bottles were incubated at 20°C for 5 days and difference in dissolve oxygen (DO) was used to calculate BOD_5 (APHA1998). The BOD values are expressed in mg L^{-1} according to Eq. 2.19.

$$\text{BOD (mg L}^{-1}) = \frac{(D_1 - D_5)}{p} \qquad (2.19)$$

where, D_1 and D_5 are the initial and final DO of sample dilution (in mg L^{-1}); P is the decimal volumetric function of sample used.

2.6. UV-Visible spectrophotometer and pH meter

The spectrophotometric measurement was carried out by Hitachi U-2800 UV-Vis sphectrophotometer. The pH of the solution was measured by using pH meter 600.

2.7. Gas chromatography mass spectrometry

Gas chromatography mass spectrometry (GC-MS) is used for separating and analyzing compounds that can be vaporized without decomposition. The GC-MS analysis was carried out by using a Shimadzu 2010 MS, equipped with integrated gas chromatograph. In GC, the components are separated based on their distribution coefficient between non polar, nonvolatile liquid stationary phase (100% dimethyl-polysiloxane (60 mm long, 0.25 mm inner diameter)) and gaseous mobile phase (Helium, flow rate: 13 mL min^{-1}). The column is held in an oven that can be programmed to increase the temperature gradually. As the temperature increases, that compounds which have low boiling points elute from the column sooner than those that have higher boiling points and show lesser retention time. Then the components are detected by respective m/z ratio by mass

spectrometer which consists of an ion source (EI), an analyzer (quadrupole) and a detector (microchannel plate detector). The injector temperature in the study was kept at 280^{o}C which was programmed as follows: 80°C kept constant for 2 min, increased up to 200^{o}C with 10^{o}C min^{-1}, and raised up to 280^{o}C with 20°C min^{-1} rate. The compounds were identified on the basis of m/z values by using the NIST library.

2.8. High-performance liquid chromatography

High-performance liquid chromatography (HPLC) is an analytical technique used to separate and identify the components of a mixture. The reversed phase HPLC experiment was performed by using Waters (Model 2690). The important components of HPLC are the solvent delivery system, sample injector, column, detector and data processor. The preparation of samples for HPLC analysis follows the same procedure as described in for the FTIR analysis (Section 2.10). The components are separated by the distribution coefficient between non polar stationary phase (C-18 column (symmetry, 4.6 mm × 250 mm) and polar liquid mobile phase (HPLC grade methanol with an isocratic flow rate 0.50 mL min^{-1}). More polar compound will elute earlier due to lesser extent of interaction with stationary phase and show lesser retention time. The eluted components were detected by UV detector with a fixed wavelength at 280 nm in the present study.

2.9. Electrospray Ionization Mass Spectrometry (ESI-MS)

In the study electrospray ionization (ESI) technique was used as the ion source in mass spectrometry (MS) to produce ions. MS is an analytical chemistry technique that helps to identify the amount and type of ions generated by measuring the mass-to-charge ratio and abundance of gas-phase ions. MS consists of a time of flight mass analyzer and a

detector (electron multiplier).A negative ion mode electrospray mass spectrometer with Quadruple-Time-of-Flight analyzer (model micrOToFQ-II, Bruker Daltonik GmbH) was used in a part of the present study where aqueous dye solutions were directly infused with an automatic syringe pump (NEMESYS from cetrol GmbH). A high voltage is applied to the liquid to create a spray of charged droplets called aerosol. The charged droplets are migrated under the influence of the potential where a flow of heated nitrogen dries the droplets and carries away uncharged mobile phase molecules. This process results in the continuous shrinkage of the droplet size until the repulsive electrostatic forces exceed the surface tension, leading to droplet explosions as indicated in the inset of the Figure 2.4. Other parameters for negative mode ESI were: end plate offset: -1000 V; dry heater temperature: 100 ^{o}C; capillary voltage: 3000 V; dry gas flow rate: 4.0 L min^{-1}; nebulizer gas: 30 kPa and collision energy was kept at 1 eV to avoid heavy in-source fragmentation.

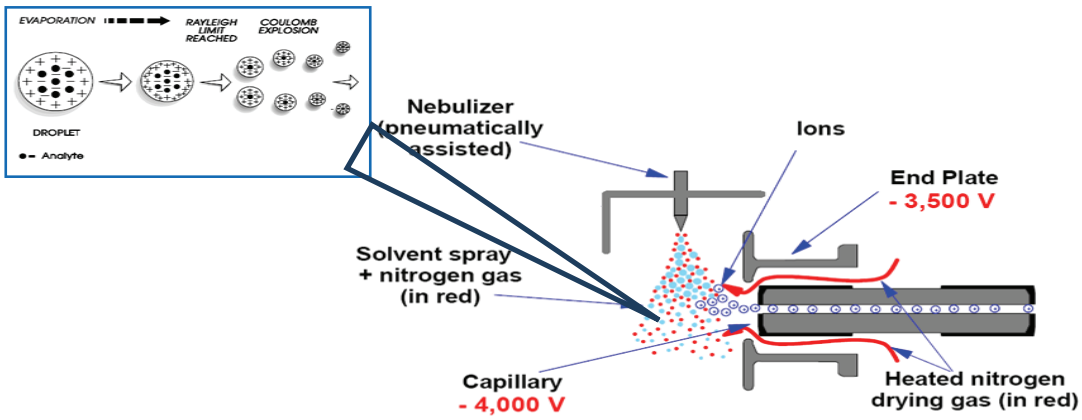

Figure 2.4 *Schematic of electrospray ionisation system.*

2.10 Fourier transformed infrared spectroscopy

Fourier transformed infrared (FTIR) spectroscopy is an important analysis technique that detects various characteristic functional groups present in the sample. In this study the FTIR spectra of radiation, microbiological and combined radiation-microbiological treated dye solutions were recorded by using Perkin-Elmer 783 Spectrophotometer. In the first set of samples, the irradiated solutions were evaporated to dryness in rotary evaporator and employed for FTIR analysis. For the other two sets, after complete decolouration, the decolourised media was centrifuged at 5000 rpm for 20 min and the metabolites were extracted from the supernatant by equal volume of ethyl acetate. The extract was dried over anhydrous Na_2SO_4 and was evaporated to dryness in rotary evaporator. The crystals obtained were mixed with anhydrous KBr in the 5:95 weight percentages and pressed into pellets under high pressure and used for FTIR analysis. The % transmittance of the samples was measured at different wavenumbers in the range between 400-4000 cm^{-1} by averaging 16 scans for each spectrum.

2.11. Photocatalytic reactor

The photocatalytic experiments were carried out by using Rayonet Photochemical Reactor. The light source contains 16 mercury lamps of 8 W power each and emitting in the near-UV (mainly around 350 nm) having incident radiation intensity (I_0) of 5.0×10^{15} photons cm^{-2} s^{-1}. The volume and area of the photoreactor chamber are V (250 cm^3) and A_{cell} (32 cm^2), respectively.

2.12. Ozone reactor

Ozone was continuously produced from pure oxygen by UOS04 model ozone generator and bubbled into the aqueous solution. The ozone generator can produce 4 g h^{-1} ozone from pure oxygen feed of 2 L min^{-1}. The input rate of ozone from the ozone generator into the aqueous solution was determined as 7.3×10^{-3} mol m^{-3} min^{-1} by the standard iodometric method.

2.13. Chemicals and Reagents

Reactive Red 120 (RR-120), 2,2-azino-bis(3-ethylbenzothiazoline-6-sulphonic acid) (ABTS), sodium dodecylbenzenesulfonate (SDBS), sodium dodecylsulphate (SDS), potassium persulfate ($K_2S_2O_8$), tert-butanol (^{t}Bu-OH) were purchased from Sigma-Aldrich, India. L-tyrosine, Methyl Red (MR) and microbiological media (such as nutrient broth) were obtained from Hi-Media Laboratory, India. 2,6-dichlorophenol indophenol (DCIP) and NADH were purchased from Sisco Research Laboratory, India. All chemicals used were of the highest purity and were used as such. Millipore water was used for the pulse radiolysis, COD, TOC, HPLC, GC-MS, ESI-MS measurements.

2.14. Enzyme assay

The activity of laccase, tyrosinase, azoreductase and NADH-DCIP reductase was studied in the cell free extracts obtained from the test solutions.

2.14.1. Determination of laccase activity

Laccase activity was determined in a 2.0 mL reaction mixture containing 10% ABTS in 20 mM potassium phosphate buffer (pH 4.0). The reaction was started by adding 0.2 mL

of enzyme solution and the increase in the optical density was measured at 420 nm *[64]*. One unit of enzyme activity was defined as μM of ABTS oxidized min^{-1} mL^{-1} of enzyme. The molar extinction coefficient of ABTS is 34450 M^{-1} cm^{-1} at 420 nm.

2.14.2. Determination of tyrosinase activity

Tyrosinase activity was determined in a 3.0 mL reaction mixture containing 2.5 mL of sodium acetate buffer (20 mM, pH 4.0) and 100 μM of L-tyrosine. The reaction was started by adding 0.2 mL of enzyme solution and increase in absorbance was measured at 280 nm *[65]*. One unit of enzyme activity was defined as a change in absorbance units min^{-1} mL^{-1} of enzyme. Molar extinction coefficient of L-Tyrosine is 1420 $M^{-1}cm^{-1}$ at 280 nm.

2.14.3. Determination of azoreductase activity

Azoreductase assay mixture (2.0 mL) contained 4.45 μM MR, 50 mM potassium phosphate buffer (pH 7.5) and 0.2 mL of enzyme solution. The reaction was started by adding 100 μM of NADH and then the absorbance was monitored at 430 nm. The molar extinction coefficient of MR is 2.34×10^4 M^{-1} cm^{-1} at 430 nm *[66]*. One unit of enzyme activity was defined as μM of MR reduced min^{-1} mL^{-1} of enzyme.

2.14.4. Determination of NADH-DCIP activity

NADH-DCIP reductase assay mixture (5.0 mL) contained 25 μM DCIP, 50 mM potassium phosphate buffer (pH 7.5) and 0.2 mL of enzyme solution. The reaction was started by adding 100 μM of NADH into the assay mixture. The absorbance was measured at 595 nm. The molar extinction coefficient of DCIP is 1.9×10^4 M^{-1} cm^{-1} at 595 nm *[67]*.

One unit of NADH-DCIP reductase activity was defined as μM of DCIP reduced min^{-1} mL^{-1} of enzyme.

2.15. Method of sample preparation for the toxicity study of the treated dye solution on plants

The metabolites produced in the test solution were extracted from the supernatant by equal volume of ethyl acetate and the extract was dried over anhydrous Na_2SO_4 and was finally evaporated to dryness in rotary evaporator. The extracted products were dissolved in sterile distilled water to make a final concentration of 600 ppm. Toxicity study was carried out by watering the seeds with 10 mL of 600 ppm sample solution. The toxicity of the original dye solution was studied with 10 mL of 600 ppm dye solution in the same time interval.

2.16. Micro-organisms and culture conditions

The stock culture of Pseudomonas sp. SUK1 was maintained on nutrient agar slants which was stored in sealed tubes at 4 °C and sub-cultured monthly to maintain viability. The pure culture of Pseudomonas sp. SUK1 was grown for 24 h in 250 mL Erlenmeyer flask containing 100 mL nutrient broth having 10, 5, 2 and 1 g L^{-1} peptone, NaCl, yeast extract and beef extract, respectively, by using a static temperature controlled incubator at 30 ± 2 ºC (which is the optimum growth temperature of Pseudomonas sp. SUK1).

2.17. Microbial treatment

The grown bacterial cells having optical density (OD) 1.0 at 620 nm were inoculated in 250 mL Erlenmeyer flasks containing 100 mL nutrient broth followed by incubation

with dye solution at 30 ± 2 ºC under static condition up to 96 h as show in the Figure 2.5. Aliquots of 3 mL of the reaction medium were withdrawn at different time intervals and were centrifuged at 5000 rpm for 15 min. Then the absorbance of the supernatant liquid was measured at 535 nm, which is the characteristic wavelength of RR-120. The absorbance was measured in triplicate for each aliquot. The percentage decolouration at any time was calculated from the initial and final absorbances.

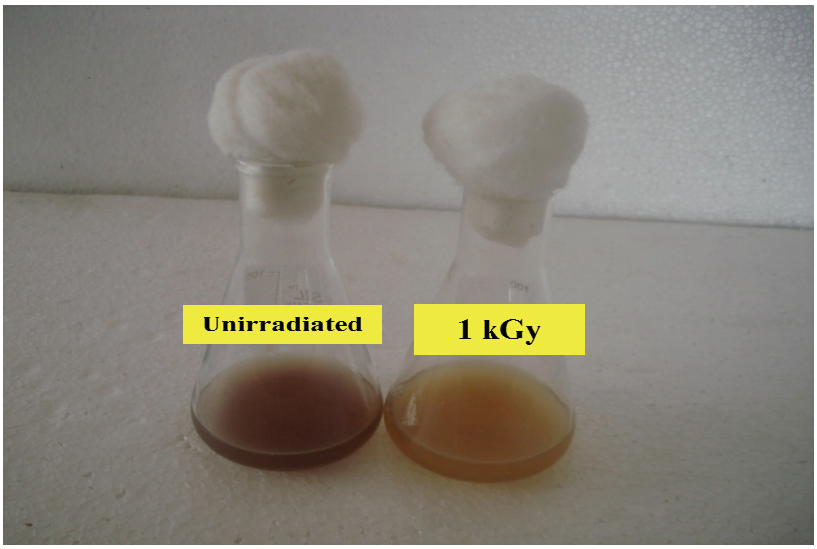

Figure 2.5 *Incubated dye solution at 30 ± 2 ºC under static condition up to 96 h.*

2.18. Preparation of the cell free extract

The grown cells of Pseudomonas sp. SUK1 were centrifuged at 10000 rpm for 20 min. These cells (75 g L^{-1}) were suspended in 50 mM potassium phosphate buffer (pH 7.4) and sonicated at 4 ºC for 6.5 min. Then the homogenate was centrifuged and supernatant was used as a source of enzyme for control.

CHAPTER 3

Decolouration and degradation of Reactive Red-120 dye

3.1. Radiolysis of aqueous solution of Reactive Red - 120

Dye is an organic compound that absorbs light in the visible range (i.e., 400 nm to 700 nm) of the electromagnetic spectrum. The physical colour of the dye is characterized by the complementary colour of the absorption band. The chromophore and auxochrome shift the absorption band in the visible region and intensify the colour. The reactive group helps to bind the dye molecule with the fibers and the sulphonic acid groups help in the solubility of dye in water. Destruction of the chromophore group of the dye causes the decolouration of the dye solution, whereas mineralization happens from the complete oxidation of the dye molecule.

3.1.1. Structure of Reactive Red - 120

The molecular structure of Reactive Red – 120 (RR-120) is shown in *Figure 3.1*. RR-120 bears two azo groups as the chromophoric moiety and two chlorotriazine groups as reactive groups. The hydroxyl groups present in the cellulose fibres forms covalent bond with RR-120 by the nucleophilic substitution of the chlorine atom of the chlorotriazine group. The phenyl and naphthol rings provide the extended π-conjugation through the azo group.

The UV-Visible absorbance spectrum of 40 μM aqueous RR-120 solution at pH 7 is shown in *Figure 3.2 (a)*. The peaks at (1) 235 nm and (2) 293 nm correspond to π-π^* transition of the benzene and naphthalene units of RR-120. The small hump (3) at 373 nm represents n- π^* transition from the nitrogen atoms of the azo group to the naphthalene ring *[68]*. The peaks at (4) 510 nm and (4') 538 nm represent two energetically closed π-π^* transition between the molecular orbitals formed by extended π conjugation including the benzene ring, azo linkage and naphthol ring *[68]*.

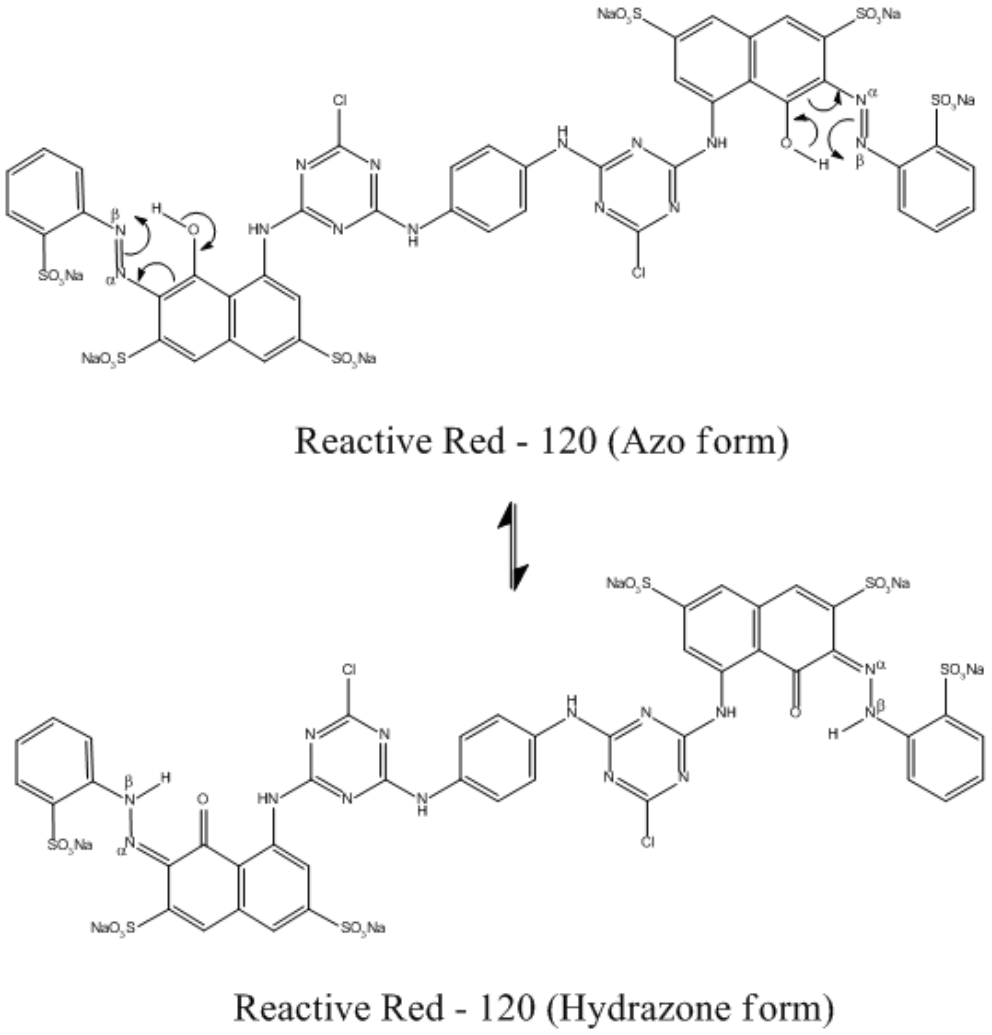

Figure 3.1 *Azo and Hydrazone tautomeric forms of Reactive Red – 120.*

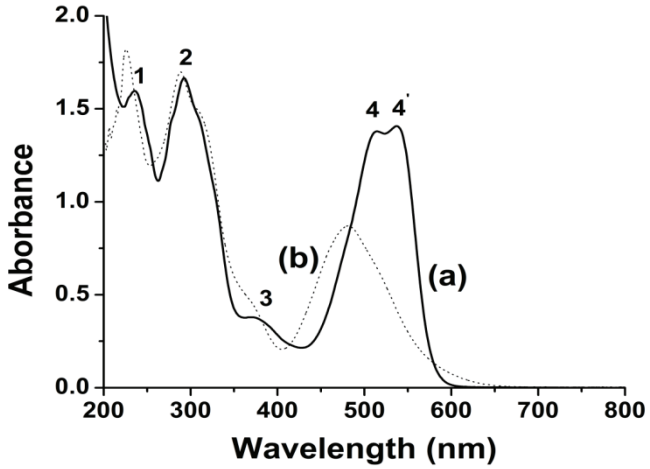

Figure 3.2 *UV-Visible spectra of aqueous solution of 40 μM RR-120 at (a) pH 7 and (b) pH 13.8.*

Upon increasing the pH of the solution to 13.8, the colour of the dye solution becomes orange, which is also evidenced from the shift of the visible band (4, 4') to lower wavelength *(Figure 3.2(b))*. The splitting peak (4 and 4') disappeared and a single peak appeared at 482 nm.

RR-120 has two tautomers viz. azo and hydrazone (*Figure 3.1*). The H-atom of the naphtholic unit (in azo form) is positioned at the *β*-N of azo linkage in the hydrazone form. The H-atom on the *β*-N of the azo group is shared by the oxo group of the naphthalene ring forming a six member ring in hydrazone tautomer. Therefore, long extended π-electron conjugation is evidenced in the hydrazone tautomer (*Figure 3.2(a)*). The tautomeric H-atom of the naphthol unit is abstracted by the HO^- ions at pH 13.8. This stops the formation of hydrazone tautomer, which is evidenced from the shift of the visible band of the spectrum to the lower wavelength (*Figure 3.2(b)*). The variation of absorbance with pH was more prominent at 450 and 550 nm.

Figure 3.3 shows the variation of optical density (OD) at 450 and 550 nm of aqueous solutions of 40 μM RR-120 as a function of pH. Therefore, pK_a of RR-120 corresponding to the dissociation of the naphtholic hydrogen was calculated as 12.5 from the point of intersection of the ODs at 450 and 550 nm as a function of pH (*Figure 3.3*). The higher pK_a value of RR-120 compared to other H-acids (i.e. phenol etc.) is attributed to the strength of the six member ring formed in the hydrazone tautomer involving the dissociating H-atom of RR-120.

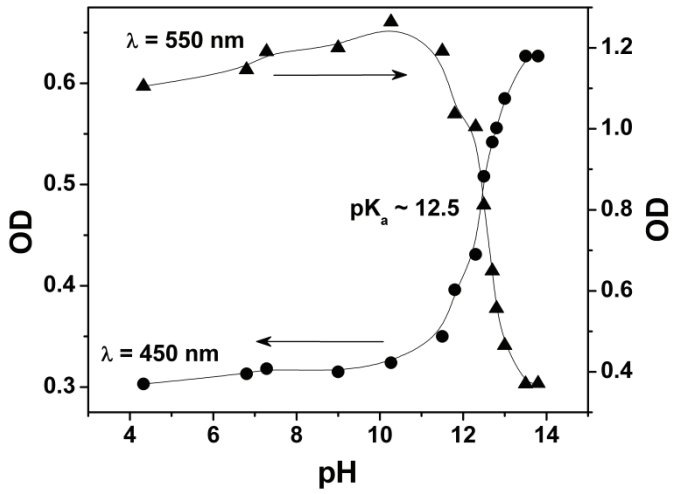

Figure 3.3 *Variation of OD at 450 and 550 nm of aqueous solution of 40 µM RR-120 as a function of pH.*

3.1.2. Radiolysis of RR-120 by Oxidising Radicals

3.1.2.1. Reaction of RR-120 with Hydroxyl Radical ($^{\bullet}$OH)

Aqueous solution of 40 µM RR-120 solution (at pH 7) was irradiated for different doses in ^{60}Co gamma chamber having a dose rate of 3 kGy h^{-1} (measured using Fricke dosimetry). During the radiolysis of water, hydroxyl radicals (yield of $^{\bullet}$OH = 0.28 µmol J^{-1}), hydrated electrons (yield of e^-_{aq} = 0.28 µmol J^{-1}) and hydrogen atoms (yield of $^{\bullet}$H = 0.06 µmol J^{-1}) are the three main reactive inter-mediates produced in the pH range between 3 and 11. The reaction between $^{\bullet}$OH and RR-120 was investigated in N_2O saturated solution, because e^-_{aq} is converted to $^{\bullet}$OH by N_2O as shown in *Eq. 1.29*. Under this reaction condition, the yield of $^{\bullet}$OH becomes 0.56 µmol J^{-1}.

Figure 3.4(a) shows the spectra of N_2O saturated 40 µM RR-120 solutions (at pH 7) (i) before radiolysis and after steady state radiolysis at (ii) 0.5, (iii) 1.0 and (iv) 2.0 kGy. The intensities of the peaks at 235, 293, 510 and 538 nm decreased with increasing dose. It is attributed to the destruction of the benzene, naphthalene and

extended π-conjugation of RR-120 by the oxidising $^{\bullet}$OH radical. Further, the doublet peaks at 510 and 538 nm merged during radiolysis to a single peak and developed significant absorption at higher wavelength than 600 nm (It should be noted that RR-120 has no absorption at λ > 600 nm). It suggests a possibility of the formation of more extended π-conjugated system compared to RR-120 by the addition of $^{\bullet}$OH to either benzene or naphthalene ring. However, the overall absorbance of RR-120 significantly decreased at 2.0 kGy.

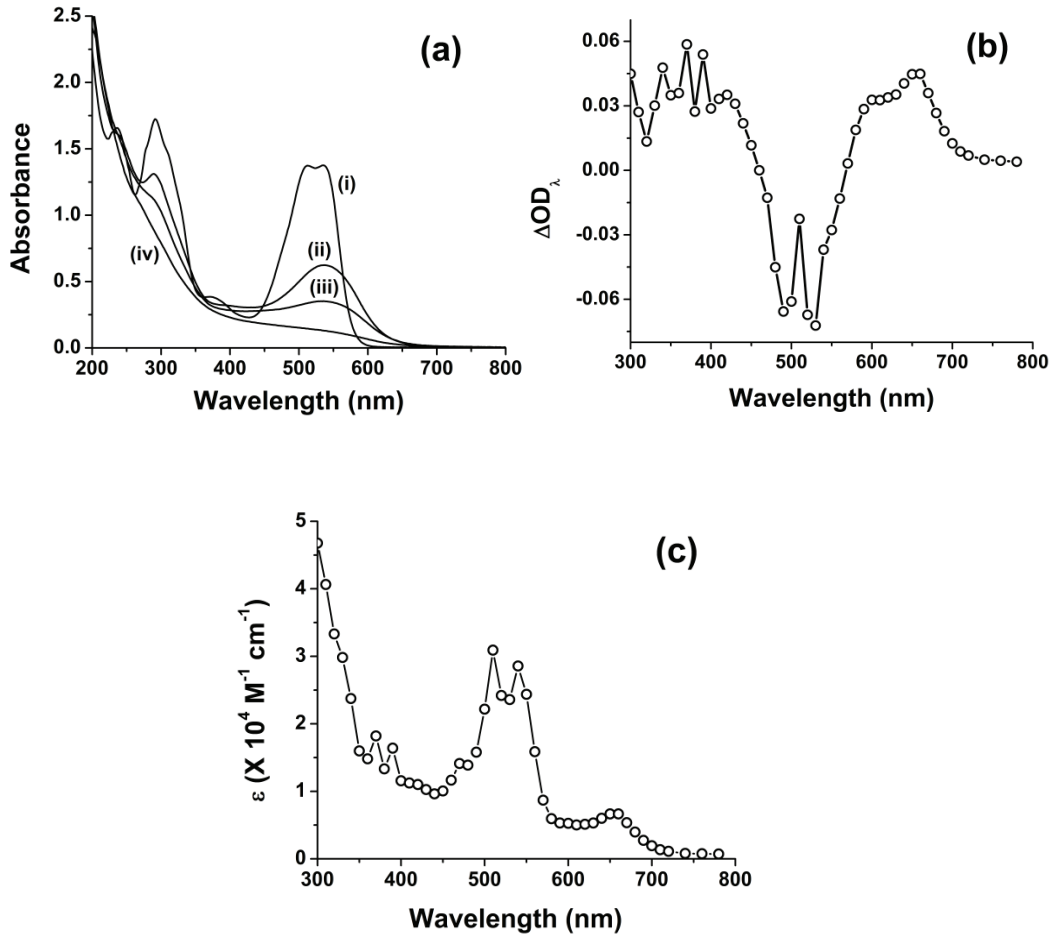

Figure 3.4 *(a) Spectra of N_2O saturated 40 μM RR-120 solutions (at pH 7) (i) before radiolysis and after steady state radiolysis at (ii) 0.5 kGy, (iii) 1.0 kGy and (iv) 2.0 kGy. (b) ΔOD_λ and (c) transient absorption as a function of λ for N_2O saturated 95 μM RR-120 solution (at pH 7) during pulse radiolysis at pulse dose of 0.01 kGy.*

The reaction between the $^{\bullet}OH$ radical and RR-120 was investigated by pulse radiolysis experiment employing 0.01 kGy/pulse in 95 μM RR-120 solution (at pH 7) saturated with N_2O gas. The change in absorption at any wavelength λ (ΔOD_λ of ΔA) due to the formation of the transient species is shown in *Figure 3.4b*. The absorption decreased significantly in the wavelength range 460-570 nm, while this increased at 650 nm and in the region of 340-390 nm. The increase or decrease in ΔOD_λ depends on the values of the molar extinction coefficients of the transient (ε_t) and parent (ε_p), respectively (*Eq. 2.3*). Therefore, for the same concentration of the transient formed, ΔOD_λ increases when $\varepsilon_t > \varepsilon_p$ and it decreases when $\varepsilon_p > \varepsilon_t$. Thus, the observed spectrum was corrected for parent absorption by *Eq. 2.5* and the corrected absorption spectrum of the species is given in *Figure 3.4c*, which shows a doublet peak at 510-540 nm and a weak band at 660 nm. *[69]* The transient spectrum shows a peak at 660 nm (*Figure 3.4c*), where parent dye (RR-120) has no absorption.

The formation signal of the transient species recorded at 660 nm fitted well to the second order kinetics indicating a bimolecular type of formation of the transient. The pseudo first order rate constant (k_φ) for the reaction of $^{\bullet}OH$ with RR-120 was determined at 660 nm in the presence of different concentrations (50 – 100 μM) of RR-120. The bimolecular rate constant of $^{\bullet}OH$ with RR-120 was calculated as 7.9×10^9 M^{-1} s^{-1} from the slope of the plot of k_φ versus concentrations of RR-120.

The addition of $^{\bullet}OH$ to the aromatic ring of RR-120 forms cyclohexadienyl radicals, which react through disproportionation producing the dye molecule having an extra OH-group (Figure 3.5) *[70]*. The regenerated dye molecules having an extra OH-group should have more extended π-conjugation as compared to the parent dye molecule and thus it justifies the development of absorption at longer wavelength beyond 600 nm (*Figures 3.4a&c*). The addition $^{\bullet}OH$ to triazine ring is a slow reaction

[71]. It should be noted that the decrease in absorbance at 535 nm could not be used to determine G(-Dye) in N_2O saturated solution because of the interference of the products' absorption at the same wavelength.

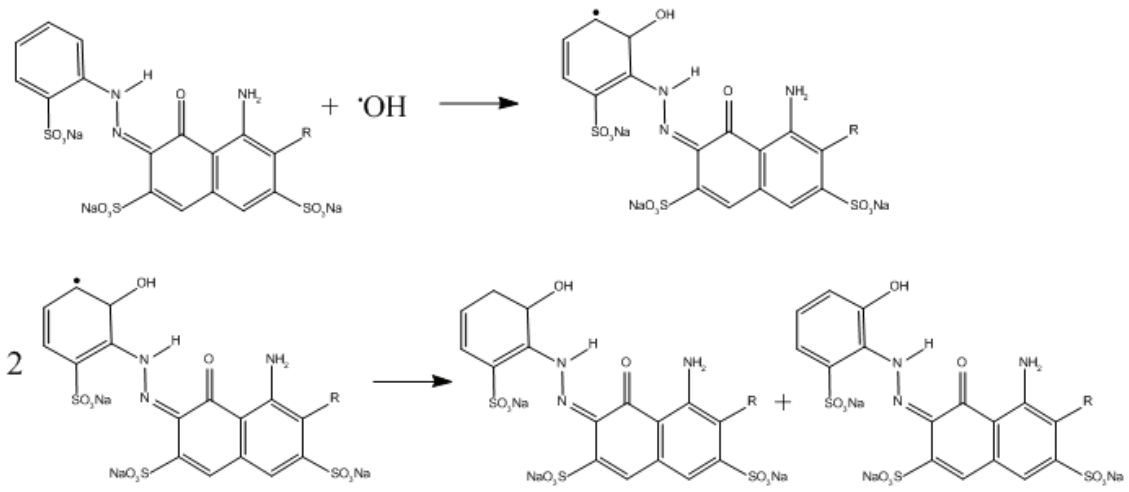

Figure 3.5 *Addition of $^{\bullet}OH$ to the aromatic ring of RR-120 forms cyclohexadienyl radicals, which react through disproportionation producing the dye molecule having an extra OH-group. R represents the residual part of RR-120.*

3.1.2.2. Reaction of RR-120 with Azide Radical ($N_3^{\bullet}$)

Aqueous solution of 40 μM RR-120 solution (at pH 7) containing 20 mM NaN_3 and saturated with N_2O was irradiated for different doses in ^{60}Co gamma chamber having a dose rate of 2.5 kGy h^{-1} (measured using Fricke dosimetry). N_2O converts e^-_{aq} to $^{\bullet}OH$, which in turn converts N_3^- to $N_3^{\bullet}$ as shown in *Eqs. 1.29 & 1.30. Figure 3.6(a)* shows the spectra of N_2O saturated 40 μM RR-120 solutions (at pH 7) containing 20 mM NaN_3 (i) before radiolysis and after steady state radiolysis at (ii) 0.5, (iii) 1.0 and (iv) 2.0 kGy. The intensities of the peaks at 235, 293, 510 and 538 nm decreased with increasing dose. It is attributed to the destruction of the benzene, naphthalene and extended π-conjugation of RR-120 by the oxidising $N_3^{\bullet}$ radical. In contrast to the

reaction of RR-120 with $^{\bullet}OH$, no absorbance was developed at $\lambda > 600$ nm during the radiolysis of RR-120 by $N_3^{\bullet}$ (*Figure 3.6a*).

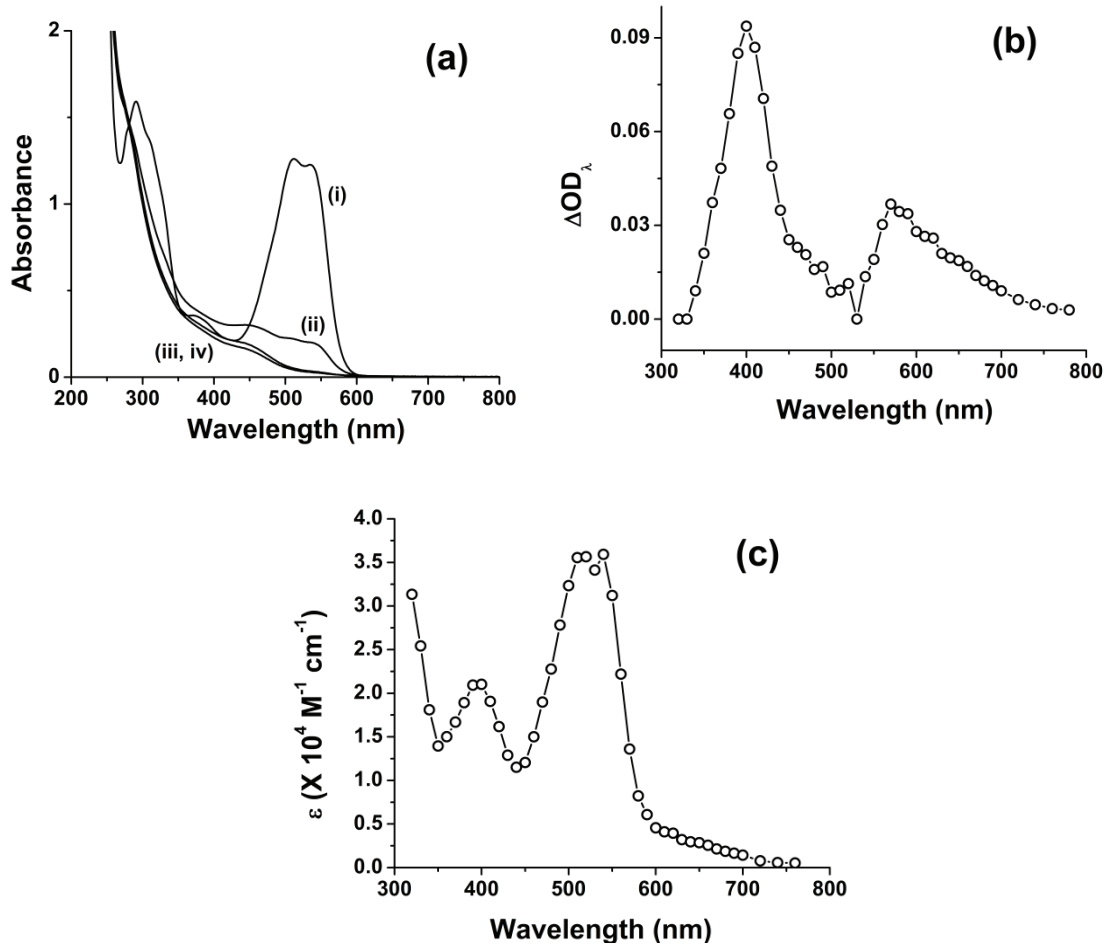

Figure 3.6 *(a) Spectra of N_2O saturated 40 μM RR-120 solutions (at pH 7) containing 20 mM NaN_3 (i) before radiolysis and after steady state radiolysis at (ii) 0.5 kGy, (iii) 1.0 kGy and (iv) 2.0 kGy. (b) ΔOD_λ and (c) transient absorption as a function of λ for N_2O saturated 100 μM RR-120 solution (at pH 7) containing 20 mM NaN_3 during pulse radiolysis at pulse dose of 0.01 kGy.*

The reaction between the $N_3^{\bullet}$ radical and RR-120 was investigated by pulse radiolysis experiment employing 0.01 kGy/pulse in N_2O saturated 100 μM RR-120 solution (at pH 7) containing 20 mM NaN_3. The ΔOD_λ for the reaction between RR-

120 and $N_3^{\bullet}$ increased at 400 nm and 570 nm (*Figure 3.6b)*). The observed spectrum was corrected for parent absorption by *Eq. 2.5* and the corrected absorption spectrum of the species is given in *Figure 3.6c*, which shows a broad peak at 510-540 nm and a band at 395 nm. $N_3^{\bullet}$ radical causes one electron oxidation of RR-120 and the products formed in the reaction of RR-120 with $N_3^{\bullet}$ radical differs from the products formed in the reaction of RR-120 with $^{\bullet}OH$ radical (*Figures 3.4c & 3.6c*). Hence the mechanisms of the reaction of $^{\bullet}OH$ and $N_3^{\bullet}$ radical with RR-120 are different.

It is to be noted that the transient shows little absorption at $\lambda > 600$ nm. Therefore, k_{φ} for the reaction of $N_3^{\bullet}$ with RR-120 was determined from the formation signal of the transient species at 620 nm in the presence of different concentrations (50 – 100 *μM*) of RR-120. The bimolecular rate constant of $N_3^{\bullet}$ with RR-120 was calculated as 1.1×10^9 M^{-1} s^{-1} from the slope of the plot of k_{φ} versus concentrations of RR-120. The decay kinetics of the transient species was studied at 610 nm, where contribution of parent absorption was absent. It was observed that the transient decays through first order reaction with a rate constant of 3.6×10^3 s^{-1}.

3.1.2.3. Reaction of RR-120 with Chlorine Radical ($Cl_2^{\bullet-}$)

Aqueous solution of 40 μM RR-120 solution (at pH 1) containing 50 mM NaCl and saturated with O_2 was irradiated for different doses in ^{60}Co gamma chamber having a dose rate of 2.5 kGy h^{-1} (measured using Fricke dosimetry). $^{\bullet}OH$ converts Cl^- to $Cl_2^{\bullet-}$ by the reactions shown in *Eqs. 1.31-1.33. Figure 3.7(a)* shows the spectra of O_2 saturated 40 μM RR-120 solutions (at pH 1) containing 50 mM NaCl (i) before radiolysis and after steady state radiolysis at (ii) 0.5, (iii) 1.0 and (iv) 2.0 kGy. The intensities of the peaks at 235, 293, 510 and 538 nm decreased with increasing dose. However, a small build up of absorbance with increasing dose was observed at 420 nm.

Therefore, the benzene, naphthalene and extended π-conjugation of RR-120 are destroyed by $Cl_2^{\bullet-}$ during radiolysis resulting into smaller molecular fragments.

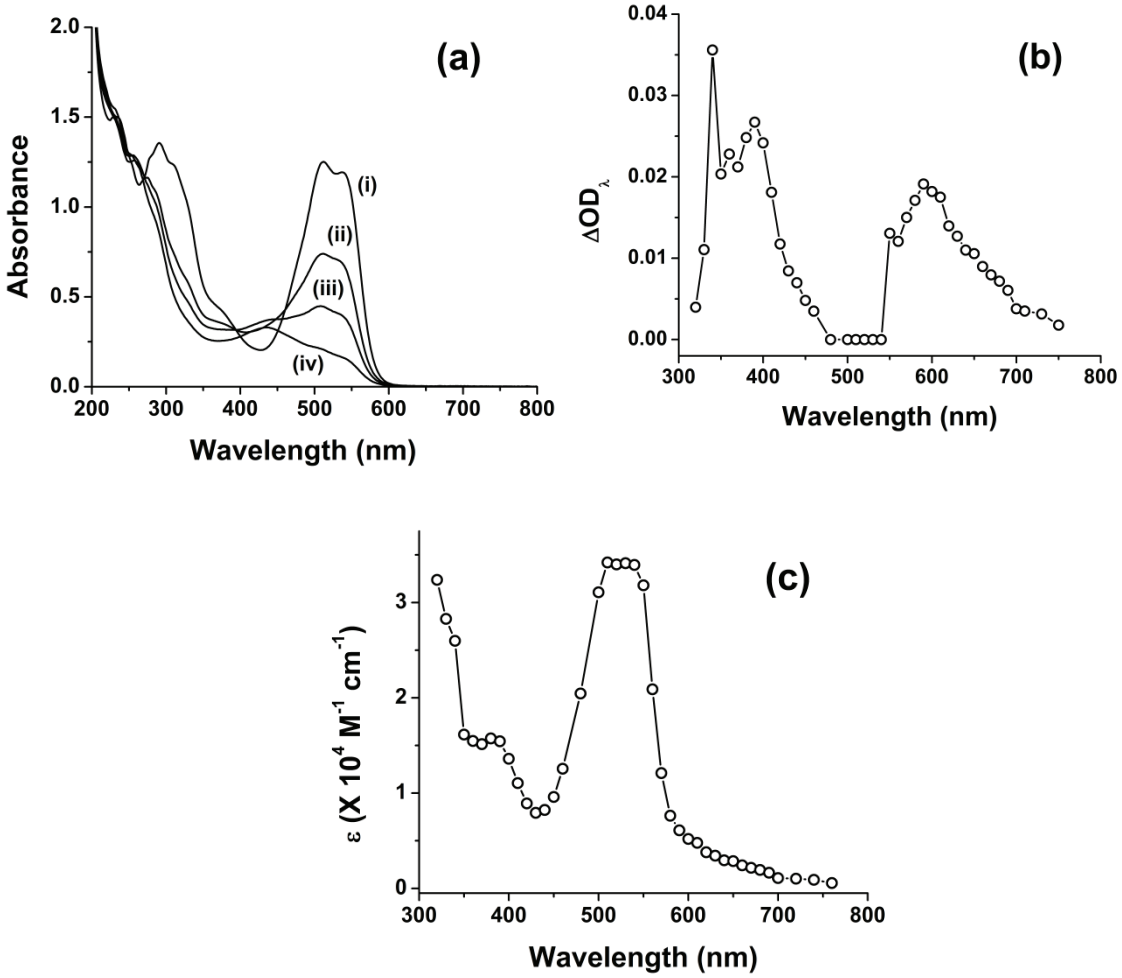

Figure 3.7 *(a) Spectra of O_2 saturated 40 μM RR-120 solutions (at pH 1) containing 50 mM NaCl (i) before radiolysis and after steady state radiolysis at (ii) 0.5 kGy, (iii) 1.0 kGy and (iv) 2.0 kGy. (b) ΔOD_λ and (c) transient absorption as a function of λ for O_2 saturated 100 μM RR-120 solution (at pH 1) containing 50 mM NaCl during pulse radiolysis at pulse dose of 0.01 kGy.*

The reaction between the $Cl_2^{\bullet-}$ radical and RR-120 was investigated by pulse radiolysis experiment employing 0.01 kGy/pulse in O_2 saturated 100 μM RR-120 solution (at pH 1) containing 50 mM NaCl. The ΔOD_λ for the reaction between RR-120

and $Cl_2^{\bullet-}$ increased in the range 340-390 and at 590 nm (*Figure 3.7b*). The observed spectrum was corrected for parent absorption (at pH 1) by *Eq. 2.5* and the corrected absorption spectrum of the species is given in *Figure 3.7c*, which shows a broad peak at 510-540 nm and a band at 385 nm. The transient shows sufficient absorption at $\lambda > 600$ nm. The k_φ for the reaction between $Cl_2^{\bullet-}$ and RR-120 was determined from the formation signal of the transient species at 610 nm in the presence of different concentrations of RR-120. The bimolecular rate constant of the oxidation of RR-120 by $Cl_2^{\bullet-}$ radicals was calculated as 1.0×10^8 M^{-1} s^{-1}. *Figure 3.8* shows the spectra of the transients produced at pH 1 from the reaction of RR-120 with (i) $Cl_2^{\bullet-}$ and (ii) $^{\bullet}OH$. It is evidenced that different transients are produced from these two reactions. $Cl_2^{\bullet-}$ radical causes one electron oxidation of RR-120 producing semi-oxidised species, which subsequently got fragmented. The transient produced by the reaction of RR-120 with $Cl_2^{\bullet-}$ transient decays (monitored at 610 nm) through first order reaction with a rate constant of 4.8×10^3 s^{-1}.

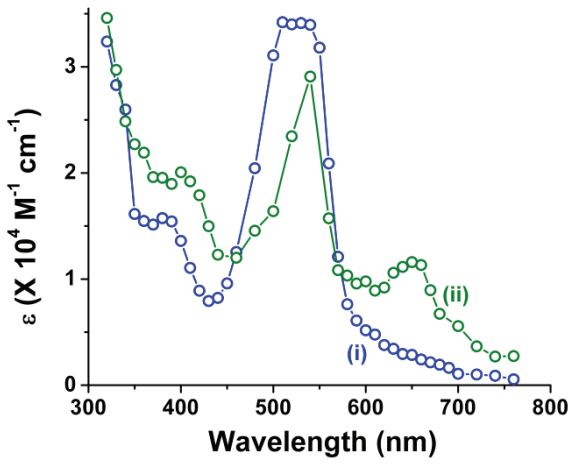

Figure 3.8 *Transient absorption as a function of λ for (i) O_2 saturated 100 μM RR-120 solution (at pH 1) containing 50 mM NaCl and (ii) N_2O saturated 100 μM RR-120 solution (at pH 1). Pulse dose = 0.01 kGy.*

The %decolouration (at 538 nm) of RR-120 for steady state gamma radiolysis in presence of (i) $^{\bullet}OH$ (at pH 7), (ii) $^{\bullet}OH$ (at pH 1), (iii) $N_3^{\bullet}$ (at pH 7) and (iv) $Cl_2^{\bullet-}$ (at pH 1) was calculated by Eq. 3.1.

$$\%\ decolouration = \frac{(A_0 - A_D)}{A_0} \times 100 \qquad (3.1)$$

where, A_0 and A_D are the absorbance measured at 538 nm for unirradiated solution and irradiated solution with dose D, respectively. Figure 3.9 shows the extent of %decolouration of RR-120 during gamma radiolysis in presence of (i) $^{\bullet}OH$ (at pH 7), (ii) $^{\bullet}OH$ (at pH 1), (iii) $N_3^{\bullet}$ (at pH 7) and (iv) $Cl_2^{\bullet-}$ (at pH 1).

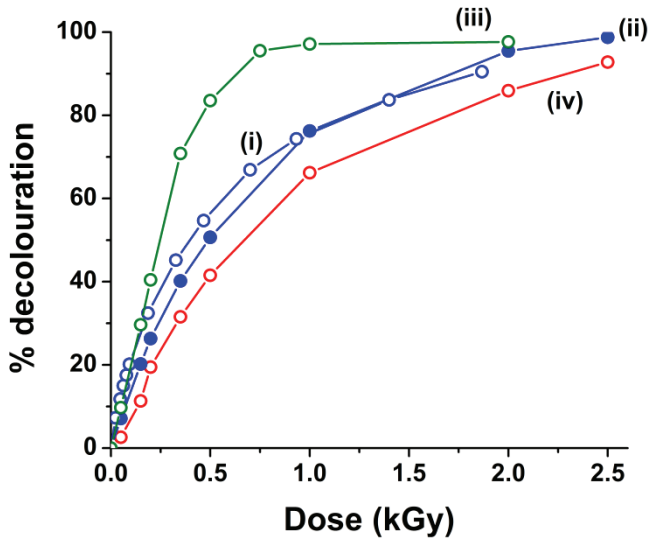

Figure 3.9 *%decolouration of RR-120 during gamma radiolysis in presence of (i) $^{\bullet}OH$ (at pH 7), (ii) $^{\bullet}OH$ (at pH 1), (iii) $N_3^{\bullet}$ (at pH 7) and (iv) $Cl_2^{\bullet-}$ (at pH 1).*

The %decoloration efficiency of $N_3^{\bullet}$ was found to be highest among the studied oxidising radicals. The G value of $^{\bullet}OH$ (0.28 µmol J^{-1}) and $Cl_2^{\bullet-}$ (0.28 µmol J^{-1}) at pH 1 is lower than that of $^{\bullet}OH$ (0.58 µmol J^{-1}) at pH 7. However, no appreciable difference was observed in the %decolouration efficiency of (i) $^{\bullet}OH$ (at pH 7), (ii) $^{\bullet}OH$ (at pH 1) and (iv) $Cl_2^{\bullet-}$ (at pH 1).

3.1.3. Radiolysis of RR-120 by Reducing Radicals

3.1.3.1. Reaction of RR-120 with Hydrated Electron (e_{aq}^-)

Aqueous solution of 40 μM RR-120 solution (at pH 7) containing 0.2 M tert-butanol (^{t}Bu-OH) and saturated with N_2 was irradiated for different doses in ^{60}Co gamma chamber having a dose rate of 3 kGy h^{-1} (measured using Fricke dosimetry). The dissolved oxygen is removed from the solution by purging with N_2 gas and ^{t}Bu-OH converts $^\bullet$OH to lesser reactive radical $^\bullet CH_2(CH_3)_2COH$ by reaction shown Eq. 1.35. Under this reaction condition, the yield of e_{aq}^- becomes 0.28 μmol J^{-1}.

Figure 3.10a shows the spectra of N_2 saturated 40 μM RR-120 solutions (at pH 7) containing 0.2 M ^{t}Bu-OH (i) before radiolysis and after steady state radiolysis at (ii) 0.05, (iii) 0.2 and (iv) 0.33 kGy. The intensities of the peaks at 235 and 293 nm did not appreciably change with increasing dose. Therefore the benzene and naphthalene units of RR-120 did not change during the radiolysis by e_{aq}^-. However, the intensities of the peaks at 510 and 538 nm decreased rapidly with increasing dose. The absorption of the doublet peak decreases with the dose, but any change in the overall shape of the absorption spectra is rarely observed. Further, a build up of absorbance was observed at wavelength ~ 400 nm during the radiolysis by e_{aq}^-. It is attributed to the reductive cleavage of the azo group by e_{aq}^- resulting into destruction of the extended π-conjugation of RR-120 (*Figure 3.11*). The amines produced by the reductive cleavage of azo bond shows n-π^* transition at ~400 nm. The dye solution completely decolourized at 0.33 kGy.

G (-Dye) was estimated by following the decrease in absorbance of N_2 saturated 40 μM RR-120 solutions (at pH 7) containing 0.2 M ^{t}Bu-OH at 535 nm with the increase in dose (inset of Figure 3.10a). G (-Dye) was calculated as 0.14 μmol J^{-1}

using an extinction coefficient value of RR-120 as 35110 M^{-1} cm^{-1}. Therefore, G (-Dye) is just half of the yield of e_{aq}^- (0.28 µmol J^{-1}) up to 0.15 kGy dose. Hence, RR-120 undergoes a two- electron reduction process producing secondary amine having characteristic absorption at ~ 400 nm (*Step 1 of Figure 3.11*). At doses higher than 0.15 kGy, G (-Dye) steadily decreased. This is attributed to the interference of the competitive reduction of the secondary amino product by e_{aq}^- in parallel with the reaction of RR-120 with e_{aq}^- (*Step 2 of Figure 3.11*).

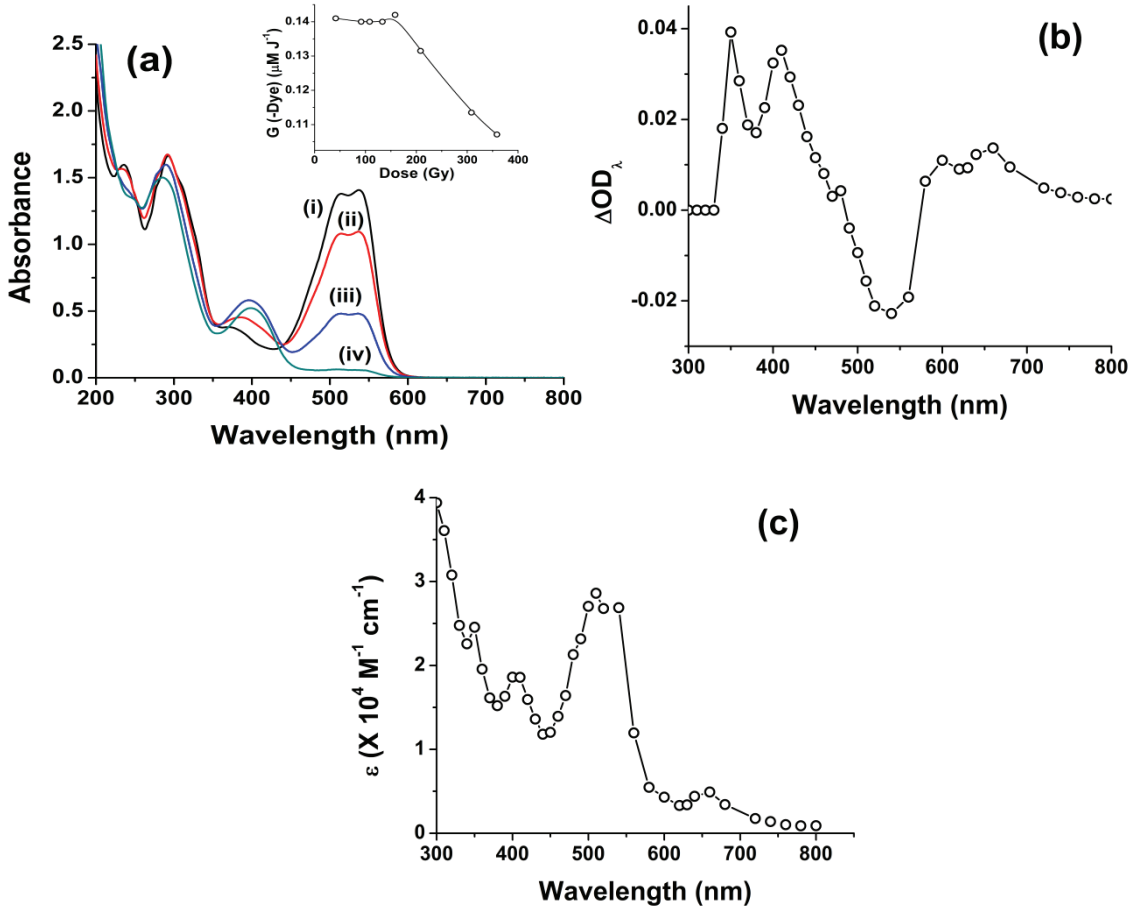

Figure 3.10 *(a) Spectra of N_2 saturated 40 µM RR-120 solutions (at pH 7) containing 0.2 M ^{t}Bu-OH (i) before radiolysis and after steady state radiolysis at (ii) 0.05 kGy, (iii) 0.2 kGy and (iv) 0.33 kGy. (b) ΔOD_λ and (c) transient absorption as a function of λ for N_2 saturated 100 µM RR-120 solution (at pH 7) containing 0.2 M ^{t}Bu-OH during pulse radiolysis at pulse dose of 0.01 kGy.*

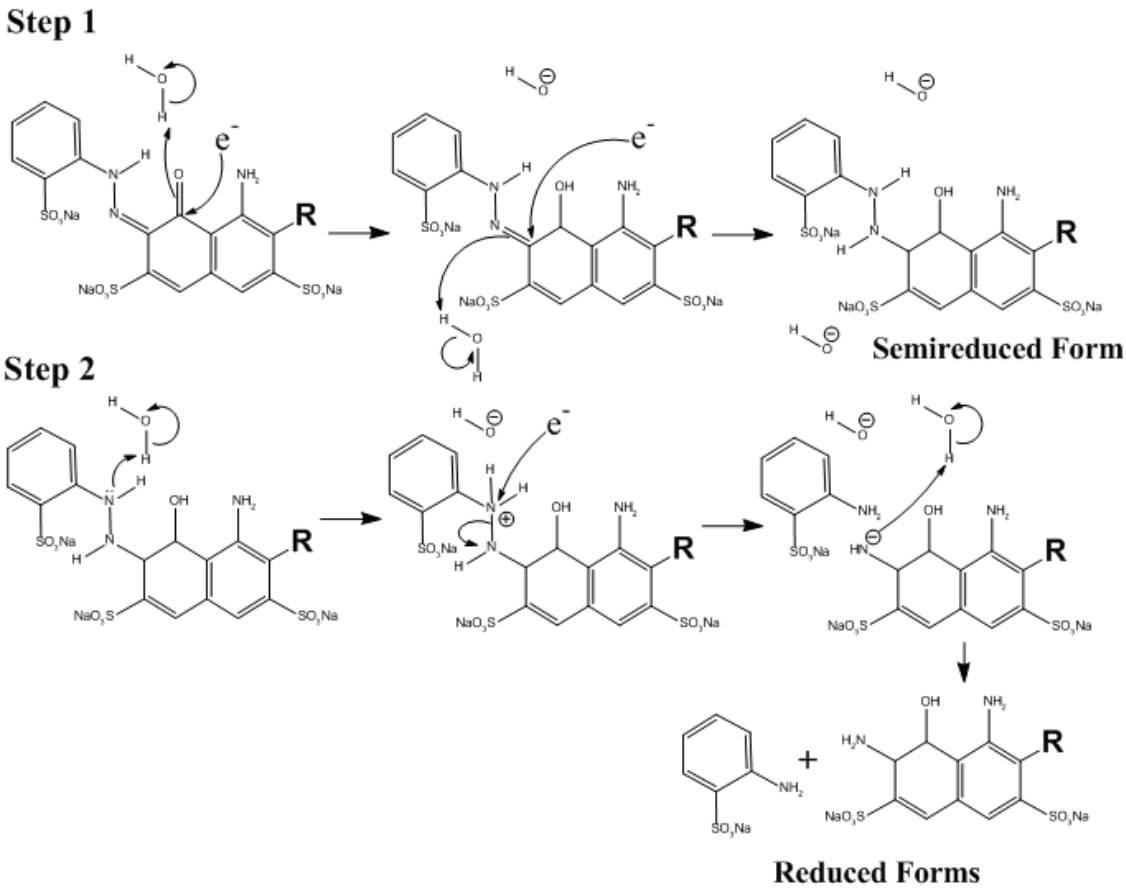

Figure 3.11 *The mechanism of radiolysis of RR-120 by e_{aq}^-. R represents the residual part of RR-120.*

The reaction between the e^-_{aq} and RR-120 was investigated by pulse radiolysis experiment employing 0.01 kGy/pulse in N_2 saturated 100 μM RR-120 solution (at pH 7) containing 0.2 M tert-butanol (^{t}Bu-OH). The absorption at any wavelength λ (ΔOD_λ) changes due to the formation of the transient species is shown in *Figure 3.10b*. The spectrum shows a strong absorption in the region 350-410 nm and weak absorption at 660 nm. The decay kinetics of the transient species was studied at 660 nm, where contribution of parent absorption was absent. The decay trace of the transient fitted well to the second order kinetics indicating a bimolecular type of decay of the transient. No bleaching recovery at 535 and 560 nm was observed indicating the absence of regeneration of the parent dye in the decay step. The k_φ for the reaction between e^-_{aq}

and RR-120 was determined from the decay of e^-_{aq} absorption at 610 nm in the presence of different concentrations of RR-120. The bimolecular rate constant of the reduction of RR-120 by e^-_{aq} radicals was calculated as 1.2×10^{10} M^{-1} s^{-1}.

3.1.3.2. Reaction of RR-120 with Isopropyl Radical ($(CH_3)_2C^{\bullet}OH$)

Aqueous solution of 40 μM RR-120 solution (at pH 7) containing 0.2 M 2-propanol ($(CH_3)_2CHOH$) and saturated with N_2O was irradiated for different doses in ^{60}Co gamma chamber having a dose rate of 2.5 kGy h^{-1} (measured using Fricke dosimetry). N_2O converts e^-_{aq} to $^{\bullet}OH$. Further, $(CH_3)_2CHOH$ converts $^{\bullet}OH$ and $^{\bullet}H$ to $(CH_3)_2C^{\bullet}OH$ by the reactions shown in Eqs. 1.36 & 1.37. *Figure 3.12a* shows the spectra of N_2O saturated 40 μM RR-120 solution (at pH 7) containing 0.2 M $(CH_3)_2CHOH$ (i) before radiolysis and after steady state radiolysis at (ii) 0.05, (iii) 0.2 and (iv) 0.33 kGy. The intensities of the peaks at 510 and 538 nm decreased with increasing dose. It is attributed to the reductive cleavage of the azo group by $(CH_3)_2C^{\bullet}OH$ resulting into destruction of the extended π-conjugation of RR-120. However, the absorbance at 250 and 350 nm increased with increasing dose indicating the production of smaller amino benzene fragments from RR-120 by $(CH_3)_2C^{\bullet}OH$.

The reaction between RR-120 and $(CH_3)_2C^{\bullet}OH$ radicals was studied in N_2O purged aqueous solution of 200 μM RR-120 and 0.65 M $(CH_3)_2CHOH$ at pH 7 (pulse dose = 0.01 kGy). The spectrum shows a strong absorption at 350, 410 nm and weak absorption at 590 nm (*Figure 3.12b*). The corrected absorption spectrum of the transient species formed in the reaction RR-120 with $(CH_3)_2C^{\bullet}OH$ shows strong shows strong absorption in the region of 530–550 nm (Figure 3.12c). The rate constant of the reaction of RR-120 with $(CH_3)_2C^{\bullet}OH$ radicals was observed as 1.8×10^9 M^{-1} s^{-1}.

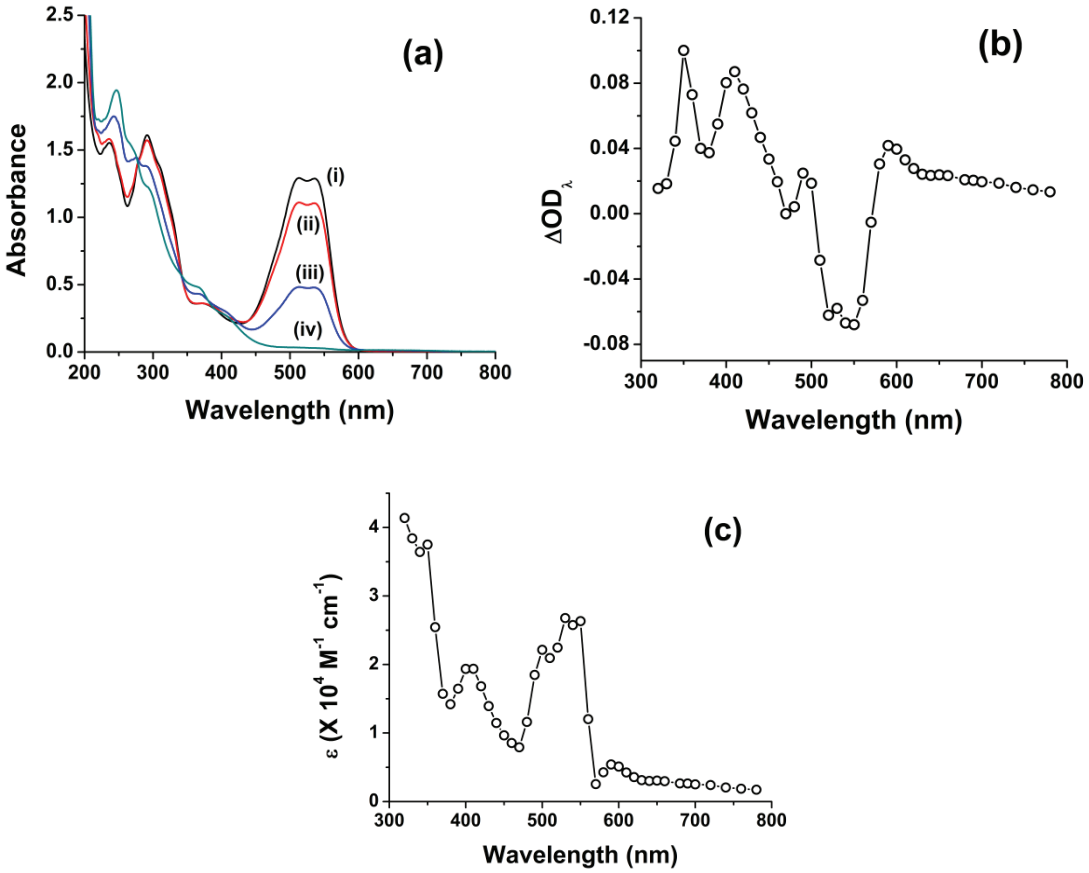

Figure 3.12 *(a) Spectra of N_2O saturated 40 µM RR-120 solution (at pH 7) containing 0.2 M $(CH_3)_2CHOH$ (i) before radiolysis and after steady state radiolysis at (ii) 0.05 kGy, (iii) 0.2 kGy and (iv) 0.33 kGy. (b) ΔOD_λ and (c) transient absorption as a function of λ for N_2O saturated 200 µM RR-120 and 0.65 M $(CH_3)_2CHOH$ at pH 7 during pulse radiolysis at pulse dose of 0.01 kGy.*

Figure 3.13a shows the corrected absorption spectra of the transient species formed in the reaction RR-120 with (i) e^-_{aq} and (ii) $(CH_3)_2C^\bullet OH$. The decay traces of the transient species produced in the reaction of e^-_{aq} and $(CH_3)_2C^\bullet OH$ radicals with RR-120 were studied at 400, 560 and 660 nm. At 400 nm, transient formed between the reaction of RR-120 and $(CH_3)_2C^\bullet OH$ decayed in 1 ms time whereas such decay was absent for the transient produced in the reaction of e^-_{aq} with dye (Figure 3.13b). It indicates that the transients produced from RR-120 by e^-_{aq} and $(CH_3)_2C^\bullet OH$ are

different. The bleaching traces obtained for e^-_{aq} and $(CH_3)_2C^{\bullet}OH$ reactions with RR-120 at 560 nm were totally different (Figure 3.13c). After initial fast bleaching, light level remained steady without any recovery for the reaction of $(CH_3)_2C^{\bullet}OH$ with RR-120. However, after initial fast bleaching, further slow bleaching takes place for the reaction of e^-_{aq} with RR-120.

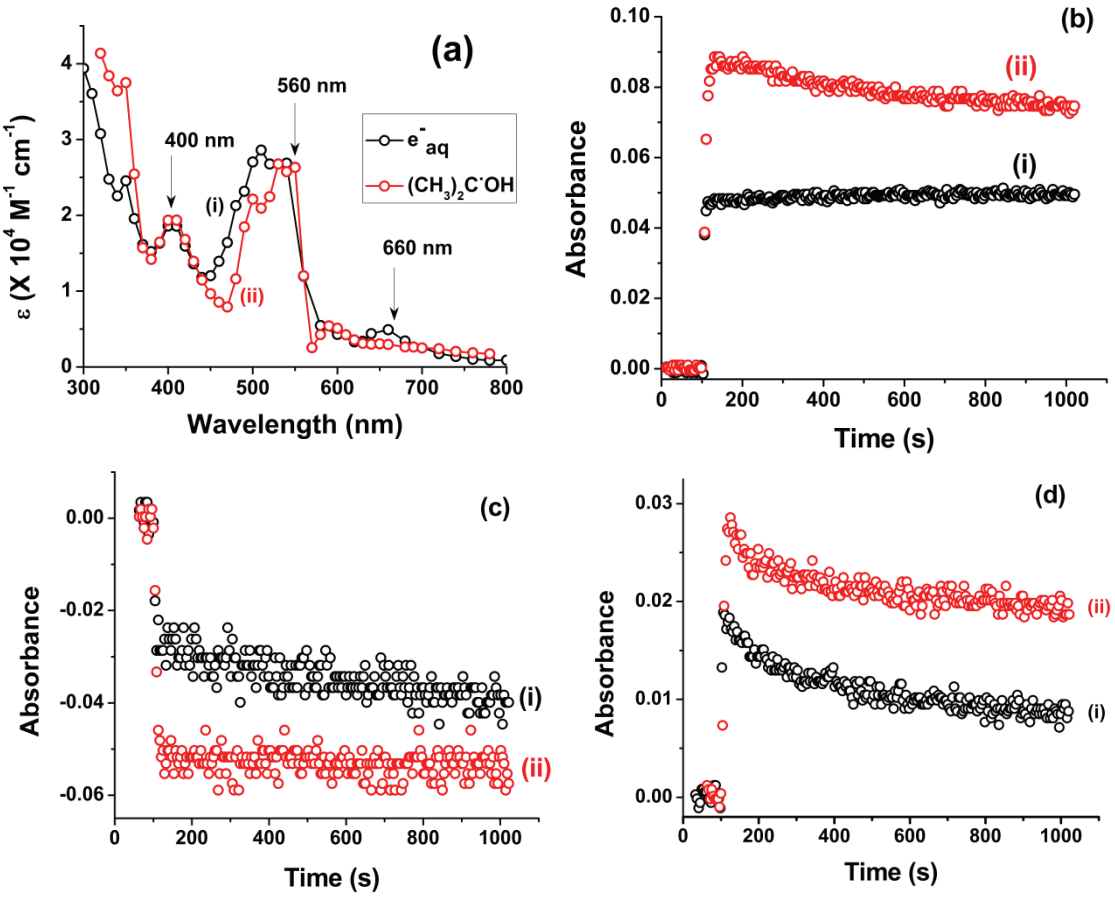

Figure 3.13 *(a) Transient absorption as a function of λ and decay traces recorded at (b) 400 nm, (c) 560 nm and (d) 660 nm for the reaction of RR-120 with (i) e^-_{aq} and (ii) $(CH_3)_2C^{\bullet}OH$.*

The ε values of RR-120 and that of the transients produced in the reaction of RR-120 with e^-_{aq} and $(CH_3)_2C^{\bullet}OH$ at 560 nm are calculated as about 19000 and 12000 M^{-1} cm^{-1}, respectively. In the reaction of RR-120 with e^-_{aq}, initial bleaching at 560 nm

was observed due to higher ε value of parent molecule compared to that of transient species. The semi-reduced species formed in the reaction of e^-_{aq} and RR-120 may react with tert-butanol radicals. No parent dye molecule was regenerated during the decay of the semi-reduced species. Therefore, the bleaching further increased with time. In the reaction of $(CH_3)_2C^{\bullet}OH$ with RR-120, decay of semi-reduced species was accompanied by regeneration of parent molecules. At 660 nm, the transient species formed in the reaction of $(CH_3)_2C^{\bullet}OH$ with RR-120 decayed slowly with a rate constant of 2.1×10^8 M^{-1} s^{-1} as compared to the reaction of e^-_{aq} with RR-120 (2×10^9 M^{-1} s^{-1}). Therefore, both $(CH_3)_2C^{\bullet}OH$ and e^-_{aq} reduce RR-120. In the reaction of $(CH_3)_2C^{\bullet}OH$ with RR-120, the semi-reduced species decayed bi-molecularly regenerating one parent dye molecule; whereas, in the reaction of e^-_{aq} with RR-120, the semi-reduced species reacted with either e^-_{aq} or tert-butanol radical resulting to reduced product which absorbs at 400 nm.

3.1.3.3. Reaction of RR-120 with Formate Radical ($CO_2^{\bullet-}$)

Aqueous solution of 40 μM RR-120 solution (at pH 7) containing 50 mM sodium formate (HCOONa) and saturated with N_2O was irradiated for different doses in ^{60}Co gamma chamber having a dose rate of 2.5 kGy h^{-1} (measured using Fricke dosimetry). The $^{\bullet}OH$ and $^{\bullet}H$ were converted to $CO_2^{\bullet-}$ by the reactions shown in Eq. 1.38. *Figure 3.14a* shows the spectra of N_2O saturated 40 μM RR-120 solution (at pH 7) containing 50 mM HCOONa (i) before radiolysis and after steady state radiolysis at (ii) 0.05, (iii) 0.2 and (iv) 0.33 kGy. The intensities of the peaks at 510 and 538 nm decreased with increasing dose. It is attributed to the reductive cleavage of the azo group by $CO_2^{\bullet-}$ resulting into destruction of the extended π-conjugation of RR-120. The change in absorbance spectra with dose for the reaction of RR-120 with $CO_2^{\bullet-}$ shows similar trends as observed for the reaction of RR-120 with $(CH_3)_2C^{\bullet}OH$.

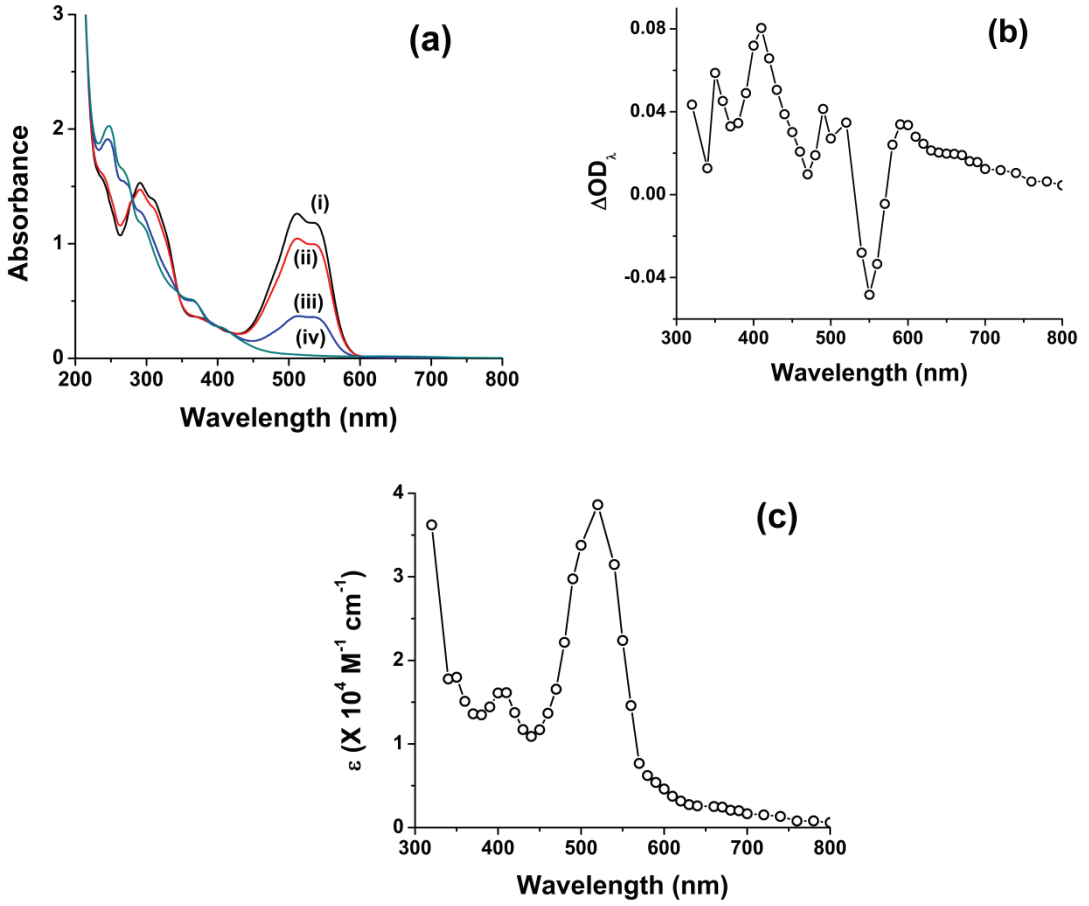

Figure 3.14 *(a) Spectra of N_2O saturated 100 µM RR-120 solution (at pH 7) containing 50 mM HCOONa (i) before radiolysis and after steady state radiolysis at (ii) 0.05 kGy, (iii) 0.2 kGy and (iv) 0.33 kGy. (b) ΔOD_λ and (c) transient absorption as a function of λ for N_2O saturated 100 µM RR-120 and 50 mM $(CH_3)_2CHOH$ at pH 7 during pulse radiolysis at pulse dose of 0.01 kGy.*

The reaction between RR-120 and $CO_2^{\bullet-}$ radicals was studied in N_2O purged aqueous solution of 100 µM RR-120 and 50 mM HCOONa at pH 7 (pulse dose = 0.01 kGy). The spectrum shows strong absorption in the region of 350-400 nm and a small band at 590 nm *(Figure 3.14b*). The corrected absorption spectrum of the transient species formed in the reaction RR-120 with $CO_2^{\bullet-}$ shows strong shows strong peak at 520 nm (*Figure 3.14c*). The k_φ for the reaction between $CO_2^{\bullet-}$ and RR-120 was determined from the formation signal of the transient species at 620 nm in the presence

of different concentrations of RR-120. The bimolecular rate constant of the reduction of RR-120 by $CO_2^{\bullet-}$ was calculated as 1.4×10^8 M^{-1} s^{-1}, which is lesser compared to the bimolecular rate constant of the reaction of RR-120 with $(CH_3)_2C^{\bullet}OH$ and $(CH_3)HC^{\bullet}OH$. The bimolecular rate constant of the reaction of RR-120 with $CO_2^{\bullet-}$ increased to 2.2×10^8 M^{-1} s^{-1} by increasing the ionic strength of the solution by adding 0.2 M Na_2SO_4 in the dye solution. Therefore, small value of the rate constant of the reaction of RR-120 with $CO_2^{\bullet-}$ may be attributed due to the coulombic repulsion between anionic RR-120 (due to the presence of six $-SO_3^-$ groups in the molecular structure of RR-120) and $CO_2^{\bullet-}$. The coulombic repulsion decreased upon increasing the ionic strength of the solution and subsequently the rate constant of the reaction of RR-120 with $CO_2^{\bullet-}$ increased. Figure 3.15 shows the % decolouration (at 538 nm), as shown in Eq. 3.3, as a function of dose during the radiolysis of 40 µM RR-120 by (i) e^-_{aq}, (ii) $(CH_3)_2C^{\bullet}OH$ and (iii) $CO_2^{\bullet-}$. The efficiency of % decolouration of RR-120 by these radicals is almost similar, though radiolytic yields of e^-_{aq} (0.28 µM J^{-1}), $(CH_3)_2C^{\bullet}OH$ (0.58 µM J^{-1}) and $CO_2^{\bullet-}$ (0.58 µM J^{-1}) are different.

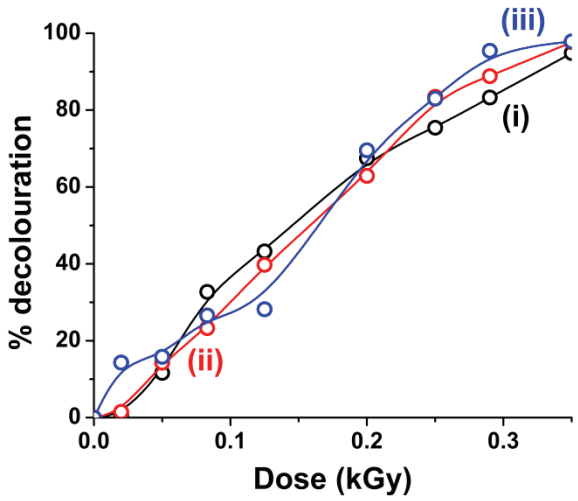

Figure 3.15 *%decolouration of 40 µM RR-120 during gamma radiolysis in presence of (i) e^-_{aq}, (ii) $(CH_3)_2C^{\bullet}OH$ and (iii) $CO_2^{\bullet-}$ at pH 1.*

3.1.4. Radiolysis of Aerated RR-120 Solution

In the Sections 3.1.2 and 3.1.3, it was discussed that the selective oxidising radicals (viz. $^{\bullet}OH$, $N_3^{\bullet}$ and $Cl_2^{\bullet-}$) and reducing radicals (viz. e^-_{aq}, $(CH_3)_2C^{\bullet}OH$ and $CO_2^{\bullet-}$) react with RR-120 through different mechanisms and finally influence the extent of %decolouration of RR-120. However, the in-situ preparation of these radicals during the irradiation process needs some special additives or reaction condition. Therefore, it is of interest to study the radiolysis of aqueous solution of RR-120 (at pH 7) under ambient aerated solution. Aqueous solution of 40 μM RR-120 was irradiated with gamma radiation at pH 7 for different dose. Under this reaction condition, e^-_{aq} and $^{\bullet}H$ are scavenged by the dissolved O_2 producing perhydroxyl radicals ($HO_2^{\bullet}$) and superoxide radical anions ($O_2^{\bullet-}$) as shown by *Eqs. 1.27 & 1.28*. The reduction potential of azo group of RR-120 at pH 7 is about -0.35 V vs. NHE *[72]*; whereas the reduction potentials of $HO_2^{\bullet}$ and $O_2^{\bullet-}$ at pH 7 are -0.037 and -0.33 V vs. NHE. Therefore, reduction of azo group (i.e. decolouration of RR-120) at pH 7 is thermodynamically impossible by $HO_2^{\bullet}$ and $O_2^{\bullet-}$ *[73]*. Hence, under the reaction condition, only $^{\bullet}OH$ becomes responsible for the decolouration of RR-120.

Figure 3.16a shows the spectra of 40 μM RR-120 solution at pH 7 irradiated at (i) 0 kGy, (ii) 0.5 kGy, (iii) 1.0 kGy and (iv) 2.0 kGy doses. The spectra shows similar trends, except lesser pronounced shift in absorbance maxima around 530 nm, as observed for the radiolysis of N_2O saturated RR-120 solution (*Figure 3.4a*). Therefore, the transient produced by the reaction of RR-120 with $^{\bullet}OH$ reacts with the dissolved oxygen forming an adduct, which has slightly different spectral feature. Figure 3.16b shows the spectra of O_2 saturated 40 μM RR-120 solution at pH 7 irradiated at (i) 0, (ii) 0.5, (iii) 1.0 and (iv) 2.0 kGy doses. Under this reaction conditions, the main reacting radicals are $^{\bullet}OH$ and $O_2^{\bullet-}$. It can be seen that the decolouration behaviour of dye in

aerated and O_2 saturated RR-120 solutions are quite similar.

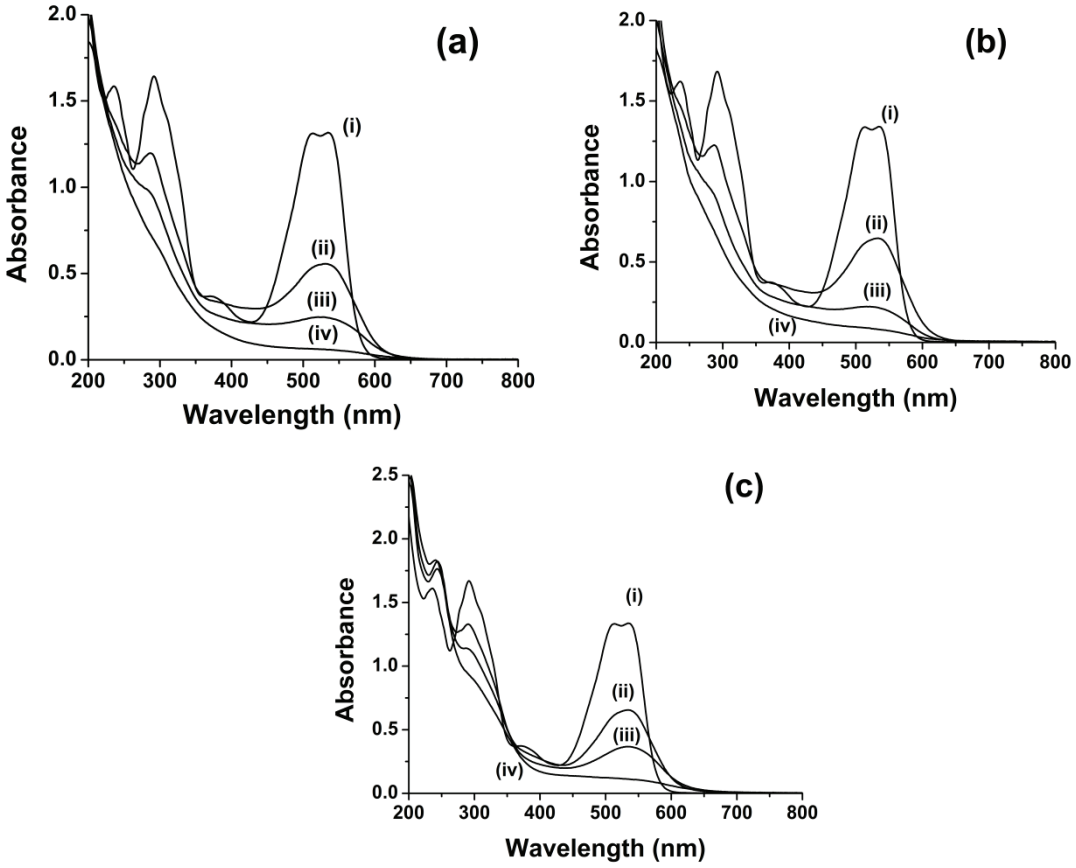

Figure 3.16 *(a) Spectra of (a) aerated (b) O_2 saturated and (c) N_2 saturated 40 µM RR-120 solutions (at pH 7) (i) before radiolysis and after steady state radiolysis at (ii) 0.5 kGy, (iii) 1.0 kGy and (iv) 2.0 kGy.*

Figure 3.16c shows the spectra of N_2 saturated 40 µM RR-120 solution at pH 7 irradiated at (i) 0, (ii) 0.5, (iii) 1.0 and (iv) 2.0 kGy doses. Since, the dissolved O_2 is purged off from the solution by the N_2, thus Figure 3.16c represents the decolouration behaviour of RR-120 by the combined effect of $^{\bullet}OH$ and e^-_{aq}. In contrast to the observation from Figure 3.10a, no building up of absorbance was observed at wavelength ~ 400 nm. One of the possible reasons is that the reduced species formed in this reaction condition may react with the transient species formed by $^{\bullet}OH$ and finally, the resultant products may not have any absorption at 400 nm.

Figure 3.17 shows the % decolouration of 40 µM RR-120 solution at different doses for air, O_2, N_2, ^{t}Bu-OH contained N_2 purged and N_2O saturated systems. The rate of decolouration was found to be very slow for $^{\bullet}OH$ dominating system (in N_2O saturated) as compared to the e^-_{aq} dominating system (^{t}Bu-OH contained N_2 purged). It was also observed from Figure 3.17 that the decolouration efficiency of O_2, N_2, air and N_2O saturated solution was almost same upto 0.5 kGy, whereas at higher doses than 0.5 kGy, decolouration efficiency in O_2 and air saturated systems is distinctly more than that in N_2 and N_2O saturated systems. Since, the products also start absorbing at higher doses, so at this point it is difficult to elucidate the actual mechanism.

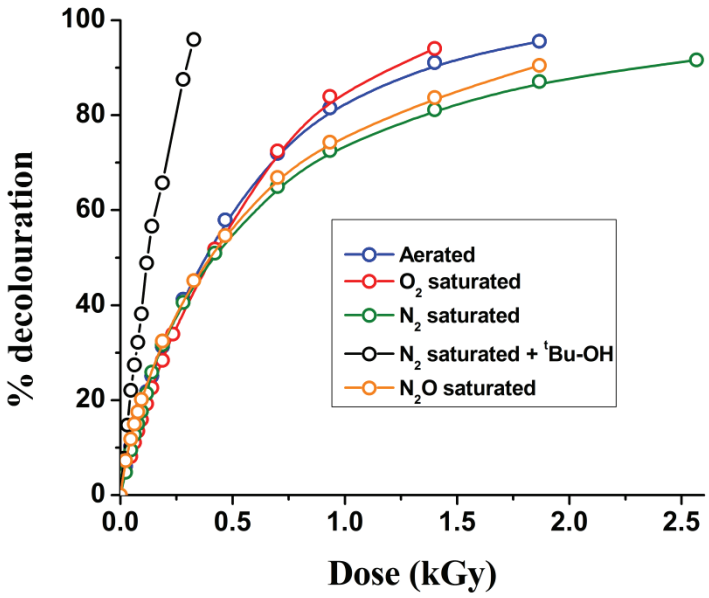

Figure 3.17 *% decolouration of 40 µM RR-120 solution at different doses for air, O_2, N_2, ^{t}Bu-OH contained N_2 purged and N_2O saturated systems.*

The total organic carbon (TOC) represents the amount of organic carbon (irrespective of the oxidation state) present in the aqueous solution of organic compounds. The TOC of 20 µM RR-120 dye (Molecular weight = 1469 g mol^{-1}) solution was calculated as 10.56 mg mL^{-1}. Figure 3.18 shows the % TOC removal of

(a) aerated and (b) oxygen saturated 20 μM RR-120 solutions (at pH 7) during the steady state gamma radiolysis. It should be noted that only ~20% TOC was removed at 2 kGy, though the solution was almost decolourised at that time. On further irradiation, 38% and 48% TOC removal was observed at 3 kGy in aerated and O2 saturated RR-120 solution, respectively. Therefore, the reduction efficiency of %TOC was found to be more for O_2 saturated solution than aerated solution. This suggests that oxygen helps in mineralization of the transient species produced from RR-120 during radiolysis.

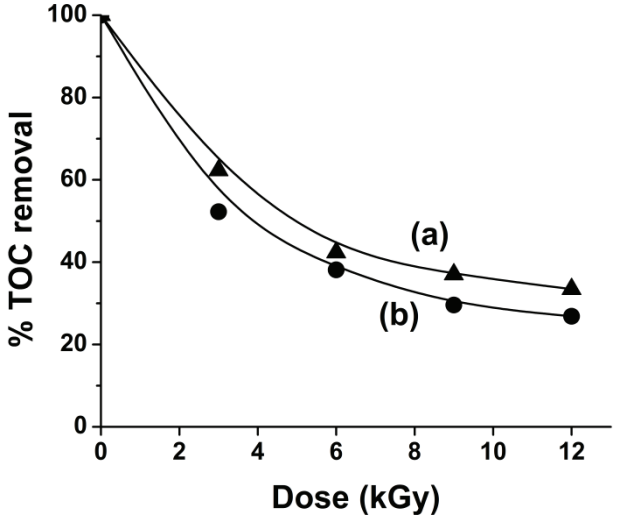

Figure 3.18 *% TOC removal of (a) aerated and (b) oxygen saturated 20 μM RR-120 solutions (at pH 7) during the steady state gamma radiolysis.*

3.1.5. Electron Beam Irradiation of Aerated RR-120 Solution

Figure 3.19a shows the absorbance spectra of 68 μM RR-120 at pH 7 (i) before radiolysis and after electron beam irradiation with 2 MeV beam energy for (ii) 1.5 kGy, (iii) 2.5 kGy, (iv) 5.0 kGy and (v) 10.0 kGy dose. The doublet peaks at 512 nm and 535 nm appreciably decreased with increasing doses. The % decolouration of the dye solution was calculated by monitoring the decrease in the absorbance at 535 nm. About 94% decoloration of 68 μM RR-120 solution was observed at the dose of 1.5 kGy,

whereas the solution was about 99% decolorized at10 kGy (Figure 3.19b(i)). At 1.5 kGy dose, about 94%, 89% and 83% decolouration was observed for (i) 68 µM, (ii) 100 µM and (iii) 130 µM of RR-120 solution at pH 7, respectively (Figure 3.19b). Therefore, the extent of % decolouration of the dye solution was decreased with increasing dye concentration because of the higher extent of radical–radical recombination at concentrated dye solution.

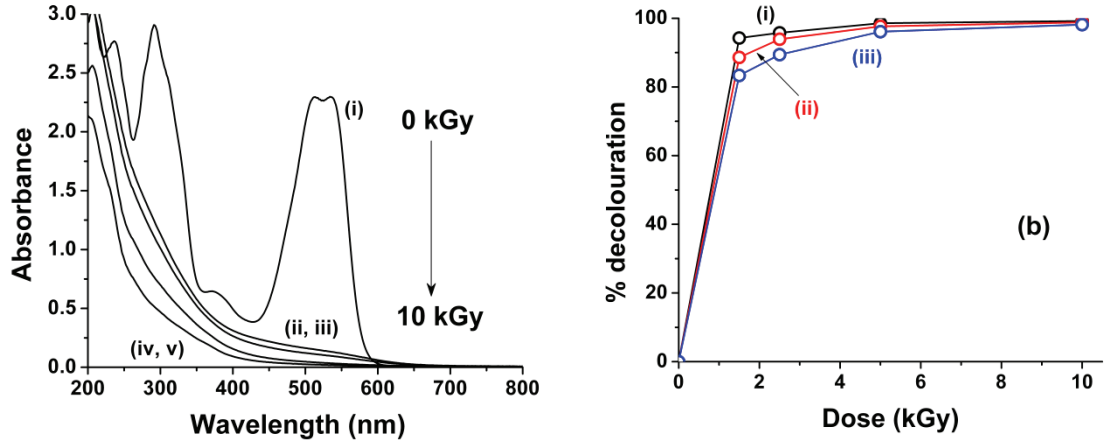

Figure 3.19 *(a) Absorbance spectra of 68 µM RR-120 at pH 7 (i) before radiolysis and after electron beam irradiation with 2 MeV beam energy for (ii) 1.5 kGy, (iii) 2.5 kGy, (iv) 5.0 kGy and (v) 10.0 kGy dose. (b) % decolouration of (i) 68 µM, (ii) 100 µM and (iii) 130 µM of RR-120 solution at pH 7, respectively.*

COD determines the amount of oxygen required to fully oxidize organic compounds into carbon dioxide using a strong oxidizing agent such as $K_2Cr_2O_7$. Thus COD depends on the oxidation states of carbon atoms of the organic constituents present in the solution. However, COD indirectly determines the amount of organic compounds present in the aqueous solution. However, TOC represents the total amount of the organic carbon (irrespective of the oxidation state) present in the solution.

The COD of unirradiated 100 µM and 130 µM RR-120 aqueous solution (at pH

7) of RR-120 was calculated as 83 and 106 mg L^{-1}, respectively. Figure 3.20 shows the %COD removal (hollow circles) of (i) 100 µM and (ii) 130 µM of RR-120 aqueous solution (at pH 7) as a function of the applied electron beam irradiation dose.

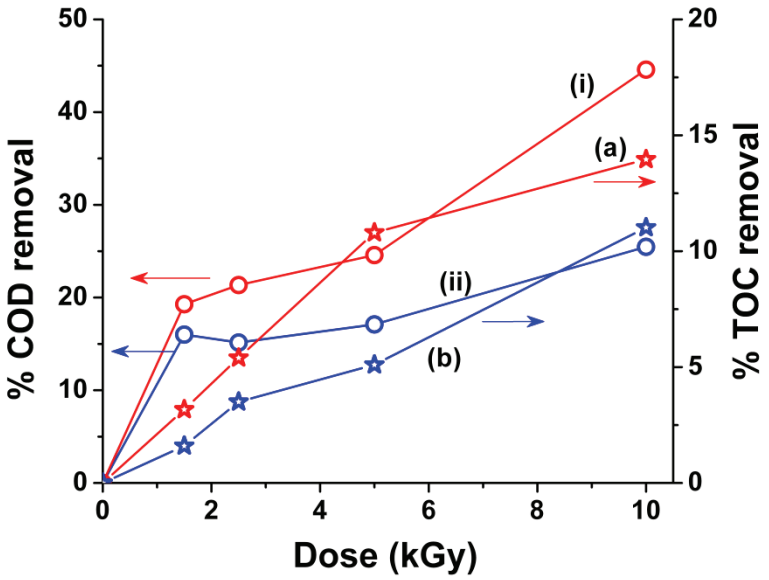

Figure 3.20 *%COD removal (hollow circles) of (i) 100 µM and (ii) 130 µM of RR-120 aqueous solution (at pH 7) as a function of the applied electron beam irradiation dose. %TOC removal (hollow stars) of (a) 100 µM and (b) 130 µM of RR-120 aqueous solution (at pH 7) as a function of the applied electron beam irradiation dose.*

The RR-120 gets fragmented into the smaller organic units along with the destruction of its chromophore group (azo linkage) during the irradiation process. Upon further irradiation, the fragmentation process sometimes leads to complete mineralization of RR-120 to CO_2 and H_2O. Therefore, the %COD removal of the aqueous dye solution increased smoothly with increasing the dose (Figure 3.20(i,ii)). However, a significant decolouration (89%) but minor mineralization (19% COD removal) was observed for irradiating 100 µM dye solution at 1.5 kGy dose. Therefore, it can be understood that the destruction of the chromophoric group of the dye

molecules is only responsible for decolouration, whereas % COD removal solely depends on the complete mineralization of the dye molecules. Lower irradiation dose is sufficient to destroy the chromophoric group of the dye molecules, but it would partially mineralize RR-120 resulting into smaller organic compounds. Hence the rate of % COD removal with respect to the applied dose (Figure 3.20(i)) was relatively lower compared to the rate of % decolouration with respect to the applied dose (Figure 3.19b(ii)).

The % COD removal of RR-120 is also influenced by the concentration of dye. 45% and 25% COD removal was observed for the radiolysis at 10 kGy of (i) 100 μM and (ii) 130 μM dye solutions, respectively.Therefore, the extent of % COD removal of RR-120 decreased with increasing dye concentration because of the higher extent of radical–radical recombination at concentrated dye solution and thus reducing the degradation of dye (Figure 3.20(ii)). Figure 3.20 shows the %TOC removal (hollow stars) of (a) 100 μM and (b) 130 μM of RR-120 aqueous solution (at pH 7) as a function of the applied electron beam irradiation dose. The %TOC removal of the aqueous dye solution also increased with increasing the dose (Figure 3.20(a,b)). The % TOC removal also decreased with increasing the concentration of dye. It is important to mention that %TOC and %COD removal do not overlap as they do not follow the same trend. The higher the amount of intermediate oxidized species (of higher oxidation state) generated after radiolysis, the lesser the number of moles of oxygen (or oxidant like $K_2Cr_2O_7$) was necessary to oxidize the intermediate oxidized products to CO_2. However, some of those oxidized species (of higher oxidation state) could still remain in the irradiated solution resulting into no change in the total organic carbon content of the solution. Therefore, the extent %TOC removal is lesser compared to the %COD removal of RR-120 under identical operational conditions (Figure 3.20).

The pH of the unirradiated 100 μM and 130 μM dye solutions was measured as 6.2. The pH of both the solutions abruptly decreased by 40% during the radiolysis of the dye solutions at 1.5 kGy. However, only 5% decrease in pH was observed upon prolonged irradiation of the dye solutions up to 10 kGy. The initial drastic decrease of pH at lower dose is attributed to the fragmentation of large dye molecule into smaller organic acids such as dicarboxylic acids or acetic acid components and other benzoic compounds *[74]*. Upon prolonged irradiation, these organic acids completely mineralize to carbonic acid. The change of is less susceptible at higher concentration of dye in solution.

3.2. Enhancement of the Biodegradability of RR-120 Solution by Radiolysis

The microbial or enzymatic decolouration and degradation of dye solution is an eco-friendly and cost-competitive process *[75, 76]*. However, the biodegradation of synthetic dye molecules sometimes becomes very slow and even many synthetic dyestuffs are toxic to the micro-organisms *[33, 34]*. The five-day biochemical oxygen demand (BOD_5) is the amount of oxygen consumed by microorganism to degrade organic compounds for a period of five-days. On the other hand, COD represents the amount of oxygen (in terms of equivalent amount of $K_2Cr_2O_7$) required for chemical degradation of organic compounds. The BOD_5/COD ratio is represented as biodegradability index for the aqueous dye solution. Nevertheless, waste waters having BOD_5/COD ratio $\geq$ 0.3-0.4 are generally accepted as biodegradable *[77]*. The BOD_5/COD ratio of the unirradiated 100 μM and 130 μM dye solutions was calculated as 0.20 and 0.17, respectively. Therefore, accordingly to the biodegradability index, these dye solutions are non-biodegradable. However, $\%BOD_5$ increased, but COD decreased for both the solutions with increasing radiation dose because of the formation of more biodegradable intermediates during radiolysis (*Table 3.1*) *[33]*. As a result,

BOD_5/COD ratio increased during the radiolysis process. However, the extent of biodegradability depends on the concentration of dye in solution. The concentrated dye solution exhibited lower biodegradability due to the higher extent of radical–radical recombination. The BOD_5/COD ratio of 100 µM dye solution increased from 0.20 to 0.30 upon irradiating the dye solution at 1.5 kGy and finally at 10 kGy, it became 0.56. It suggested that the non-biodegradable dye solution became biodegradable only upon irradiating with 1.5 kGy dose and its biodegradability enhanced with increasing the applied dose. This results encouraged exploring the combination of radiation and biological treatment for the treatment of textile wastewater.

Table 3.1 *% BOD_5 and BOD_5/COD ratio of 100 µM and 130 µM aqueous RR-120 solutions at pH 7 for different radiation doses.*

Dose (kGy)	Concentration of RR-120			
	100 µM		130 µM	
	Increase of BOD_5 (%)	BOD_5/COD	Increase of BOD_5 (%)	BOD_5/COD
0.0	00.00	0.20	00.00	0.17
1.5	16.18	0.30	15.38	0.23
2.5	35.26	0.34	41.21	0.28
5.0	42.77	0.37	56.60	0.32
10.0	50.23	0.56	60.23	0.37

3.3. Combined Radiation and Microbial Treatment of aqueous RR-120 Solution

Steady state gamma radiolysis of 102 µM aqueous RR-120 solution was carried out at pH 7 for 0.5 and 1.0 kGy by using ^{60}Co gamma radiation with a dose rate of 2.5 kGy h^{-1}. Henceforth, the 102 µM unirradiated and irradiated RR-120 solutions at doses

of 0.5 kGy and 1 kGy will be designated as RR-120-0, RR-120-0.5 and RR-120-1, respectively. The % decolouration of (i) RR-120-0, (ii) RR-120-0.5 and (iii) RR-120-1 after 24 h of microbial treatment was calculated as 27, 56 and 66, respectively (Figure 3.21). The % decolouration of (i) RR-120-0, (ii) RR-120-0.5 and (iii) RR-120-1 increased after 96 h of biological treatment to 87, 94 and 98, respectively. Henceforth, 96 h biologically treated RR-120-0, RR-120-0.5 and RR-120-1 will be designated as RR-120-0-B, RR-120-0.5-B and RR-120-1-B, respectively.

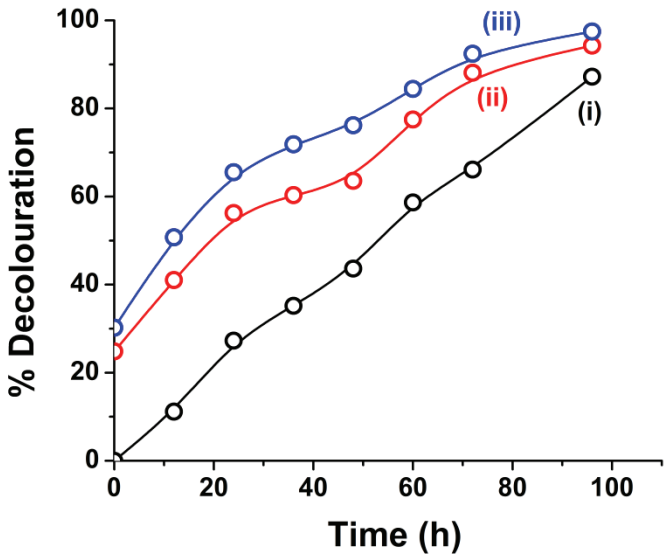

Figure 3.21 *% decolouration of (i) RR-120-0, (ii) RR-120-0.5 and (iii) RR-120-1 during the microbial treatment.*

Figure 3.21 indicates that the introduction of radiation pretreatment increased the efficiency and throughput of the microbial decolouration of RR-120 solution in shorter time scale. It is important to note that the amount of enzymes present in the microbial degradation process is very small compared to the amount of the substrate. At higher substrate concentration, the biodegradation process follows zero-order reaction kinetic with respect to the substrate concentration. Therefore, faster decolouration was evidenced at the initial stage of the microbial treatment. However, the reaction kinetic

switches over at lower substrate concentration from zero-order to pseudo-first order with respect to the substrate concentration. It is well known that the rate of a pseudo-first order reaction becomes more sluggish as the substrate concentration decreases. Therefore, a smaller variation in the extent of % decolouration (87 and 98 %decolouration for RR-120-0-B and RR-120-1-B, respectively) was evidenced at later stage of microbial treatment (Figure 3.21).

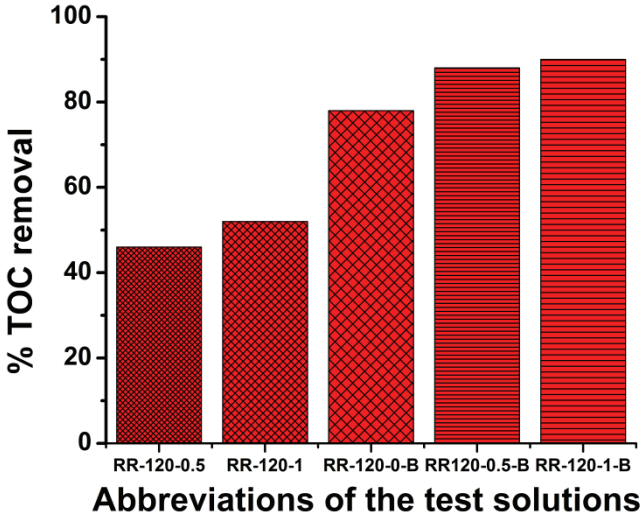

Figure 3.22 *% TOC removal of RR-120-0.5, RR-120-1, RR-120-0-B, RR-120-0.5-B and RR-120-1-B.*

At the initial stage of the radiolysis process, the dye molecules break down into smaller fragments. The % TOC removal of RR-120-0.5, RR-120-1, RR-120-0-B, RR-120-0.5-B and RR-120-1-B was calculated as 46, 52, 78, 88 and 90, respectively (Figure 3.22). The higher TOC removal in case of combined treatment of RR-120 might be due to the acceleration of the fragmentation of the dye molecules upon irradiating with high energy gamma-rays. A similar type of enhancement in the extent of mineralization was also observed in combined electron beam-biological treatment for dyeing wastewater *[78, 79]*.

The treated wastewater from the textile industries is sometime used in the

agricultural fields for irrigation purpose *[80]*. Therefore, the assessment of the toxicity level of the treated textile effluent is one of the important factors for the seed germination and plant growth *[80]*. The toxic effect of the treated dye solution was studied on Indian agricultural seeds viz. Phaseolus mungo at room temperature. Germination (%) as well as the length of plumule and radical were recorded after 7 days. The results were averaged over the 10 seeds under the same experimental condition. The control set was carried out by using distilled water under the same time scale. Although the other experiments were carried out at 102 μM of initial dye concentration, no appreciable differences were observed in seed germination and plant growth between control (distilled water) and treated dye solution at that initial dye concentration. Our preliminary studies showed that Pseudomonas sp. SUK1 was able to effectively decolourise RR-120 up to 410 μM of initial dye concentration and no effective decolouration was observed above that concentration. Therefore, the seed germination and plant growth studies were carried out at 410 μM for both control and treated dye.

The seed germination was reduced to 30% with respect to the control, when the seeds were treated with 410 μM RR-120-0 (Table 3.2). About 80%, 90% and 90% germination was recovered after treating the seeds with 410 μM degraded metabolites of RR-120-0-B, RR-120-0.5-B and RR-120-1-B, respectively. The growth of the plumule and radical length of the seeds was found to be reduced to 48% and 32% in RR-120-0 as compared to the growth of the same in the distilled water, respectively. The growth of the plumule was significantly improved to 89% of the normal growth whereas for radical growth, it was 98% in RR-120-0-B. Again, 92%, 94% and 98%, 99% of the normal plumule and radical growth were recovered for RR-120-0.5-B and RR-120-1-B, respectively. Therefore, biodegradation as well as the combined radiation-

microbial treatment on RR-120 solution showed better reduced toxicity than the unirradiated dye solution.

Table 3.2 *Toxicity studies of 410 µM RR-120-0 and metabolites produced from 410 µM RR-120-0-B, RR-120-0.5-B and RR-120-1-B using Pseudomonas sp. SUK1.*

Parameters studied	Water	RR-120-0	Metabolites produced by *Pseudomonas* sp. SUK1 from		
			RR0-120-0-B	RR-120-0.5-B	RR-120-1-B
Germination (%)	100	30	80	90	90
Plumule (cm)	14.8 ± 0.6	7.2 ± 0.6***	13.2 ± 0.5	13.7 ± 0.4	14.0 ± 0.8*
Radical (cm)	5.0 ± 0.3	1.6 ± 0.3***	4.9 ± 0.2	4.9 ± 0.3	5.0 ± 0.3

*[Values are mean of three experiments ± SEM, significantly different from control (seed germination in distilled water) at *P< 0.05,**P< 0.01and ***P<0.001 by one-way analysis of variance (ANOVA) with Turkey–Kramer comparison test.]*

3.3.1. Investigation on the mechanism of the decolouration and degradation in combined radiation and microbial treatment of aqueous RR-120 Solution

3.3.1.1. FTIR analysis

The broad peak at 3433 cm^{-1} in the FTIR spectrum of RR-120-0 represents N-H stretching frequency of 2º aromatic amine (Figure 3.23a). The peak at 1739 cm^{-1} corresponds to the C=O stretching frequency of the hydrazone tautomer and the peaks at 1017 and 1042 cm^{-1} are attributed to the phenolic -OH groups present in the azo tautomer of the dye. The peaks at 1201 and 1624 cm^{-1} represent the aromatic C-O and –N=N- stretching of the azo group, respectively. The small band at 1443 cm^{-1} is attributed to the in-plane vibrations of the s-triazine ring. The peak at 1114 cm^{-1}

represents the signature of the C-N-C of triazine moiety. The characteristic peak of C-Cl could not be identified due to the overlapping peaks of the other groups in the region of 700-800 cm^{-1}.

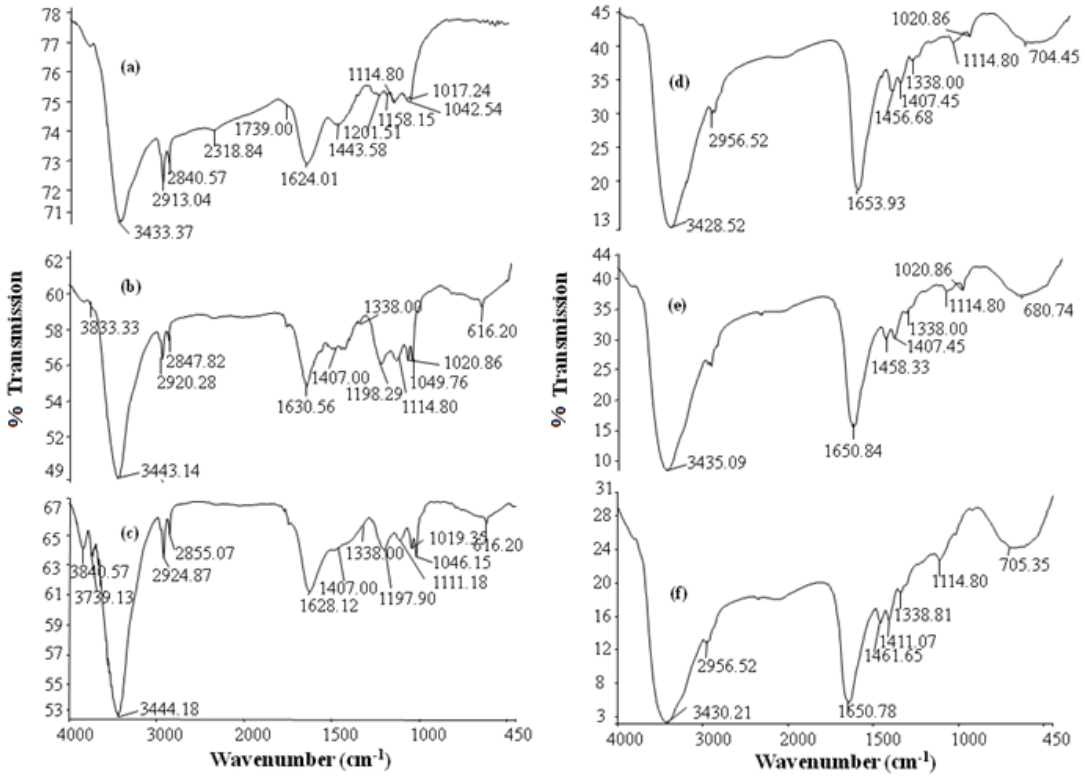

Figure 3.23 *FTIR spectra of (a) RR-120-0, (b) RR-120-0.5, (c) RR-120-1 and (d) RR-120-0-B, (e) RR-120-0.5-B, (f) RR-120-1-B.*

The FTIR spectra of RR-120-0.5 and RR-120-1 revealed the increase in the peak intensities at 1198, 1049, 1020 cm^{-1} (Figure 3.23b) and 1197, 1046, 1019 cm^{-1} (Figure 3.23c), respectively. The increase in the intensities of these peaks might be attributed to the increase in the population of the phenolic -OH groups, which were formed by the addition of $^{\bullet}OH$ radicals to the benzene ring during the irradiation of the dye solution. The peak at 1650 cm^{-1} (primary aromatic amines) which could not be observed in both Figure 3.23b&c might be overlapped with the peak of azo bond (1624 cm^{-1}). The appearance of the peaks at 1650, 1338 and 1407 cm^{-1} (Figure 3.23b&c) might be

ascribed due to the C-N stretching of primary aromatic amines and -CH_2 scissoring bend of cyclohexadiene, respectively, formed upon irradiating RR-120 dye solutions as discussed later in the sub-section 3.3.1.3.. The intensity of the peak at 1114 cm^{-1}, which is the characteristic peak of the C-N-C of triazine moiety, remained constant upon irradiation up to 1 kGy.

The FTIR spectrum of the extracted metabolites from RR-120-0-B solution is shown in Figure 3.23d. The disappearance of the peak at 1624 cm^{-1} is attributed to the destruction of the azo (-N=N-) group. The new pair of peaks at 1650 and 1338 cm^{-1} correspond to the primary aromatic amines (C-N stretching) formed during the biodegradation process. The intensities of the characteristic peaks of the phenolic groups in the range between 1198 and 1020 cm^{-1} significantly changed during the biological treatment process. The relative intensity of the peak at 1650 cm^{-1}, which is the characteristics of the C-N stretching, increased in RR-120-0.5-B and RR-120-1-B (Figure 3.23e&f).

3.3.1.2. HPLC analysis

Two characteristic retention times of RR-120-0 were observed at 1.52 and 1.74 min (Figure 3.24a). However, no remarkable change in the intensity and retention time were observed for RR-120-0.5 and RR-120-1 (Figures 3.24b&c). At this point, we can presume that either (i) the fragmented products were of similar polarities or (ii) the amount of the fragmented products was very low to produce significant response at 280 nm or (iii) the fragmented products did not absorb at the monitoring wavelength or (iv) total concentration of the 280 nm absorbing species remains same. The significant changes in the retention time as well as in the intensity were observed in the extracted metabolites from RR-120-0-B (Figures 3.24d). In this case, the characteristic retention times of the metabolites were observed at 1.22 and 1.34 min compared to 1.52 and 1.74

min for RR-120-0. Biological degradation of RR-120 resulted heavy fragmentation producing metabolites having absorption at 280 nm. HPLC analysis of RR-120-0.5-B showed prominent peaks at retention times 1.25 and 1.36 min (Figures 3.24e), which are quite similar to the extracted metabolites of RR-120-0-B. HPLC analysis of the extracted products from RR-120-1-B showed a remarkable increase in the intensity at retention time 1.22 min (Figures 3.24f), which indicates a better fragmentation of RR-120. The results indicate that degradation products obtained by radiation, biological and combined radiation-microbial treatment of RR-120 may not be similar.

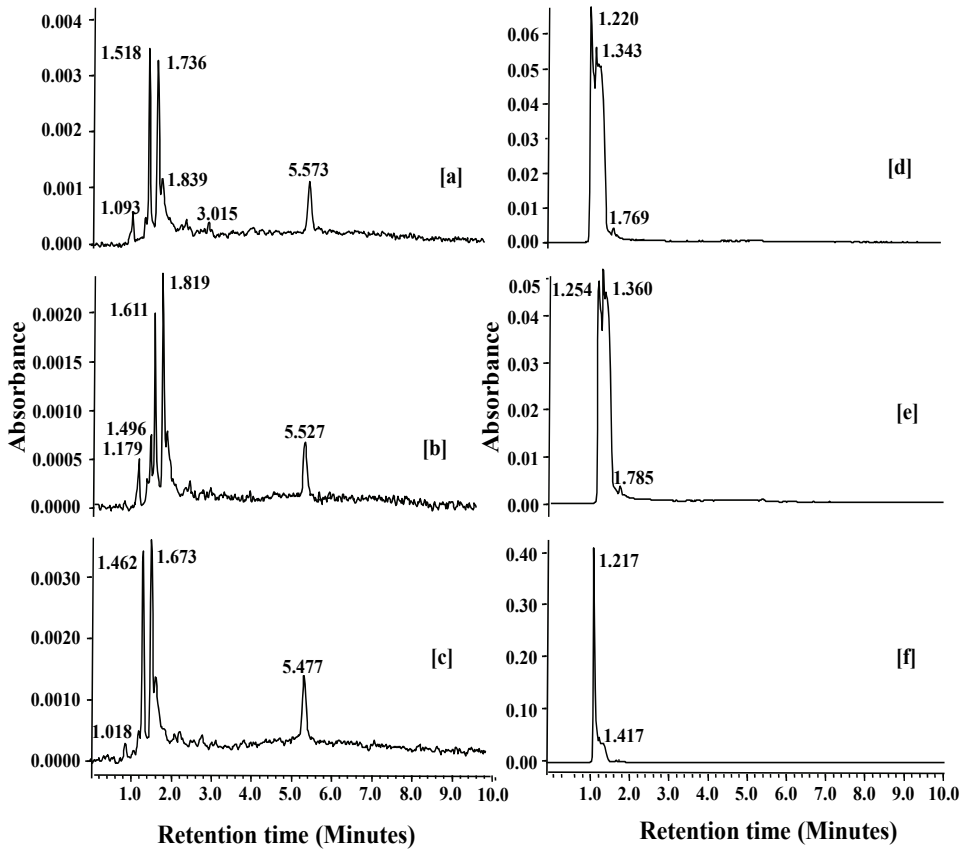

Figure 3.24 *Chromatograms of (a) RR-120-0, (b) RR-120-0.5, (c) RR-120-1 and (d) RR-120-0-B, (e) RR-120-0.5-B, (f) RR-120-1-B.*

3.3.1.3. ESI-MS analysis

A closer inspection of Figure 3.21 revealed that in the combined radiation-microbial process ~25% (for 0.5 kGy) and ~30% (for 1 kGy) decolouration of 102 μM RR-120 solution occurred at the onset of the biological treatment. Therefore, negative ion ESI-MS analysis was performed to study the compositions of (a) RR-120-0, (b) RR-120-0.5 and (c) RR-120-1 solutions just prior to microbial treatment. The peaks corresponding to the parent dye molecule (RR-120; M = 1337) can be assigned for the ion series of $[M - xH]^{x-}$ ions or their sodiated adducts $[M - (x + y)H + yNa]^{x-}$ (where the maximum value of x or (x + y) is equal to the total number of acidic protons) or their in-source fragmented units. The mass spectrum of RR-120-0 exhibited the $[M - 6H + Na]^{5-}$, $[M - 6H + 2Na]^{4-}$ and $[M - 6H + 3Na]^{3-}$ ion peaks from ion series at m/z 271, 344 and 467, respectively and in-source fragmentation peaks at m/z 171 and 337.6 (Figure 3.25a). The most probable structures of the in-source fragments at m/z 171 and 337.6 are shown in Figure 3.26. Five additional peaks at m/z 172, 173, 189, 274.7 and 348 were observed in RR-120-0.5 (Figure 3.25b). The peaks at m/z 172, 173 and 189 correspond to the radiolysis fragments of RR-120 viz. aminobenzosulphonic acid, hydroxybenzosulphonic acid and di-hydroxybenzosulphonic acid, respectively (Figure 3.27). The peaks at m/z 274.7 and 348 correspond to the sodiated adduct of the hydroxylated dye molecule produced during radiolysis from the aromatic electrophilic addition of $^{\bullet}OH$ to benzene or naphthalene ring, e.g. $[M - 6H + O + Na]^{5-}$ and $[M - 6H + O + 2Na]^{4-}$, respectively. The aromatic electrophilic addition of $^{\bullet}OH$ to benzene or naphthalene ring of RR-120 was also supported by the UV–visible spectra of (a) RR-120-0, (b) RR-120-0.5 and (c) RR-120-1 (Figure 3.28), where the increase in the absorbance at longer wavelengths beyond 600 nm due to extra conjugation was evidenced for RR-120-0.5 and RR-120-1.

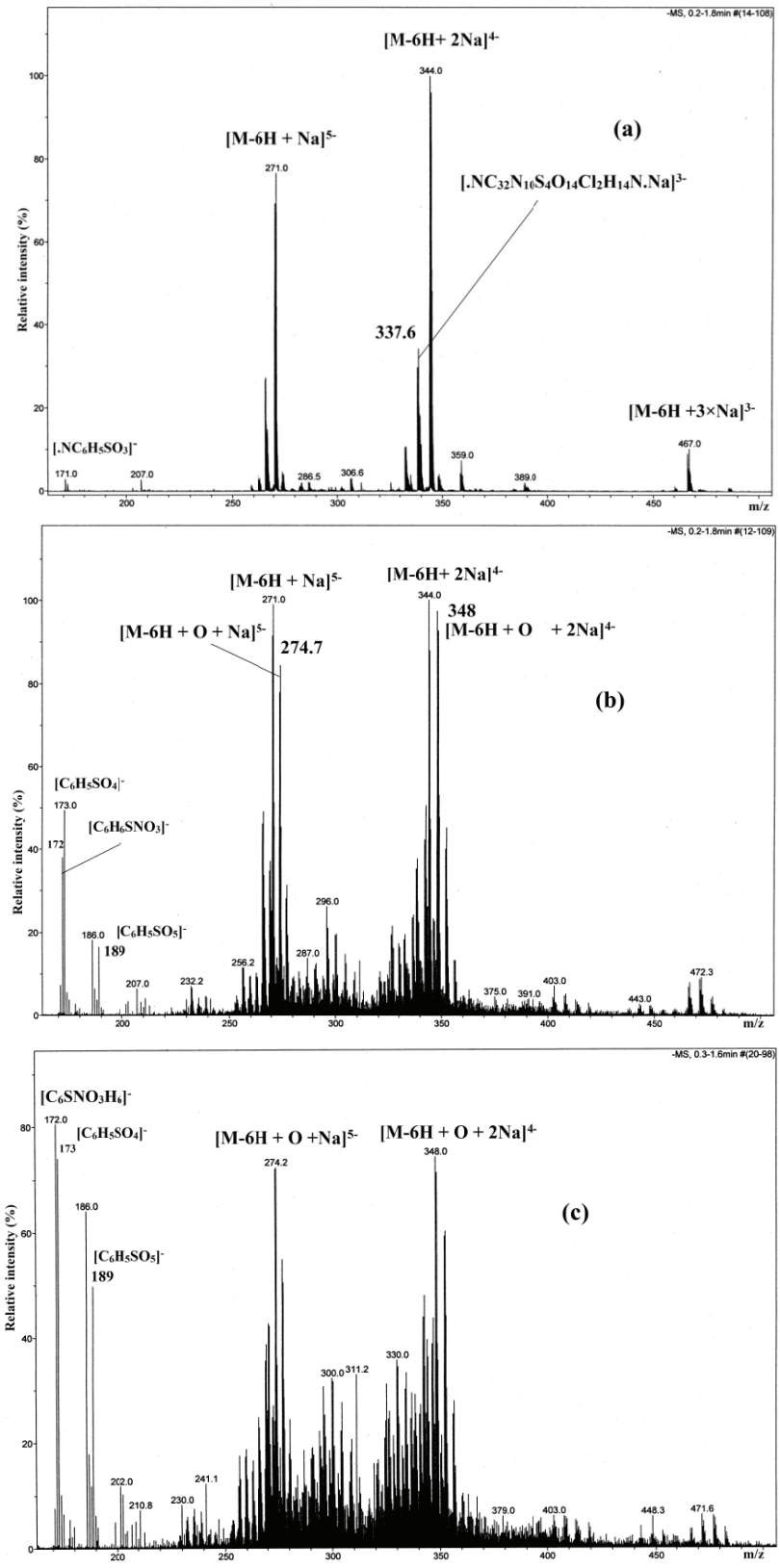

Fjgure 3.25 *Negative ion ESI-MS spectra of (a) RR-120-0, (b) RR-120-0.5 and (c) RR-120-1.*

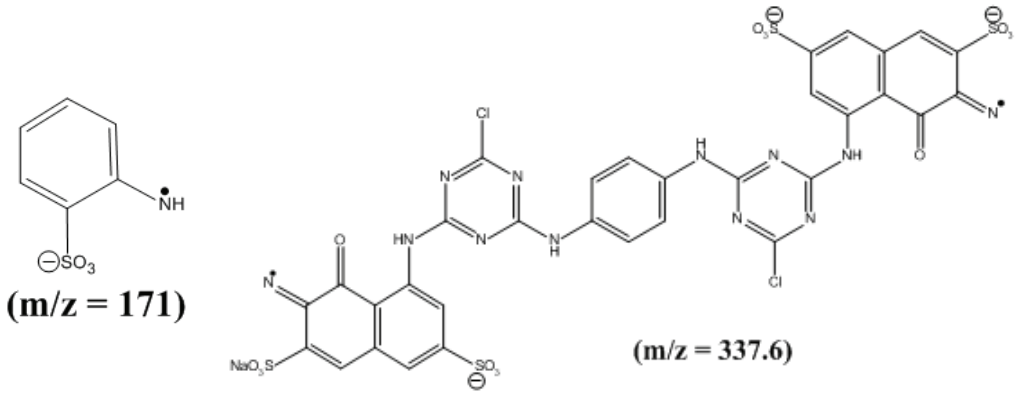

Fjgure 3.26 *In-source fragments of RR-120-0 in negative ion ESI-MS.*

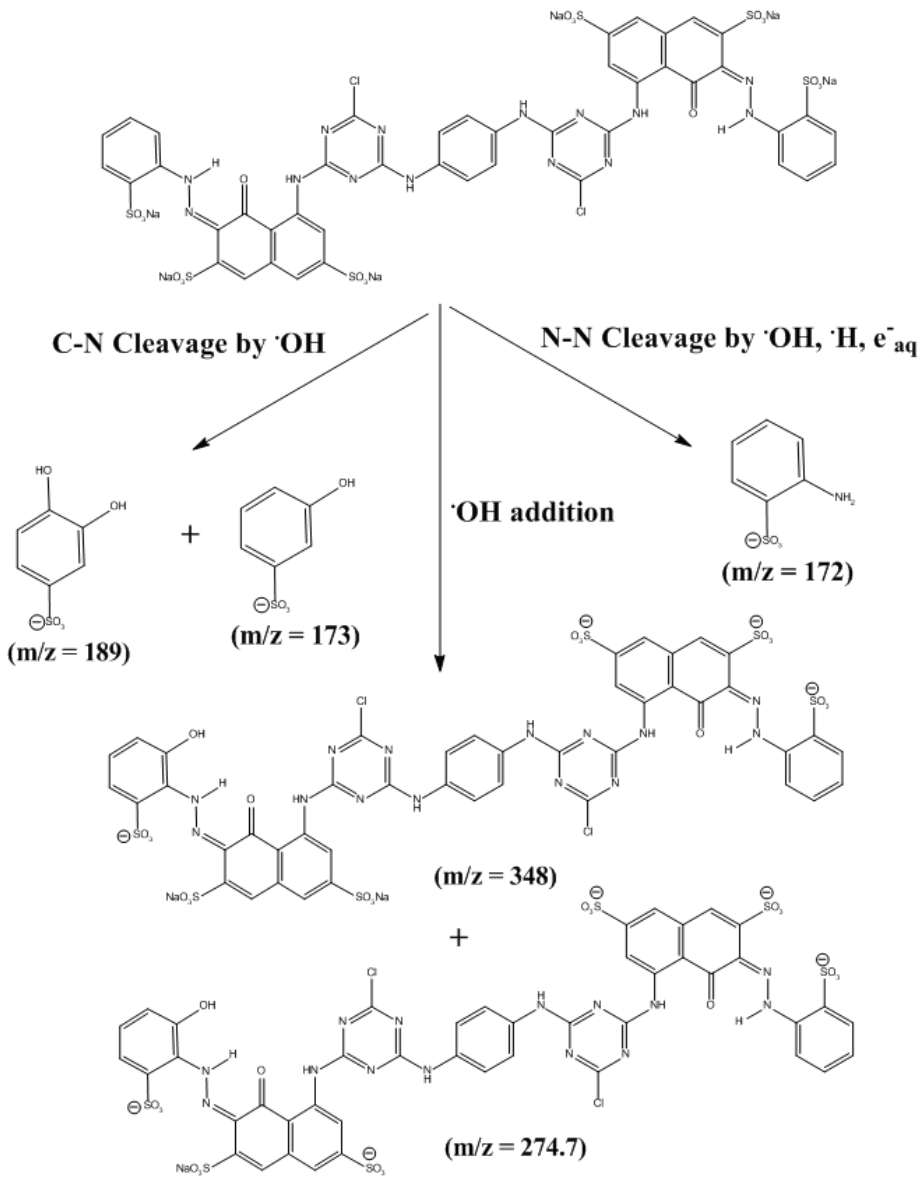

Figure 3.27 *Radiolytic fragments of RR-120 found ESI-MS.*

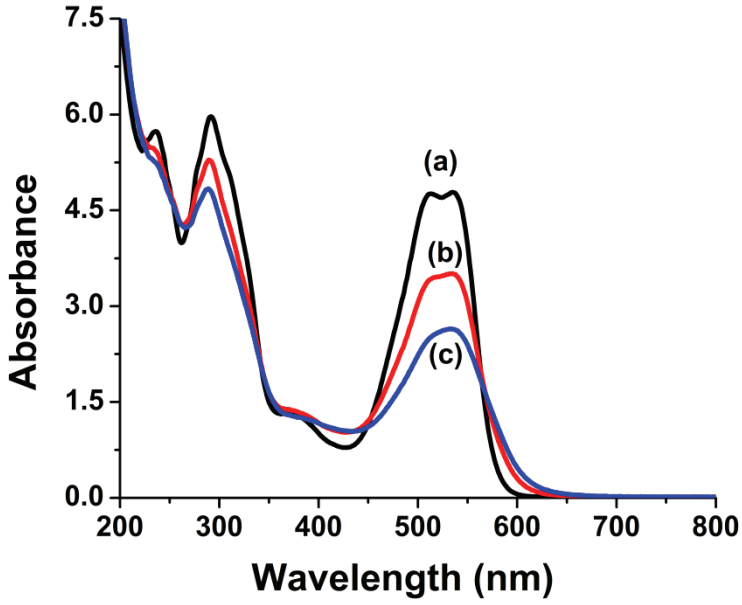

Figure 3.28 *UV–visible spectra of (a) RR-120-0, (b) RR-120-0.5 and (c) RR-120-1.*

The relative intensities of the peaks at m/z 172, 173, 189, 274.7 and 348 increased significantly in the RR-120-1 solution (Figure 3.25c). Therefore, the relative concentration of RR-120 decreased and the relative concentrations of aminobenzosulphonic acid, hydroxybenzosulphonic acid, dihydroxybenzosulphonic acid, $[M - 6H + O + Na]^{5-}$ and $[M - 6H + O + 2Na]^{4-}$ increased significantly for irradiating the dye solution with 1 kGy dose.

3.3.1.4. Enzyme analysis

The major mechanism behind the biodegradation of azo dyes in static condition is the synchronised action of several oxidative and reductive enzymes viz. laccase, tyrosinase, azoreductase and NADH-DCIP reductase leading to the degradation of dye molecules and their fragmented products *[81, 82]*. The activity of laccase, tyrosinase, azoreductase and NADH-DCIP reductase was studied in the cell free extracts obtained from control, RR-120-0-B and RR-120-1-B. The enzyme activity was defined in μM of

ABTS oxidised min^{-1} mL^{-1} (for laccase), units min^{-1} mL^{-1} (for tyrosinase), µM of MR reduced min^{-1} mL^{-1} (for azoreductase), µM of DCIP reduced min^{-1} mL^{-1} (for NADH-DCIP reductase) and the % variation of each enzyme activity in the dye solution with respect to the control. The activity of the tyrosinase was decreased to 58% and increased to 107% in RR-120-0-B and RR-120-1-B, respectively (Table 3.3). The activity of the azoreductase was increased to 122% and 116% in RR-120-0-B and RR-120-1-B, respectively. The laccase activity was increased to 231% and 200% in RR-120-0-B and RR-120-1-B, respectively. The activity of NADH-DCIP reductase increased to 541% and 154% in RR-120-0-B and RR-120-1-B, respectively (Table 3.3).

Table 3.3 *Activities of laccase, tyrosinase, azo reductase and NADH-DCIP reductase in control Pseudomonas sp. SUK1 cells and cells obtained from RR-120-0-B and RR-120-1-B.*

Enzyme	Control	Cells obtained from RR-120-0-B	Cells obtained from RR-120-1-B
Laccase[a]	1.9 ± 0.2	4.4 ± 0.5*	3.8 ± 0.8*
Tyrosinase[b]	0.6 ± 0.1	0.4 ± 0.0*	0.7 ± 0.1*
Azoreductase[c]	1.8 ± 0.1	2.2 ± 0.1*	2.0 ± 0.1*
NADH-DCIP reductase[d]	12.1 ± 0.5	65.2 ± 1.7*	18.6 ± 0.3*

*[Values are mean of three experiments ± standard error of measurement, significantly different from control cells *P<0.001 by one way analysis of variance (ANOVA) with Turkey-Kramer multiple comparison test. [a]µM of ABTS oxidized min^{-1} mL^{-1}; [b]Units min^{-1} mL^{-1}; [c]µM of Methyl Red reduced min^{-1} mL^{-1}; [d]µM of DCIP reduced min^{-1} mL^{-1}.]*

3.3.1.5. GC–MS analysis

GC–MS analysis was carried out with the metabolites formed from RR-120-0-B, RR-120-0.5-B and RR-120-1-B solutions. The metabolites of m/z 154 and 170 obtained from RR-120-0-B are attributed to the biodegraded products viz. N-(4-aminophenyl)-1,3,5-triazine-2,4-diamine and 2-aminobenzenesulfonic acid, respectively (Table 3.4).

Table 3.4 *GC-MS analysis of the metabolites formed from RR-120-0-B, RR-120-0.5-B and RR-120-1-B solutions.*

Identified product name	**Molecular weight of product**	**m/z obtained of product**	**GC-MS Peaks (y-axis in relative % intensity)**
N-(4-aminophenyl)-1,3,5-triazine-2,4-diamine **(III)**	157	154	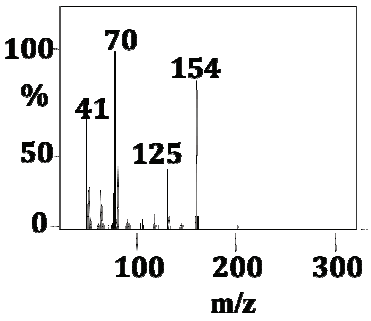
2-aminobenzenesulfonic acid **(I)**	172	170	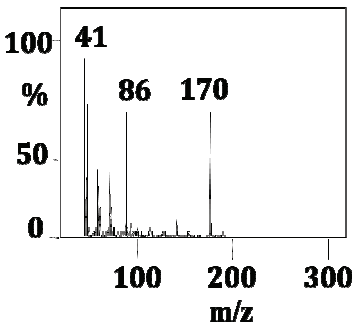
N-(7-amino-8-hydroxy-5,6-dioxo-5,6-dihydronaphthalen-1-yl)-guanidine **(IX)**	246	244	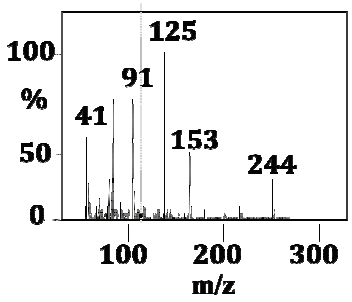

An additional peak at m/z 246 was obtained in RR-120-0.5-B. That new peak at m/z 246 is attributed to the N-(7-amino-8-hydroxy-5,6-dioxo-5,6-dihydronaphthalen-1-yl)-guanidine, which is formed upon the biological treatment of the irradiated solution (Table 3.4). No good quality mass spectrum was observed for RR-120-1-B because of the higher extent of mineralization in that solution.

3.3.2. Discussion on the decolouration and degradation mechanisms of RR-120 for combined radiation-microbial treatment

The probable reason behind the improvement in the process efficiency in case of the combined radiation-microbial treatment in comparison with the general microbial treatment can be proposed by correlating the results obtained from the FTIR, HPLC, ESI-MS, enzyme assay and GC-MS analysis. It is evidenced from Figure 3.27 that primary amines are produced by the reaction of RR-120 with e_{aq}^- and $^\bullet H$ (Figure 3.11). On the other hand, three parallel reactions are possible between RR-120 and $^\bullet OH$ viz. (a) adduct formation to the organic π-system, (b) addition to the chromophoric group and (c) one electron oxidation *[83]*. Therefore, the cleavage of the C-N bond of RR-120 by $^\bullet OH$ forms hydroxybenzosulphonic, di-hydroxybenzosulphonic acid, etc. (Figure 3.27). The cleavage of active azo bond of RR-120 forms aminobenzosulphonic acid (*Figure 3.27*) *[84, 85]*. The aromatic electrophilic substitution of $^\bullet OH$ to phenyl ring and one electron oxidation of RR-120 also competes with the bond cleavage reaction (*Figure 3.27*). Aromatic electrophilic substitution of $^\bullet OH$ to the phenyl produces cyclohexadienyl type of radical, which produces the cyclohexadiene ring (confirmed by $-CH_2$ scissoring bend in FTIR analysis) and regenerates the aromatic ring with an extra OH group via disproportionation reaction.

Laccase is an oxido-reductase, which is able to catalyze the oxidation of various aromatic compounds particularly phenols, aromatic amines, benzenethiols etc. *[86]*.

The activity of laccase is increased in RR- 120-0-B solution compared to control because of the presence of the dye molecule containing phenolic group and its amino metabolites. However, 30% decolouration and 52% TOC removal of RR-120-1 was observed. Therefore, the laccase activity is expected to decrease in the irradiated solution; but almost similar laccase activity was observed in RR-120-1-B (Table 3.3). Therefore, it can be assumed that the radiation induced fragmented products like hydroxybenzosulphonic, di-hydroxybenzosulphonic acid, aminobenzosulphonic acid, etc. helped to recover the laccase activity in RR-120-1-B solution.

Tyrosinase catalyzes the o-hydroxylation of monophenols to yield o-diphenols (cresolase activity) and subsequently oxidation of o-diphenols to o-quinones (catecholase activity) in the presence of oxygen *[87]*. RR-120 and its amino metabolites are supposed to inhibit the first step of the reaction and that is why the activity of tyrosinase is decreased in RR-120-0-B with respect to the control. On the other hand, hydroxybenzosulphonic acid and di-hydroxybenzosulphonic acid were formed in RR-120-1 solution. These irradiated fragments are supposed to be the specific substrates for tyrosinase. Therefore, the activity of tyrosinase increased in RR-120-1-B solution as compared to the RR-120-0-B (Table 3.3).

Azoreductase is the key enzyme for the reductive cleavage of the azo bond (-N=N-) of RR-120 resulting to aromatic amines. The activity of azoreductase was increased in RR-120-0-B solution as compared to the control because of the presence of the azo group in RR-120 *[81]*. The number of azo groups was decreased in the irradiated dye solution and therefore the activity of the azoreductase decreased in RR-120-1-B (*Table 3.3*). From the overall enzyme activity results, it can be concluded that the radiation induced fragmented products of RR-120 showed diverse enzymatic activities; for some enzymes the activity increased whereas it decreased for other

enzymes. The type of enzymes as well as their rate of secretion and activity towards a particular substrate varies with microbial strain to strain *[88]*. Therefore, selection of the microbial strain may be one of the crucial aspects in this type of experiments.

On the basis of various enzyme inductions and GC-MS analysis, the possible biodegradation pathways of unirradiated and irradiated RR-120 dye solution adapted by Pseudomonas sp. SUK1 are illustrated in *Figures 3.29 and 3.30*. Initial cleavage of RR-120 may proceed through the cleavage of azo bond by azoreductase leading to the formation of 2-aminobenzenesulfonic acid [I] of m/z 170 and reactive intermediate [II], which undergoes subsequent oxidative and reductive cleavages by various oxidative and reductive enzymes viz. laccase, tyrosinase and DCIP reductase followed by the dechlorination resulting the formation of N-(4-aminophenyl)-1,3,5-triazine-2,4-diamine[III] of m/z 154.

The azo group of the product [IV] formed in the irradiated dye solution (as observed in Figure 3.27) may be reduced by azoreductase to 2-aminobenzenesulfonic acid [I] of m/z 170 and reactive intermediate [V]. Asymmetric cleavage of the reactive intermediate [V] by laccase and subsequent dechlorination formed another reactive intermediate [VI] and one stable product N-(4-aminophenyl)-1,3,5-triazine-2,4-diamine [III] of m/z 154. Subsequent desulphonation of [VI] led to the formation of [VII], which produces N-(7-amino-8-hydroxy-5,6-dioxo-5,6-dihydronaphthalen-1-yl)-guanidine[IX] having m/z at 246 by further attack of reductase and tyrosinase, subsequently.

The above results demonstrate that irradiating the RR-120 solution with a lower dose (≤ 1 kGy) and then microbial treatment of the irradiated solution with Pseudomonas sp. SUK1 under static condition increased the performance of the degradation and decolouration of RR-120 dye solution. As compared to the chemical

oxidation processes, radiation treatment does not produce any toxic byproducts, needs simple technical operation and most importantly, it is not perturbed by the highly coloured or turbid effluent, which makes it as a potential alternative compared to the other AOPs. This study explores a reliable and promising way to use industrially viable dose and microbial strain for transformation of carcinogenic dyes to non-toxic compounds.

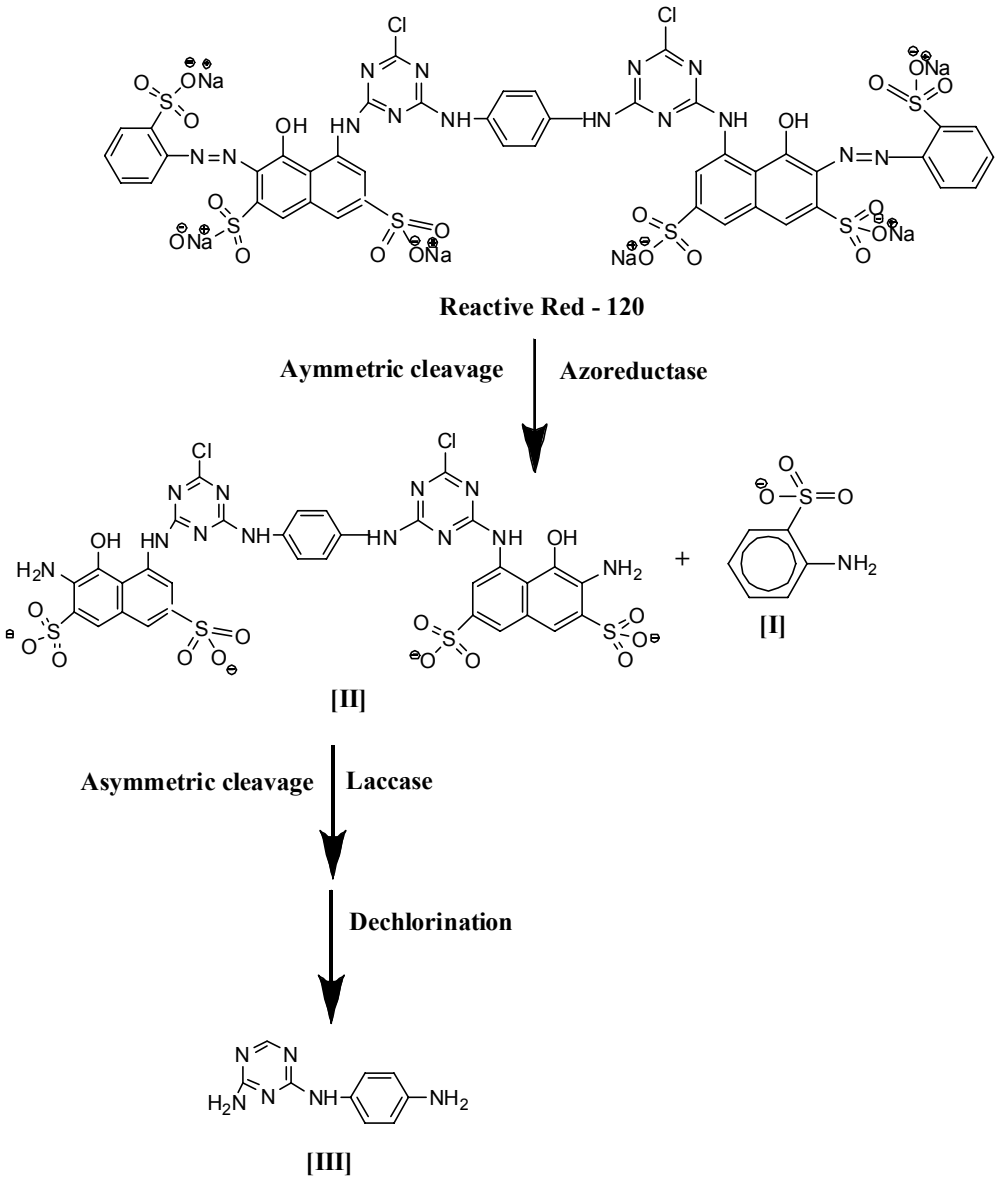

Figure 3.29 *Biodegradation pathways of RR-120-0 dye solution adapted by Pseudomonas sp. SUK1.*

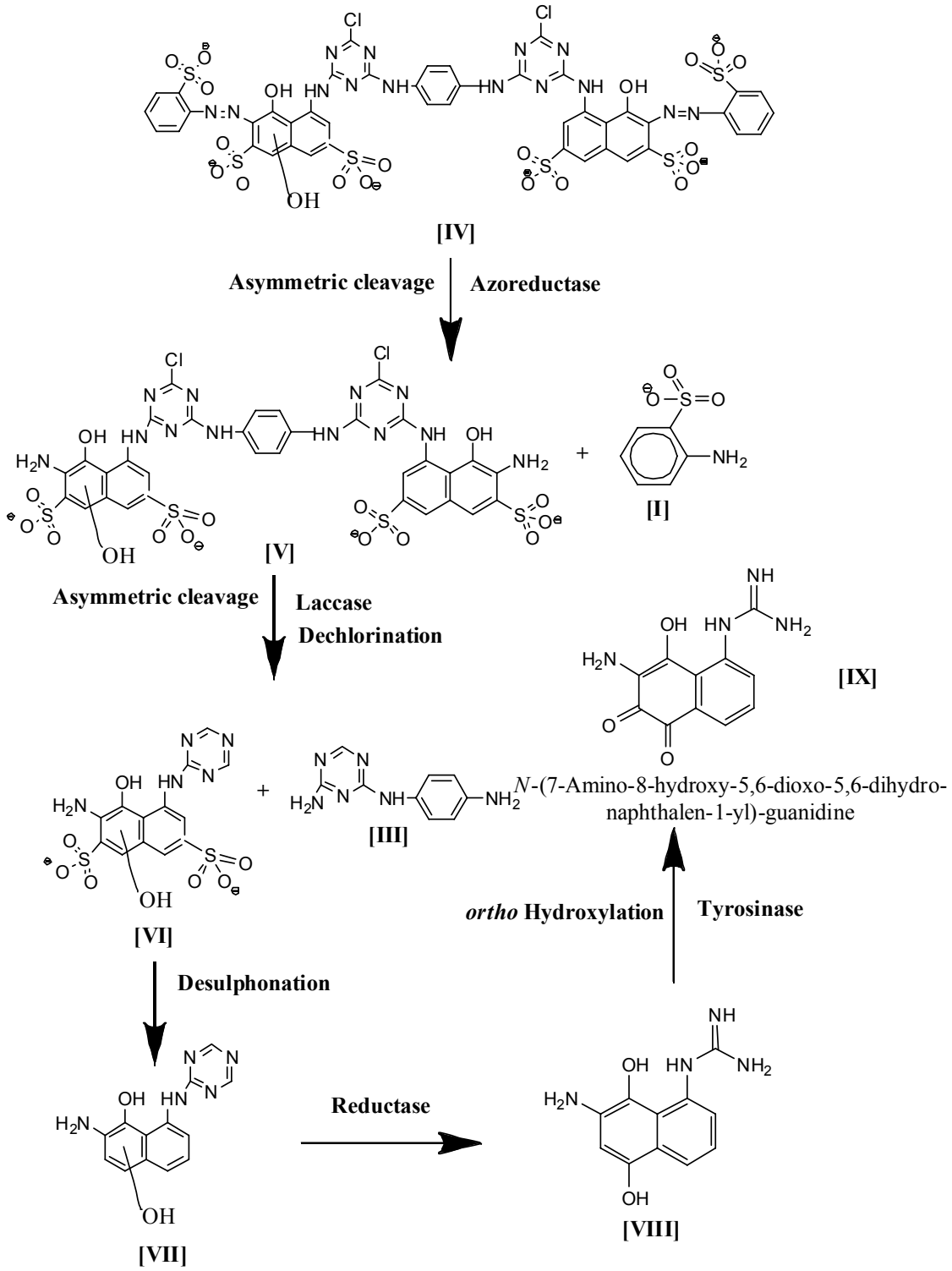

Figure 3.30 *Biodegradation pathways of RR-120-0.5 dye solution adapted by Pseudomonas sp. SUK1.*

3.4. Radiolysis of simulated textile dye waste water (STDWW) containing RR-120

A detailed discussion is presented in the previous sections on the radiolytic mineralization of RR-120. The combined radiation-microbial treatment was also explored to increase the efficiency of the biodegradation process. Further, real textile dye bath contains the auxiliary chemicals (i.e., surfactants, sequestering agent, pH-adjusting acids, inorganic salts etc.) along with the bio-resistant synthetic dye molecules. These auxiliary chemicals of the dye bath contribute to ~83% of the organic load of the effluent *[89, 90]*. The heavy organic load of the textile effluent causes a negative impact to the aquatic lives owing to the decrease in the dissolved oxygen concentration in the water stream *[91]*. The COD of real textile effluents varies in the ranges 2900-3000 ppm, which is well above the permissible discharge limit (COD ≤ 250 ppm) set by the Central Pollution Control Board under the Ministry of Environment and Forest, Government of India.

In this section, the process efficiency of radiolysis is validated on simulated textile dye waste water (STDWW), mimicking the compositions used in dye industries. The process efficiency of the radiolytic mineralization of STDWW was also compared with a couple of AOPs, viz. photocatalysis, ozonolysis. The constituents of the simulated textile dye bath and the role of each constituent in the dyeing process are given in Table 3.5. The hydrolyzed dye effluent was prepared by boiling the constituents with 1 M NaOH at 80-90°C for 3 h under refux *[11]*. The pH, conductivity, COD and dissolved oxygen of STDWW were measured as 10, 28.9 mS, 3128 mg L^{-1}, 3.7 mg L^{-1}, respectively.

Table 3.5 *Composition of STDWW.*

Component	Concentration (mg L^{-1})	Function
C.I. Reactive Red 120	70	Colouring agent
Sodium dodecylbenzenesulfonate (SDBS)	375	Detergent used for washing excess dye
Ethylenediaminetetraacetic acid (EDTA)	150	Removal of unwanted metal ions in the dye bath
Na_2CO_3	4876	Adjustment of the starting pH (8.8–9.3)
NaOH	188	Adjustment of the Final dyeing pH (10.5–11.0)
NaCl	1.5×10^4	Promotes dye binding onto cotton
Acetic acid	As required	For pH (10) adjustment

3.4.1 Decolouration and mineralization of STDWW by photocatalysis and ozonolysis

The $^{\bullet}OH$ radical is produced from the surface of TiO_2 nanoparticles (Degussa (P25), particle size ~ 30 nm) upon irradiating with UV light. The photocatalytic treatment of STDWW was carried out for different time intervals. It took about 500 min of this process to completely decolourise STDWW. However, at the same time, it could mineralise only 21% of the total organic loads of STDWW (Figure 3.31a). The rate of photocatalytic mineralization decreased with time. Therefore, only 25% mineralization was observed at 720 min and no significant change in the extent of mineralization was observed on prolonged irradiation.

The TiO_2 nanoparticles made very stable suspensions with the aqueous solution of the individual components of STDWW. However, it settled down rapidly in STDWW. It can be speculated that the presence of high salts concentration (~1.5×10^4 ppm of NaCl) in the STDWW might be responsible for changing the surface properties

of TiO_2 particles and it finally led to the easy settlement of the catalyst in STDWW. On the other hand, the coulombic repulsion between the negatively charged surface of TiO_2 (pH_{pzc} = 6.0 ± 0.2) and OH^- (at pH 10) also prevents the production of $^{\bullet}OH$ resulting into the poor mineralization of STDWW *[92, 93]*.

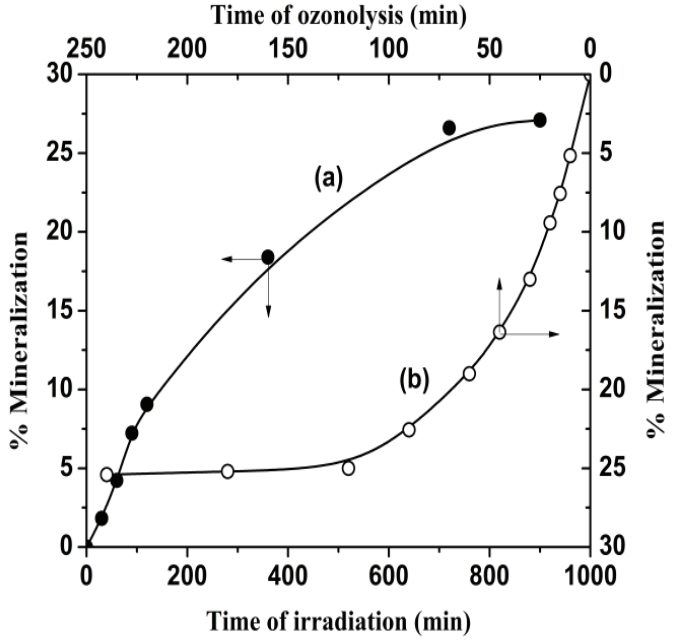

Figure 3.31 *Mineralization of STDWW by (a) photocatalysis (b) ozonolysis.*

Ozone (O_3) produces $^{\bullet}OH$ via decomposition in alkaline pH (pH 10) *[46]*. O_3 is also a strong chemical oxidant and it can directly react with the unsaturations present in the organic molecules *[94]*. Therefore, O_3 and $^{\bullet}OH$ both could react with the components of STDWW. However, the direct reaction of O_3 is selective and slow. The ozonolysis of STDWW was carried out for different time intervals. The complete decolouration and negligible mineralization of STDWW were observed at ~3 min of ozonolysis. About 25% mineralization of STDWW was observed after 120 min and remained almost constant at prolonged ozonolysis (Figure 3.31b). The process efficiency (in terms of the % mineralization of STDWW) of ozonolysis was tried to increase even by adding some additives such as H_2O_2, Al_2O_3, $K_2S_2O_8$ etc., but the

extent of % mineralization did not increase. The continuous flow of oxygen during ozonolysis also did not improve the extent of % mineralization of STDWW.

3.4.2. Decolouration and mineralization of STDWW by gamma radiolysis

The radiolysis of STDWW was carried out for different doses. The complete decolouration and negligible mineralization of STDWW were observed at ~3 kGy dose. The extent of mineralization of STDWW was increased only up to 16% at 50 kGy dose and no further enhancement in the mineralization was observed at higher doses (Figure 3.32a). The above discussed results in conjugation with the results discussed in *Section 1.4.1.* suggested that $^{\bullet}OH$ cannot effectively mineralize the organic load of STDWW. It was observed that the radiolytic mineralization of ibuprofen was enhanced by gamma radiolysis in presence of $K_2S_2O_8$ *[95]*. The e_{aq}^- and $^{\bullet}H$ preferentially reacts with $S_2O_8^{2-}$ during radiolysis resulting into sulphate radical ($SO_4^{\bullet-}$) (Eq. 1.34) *[96]*.

The $SO_4^{\bullet-}$ is itself an oxidising radical. In addition, $^{\bullet}OH$ radical also can react independently with organic compounds *[97]*. The gamma radiolysis of STDWW was carried out for different doses in presence of 40 mM $K_2S_2O_8$. The % mineralization of STDWW was enhanced to 50% at 50 kGy dose, though it remained almost constant at higher doses than 50 kGy (Figure 3.32b). It is important to mention that $K_2S_2O_8$ itself can produce $SO_4^{\bullet-}$ by thermal decomposition at 38-40ºC *[98]*, which is the usual temperature of the solution during gamma radiolysis. Therefore, the extent of mineralization of STDWW in presence of 40 mM $K_2S_2O_8$ was studied at 40ºC in absence of gamma source and no mineralization of STDWW was obtained.

In this context, it is important to mention that the COD of STDWW was 3128 ppm, which was much higher than the COD of pure dye solution (70 ppm) and it indirectly represented the amount of other organic compounds (viz. SDBS, EDTA,

CH_3COOH etc.) present in STDWW. After some preliminary experiments, it was found that the high value of COD was mainly contributed by SDBS, EDTA and CH_3COOH. The concentration of CH_3COOH varies from case to case as it is used to neutralize the pH of the dye bath and thus the radiolysis of pure CH_3COOH component was not investigated. The aqueous solutions of EDTA (150 ppm) and SDBS (375 ppm) were irradiated at pH 10 individually at a dose of 50 kGy both in the absence and presence of $K_2S_2O_8$. About 80% and 95% mineralization of EDTA were observed in the absence and presence of $K_2S_2O_8$. It suggests that EDTA can be mineralized easily by irradiation unlike SDBS. However, more interestingly, about 16% and 62% mineralization of SDBS was observed in the absence and presence of $K_2S_2O_8$. Therefore, the extent of mineralization of SDBS was observed to be enhanced by approximately 4 times in case of gamma radiolysis in the presence of $K_2S_2O_8$.

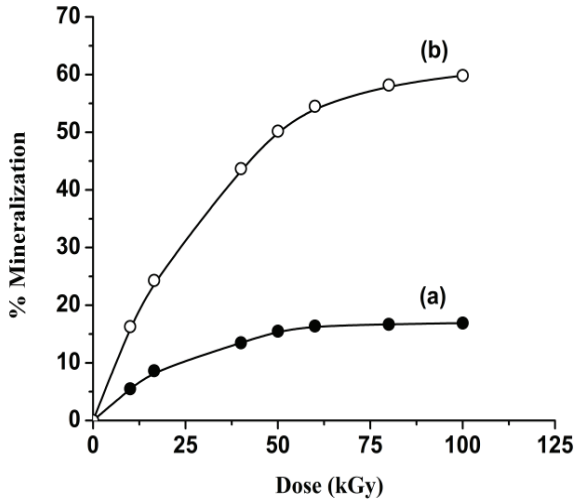

Figure 3.32 *Mineralization of STDWW on gamma radiolysis (a) without and (b) with* $K_2S_2O_8$.

In presence of HCO_3^- and CO_3^{2-}, the extent of mineralization of the organic components present in STDWW was expected to be decreased because of the expected

scavenging of $^{\bullet}OH$ radical by the HCO_3^- and CO_3^{2-} *[99]*. However, no appreciable enhancement in the extent of mineralization was observed during the radiolysis in absence of Na_2CO_3. It indicates that CO_3^{2-} might not have interfered during the radiolysis of STDWW.

3.4.3. Comparison of the process efficiencies of photocatalysis, ozonolysis and gamma radiolysis for the mineralization of STDWW.

The process efficiencies of different AOPs were compared in terms of oxygen-equivalent chemical-oxidation capacity (OCC), which is defined as the kg of O_2 that are equivalent to the quantity of oxidant reagents used in an AOP to treat 1 m^3 of wastewater *[100]*. It gives an index of the chemical efficiency of the oxidants used in an AOP by quantifying the amount of the oxidants (kg O_2) added per m^3 of the wastewater. The OCC of photocatalysis, ozonolysis and gamma radiolysis are calculated by the following Eq. 3.2-3.4:

$$1\ OCC_{Photo}(kg\ O_2\ m^{-3}) = \frac{[I_0(cm^{-2}s^{-1})\times A\ (cm^2)\times t(s)\times 10^6\ (cm^3m^{-3})]}{[6.023\times 10^{26}(kmol^{-1})\times V(cm^3)} \times \frac{1\ kmol\ O_2}{4\ kmol} \times \frac{32\ kg\ O_2}{1\ kmol\ O_2} \qquad (3.2)$$

$$1\ OCC_{Ozo}(kg\ O_2\ m^{-3}) = O_3(kg\ O_3\ m^{-3}) \times \frac{1\ kmol\ O_3}{48\ kg\ O_3} \times \frac{6\ kmol\ e^-}{1\ kmol\ O_3} \times \frac{1\ kmol\ O_2}{4\ kmol\ e^-} \times \frac{32\ kg\ O_2}{1\ kmol\ O_2} \qquad (3.3)$$

$$1\ OCC_{Radio}(kg\ O_2\ m^{-3}) = D\ (J\ kg^{-1}) \times \rho(kg\ m^{-3}) \times G(kmol\ J^{-1}) \times \frac{1\ kmol\ O_2}{4\ kmol} \times \frac{32\ kg\ O_2}{1\ kmol\ O_2} \qquad (3.4)$$

where, D is the dose, ρ is the density of water, $G(SO_4^{\bullet-}) = 3.4\times10^{-10}$ kmol J^{-1} or 3.3/100 eV; $G(^{\bullet}OH) = 2.8\times10^{-10}$ kmol J^{-1} or 2.7/100 eV.

The lowest degree of mineralization (16%) of STDWW was observed for gamma radiolysis (Figure 3.33). Thus the OCCs of different AOPs were compared for only 16% mineralization of STDWW and they were calculated as 4.02, 16.19, 0.13, 0.05 kg equiv. O^2 m^{-3} for photocatalysis, ozonolysis and gamma radiolysis in the absence and presence of $K_2S_2O_8$, respectively. Therefore, for the same extent of mineralization, least amount of oxidant was required for the gamma radiolysis in presence of $K_2S_2O_8$. To the best of our knowledge, this is the first report on the calculation of OCC for photocatalysis and gamma radiolysis.

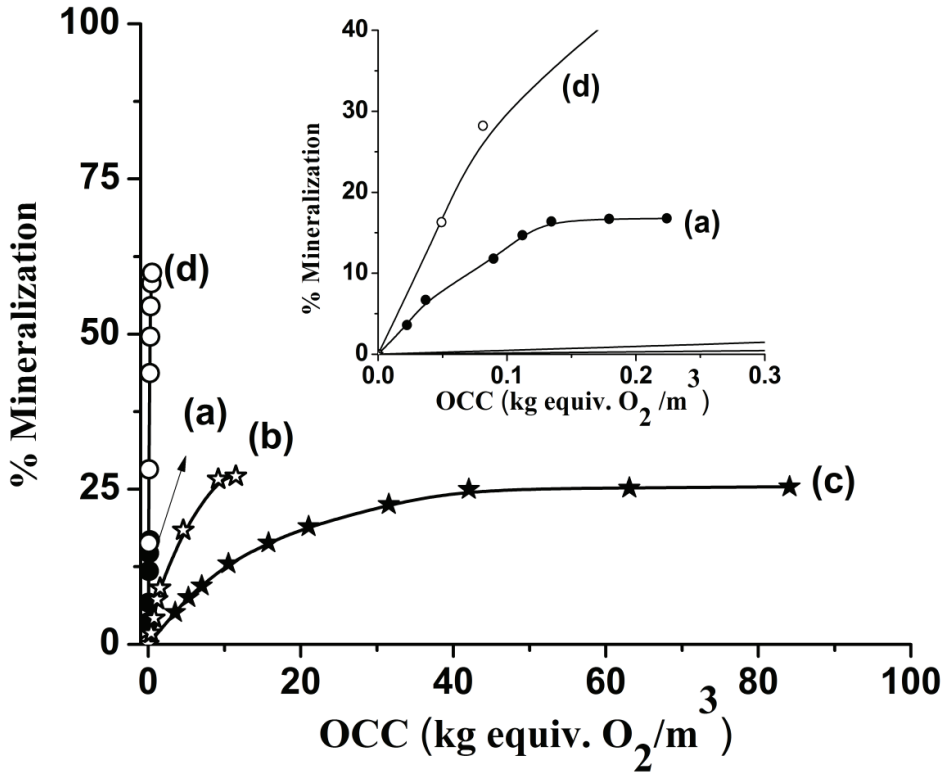

Figure 3.33 *Variation in mineralization extent with OCC of (a) radiolysis (b) photocatalysis (c) ozonolysis (d) radiolysis in presence of $K_2S_2O_8$. Inset: mineralization extent at lower OCC (a) radiolysis (b) photocatalysis (c) ozonolysis (d) radiolysis in presence of $K_2S_2O_8$.*

Gamma radiolysis in the presence of $K_2S_2O_8$ showed better chemical efficiency (i.e. 47% mineralization) of the oxidants at OCC of 0.23 kg equiv. O_2 m^{-3}, which was equivalent to 16% mineralization for the radiation treatment in absence of $K_2S_2O_8$. Moreover, no mineralization was observed at that OCC value for both ozonolysis and photocatalysis. The overall results suggest that the gamma radiolysis in the presence of $K_2S_2O_8$ is the most efficient process for the treatment of STDWW compared to the general gamma radiolysis, photocatalysis and ozonolysis.

3.4.4. Mechanism of mineralization of the components present in STDWW

Mendez-Diaz et al. speculated that the conjugative action of $^{\bullet}OH$ and $SO_4^{\bullet-}$ might be led to the higher extent of mineralisation of SDBS during the photooxidation of SDBS in presence of $K_2S_2O_8$ at pH 7 *[101]*. We want to note that the yield of oxidizing radicals in gamma radiolysis in presence of $K_2S_2O_8$ is 6 [= $G(^{\bullet}OH)$ + $G(SO_4^{\bullet-})$ + $G(^{\bullet}H)$], whereas, that in absence of $K_2S_2O_8$ is 2.7 (= $G(^{\bullet}OH)$). Therefore, about 2.2 times enhancement in the extent of mineralization of SDBS could be expected during gamma radiolysis in the presence of $K_2S_2O_8$ compared to the same in the absence of $K_2S_2O_8$. However, in the Section 3.4.2, we showed that the extent of mineralization of SDBS was enhanced by approximately 4 times due to the presence of $K_2S_2O_8$ during gamma radiolysis.

Therefore, the reactions between SDBS with $^{\bullet}OH$ and $SO_4^{\bullet-}$ were investigated by pulse radiolysis experiments in 0.5 mM aqueous solution of SDBS saturated with (i) N_2O and (ii) N_2, respectively, by employing 14 Gy per pulse at pH 10. The 20 mM $K_2S_2O_8$ and 20 mM t-Bu-OH were added additionally to the solution for the second reaction. Figure 3.34 shows the absorbance per unit G value ($\Delta OD/G$) of the transient species formed by $^{\bullet}OH$ and $SO_4^{\bullet-}$ as a function of wavelength. In Figure 3.34a, a strong absorption at 290 nm, a weak absorption peak at 320 and a weak hump in the range of

325-340 nm was observed for the reaction between SDBS and $^{\bullet}OH$. The peak around at 270-290 nm is attributed to the benzyl type radical and broad peak at 300-350 nm correspond to the formation of OH-adduct with the benzene ring *[95, 102]*. All of the transient species absorbing at 290, 320 and 325-340 nm decayed faster in presence of 4:1 (v/v) mixture of N_2O and O_2 and it suggests that the produced transient species had carbon centered radicals. The decay constant of the transient reacting with O_2 could not be determined because of the interference of the formation signal of the peroxy type radical with the decay signal of the reacting transient.

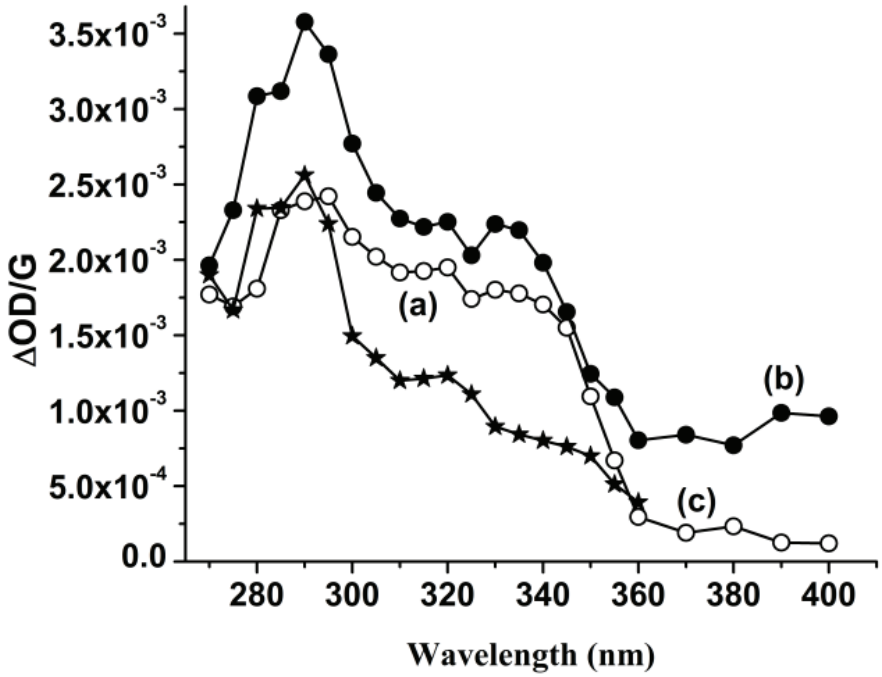

Figure 3.34 *Transient absorption spectra for the reaction of SDBS with (a) $^{\bullet}OH$, (b) $SO_4^{\bullet-}$ and (c) $O^{\bullet-}$ at dose of 14 Gy per pulse.*

Figure 3.35a represents the probable routes of formation of the OH-adducts and benzyl type radicals from the reaction between SDBS and $^{\bullet}OH$. The $^{\bullet}OH$ first conjugates with the benzene ring of SDBS forming the OH-adduct, which reacts with the water molecules leading to the formation of the benzene radical cation. The benzene radical cation is unstable and it forms a benzyl type radical by dissociation of the weak

benzylic C_α-hydrogen *[95, 103]*. Both the intermediates viz. OH-adduct and benzyl type radicals are observed for the reaction of $^\bullet$OH with SDBS. Apart from these above phenomena direct H-atom abstraction may also take place from the alkyl chain of SDBS by $^\bullet$OH *[102]*. The bi-molecular rate constant of the reaction between $^\bullet$OH and SDBS was calculated as 1.8×10^9 M^{-1} s^{-1} (at pH 10), which is similar to the value reported ~10^{10} M^{-1} s^{-1} (at pH 7) by Mendez-Diaz et al. *[101]*.

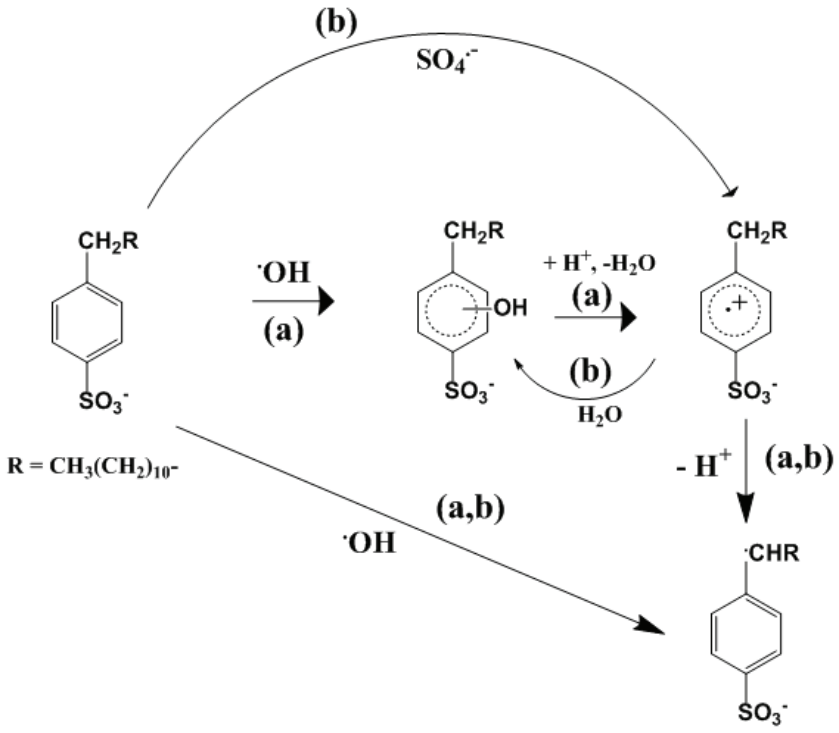

Figure 3.35 *Reactions of SDBS with $^\bullet$OH and $SO_4^{\bullet-}$.*

The similar types of transient absorption peaks were observed at 290, 320 and 330 nm in the reaction of SDBS with $SO_4^{\bullet-}$ (Figure 3.34b). However, the intensity of the peak at 290 nm significantly increased by 1.5 times in case of $SO_4^{\bullet-}$ as compared to the $^\bullet$OH. The $SO_4^{\bullet-}$ is more selective electrophile compared to $^\bullet$OH *[101]*. Figure 3.35b represents the probable routes of reaction between $SO_4^{\bullet-}$ and SDBS. The $SO_4^{\bullet-}$ does not directly add to the aromatic ring. Instead it produces a very short lived (< 0.1 μs) radical cation followed by benzyl type radical and hydroxycyclohexadienyl radical by

the reactions with water molecules *[95, 104]*. $SO_4^{\bullet-}$ can also produce benzyl radical by H-abstraction reaction from the alkyl chain of the SDBS *[101, 102, 105]*. The bi-molecular rate constants for the reaction of $SO_4^{\bullet-}$ with SDBS was calculated as 3.8×10^8 M^{-1} s^{-1} from the decay of $SO_4^{\bullet-}$ at 450 nm (at pH 10) and it is similar to the value reported about 3.6×10^8 M^{-1} s^{-1} *[101]*.

The H-abstraction reaction of $SO_4^{\bullet-}$ from the alkyl chain was verified by monitoring the decay of $SO_4^{\bullet-}$ with the reaction of SDS in N_2 purged 0.5 mM SDS containing 20 mM $K_2S_2O_8$ and 20 mM t-Bu-OH at pH 10 by employing 14 Gy per pulse. The decay constant of $SO_4^{\bullet-}$ for the reaction with SDS was calculated as 4.7×10^5 s^{-1} at 440 nm and it was found to be about 1.5 times higher compared to the decay of $SO_4^{\bullet-}$ in a solution containing no SDS (spectra is not shown). It supports that the H-abstraction reaction of $SO_4^{\bullet-}$ from the alkyl chain of SDS and SDBS are of similar nature.

The absorption peaks of the transients formed by the reaction between SDBS and $O^{\bullet-}$ were also monitored in N_2O saturated 0.5 mM aqueous SDBS solution at pH 13.5 by applying 14 Gy per pulse (Figure 3.34c). The $O^{\bullet-}$, being a nucleophilic species cannot add to the benzene ring, rather it is known to react via one electron oxidation producing benzene radical cation followed by benzyl type radicals by the dissociation of C_α-hydrogen *[106]*. Therefore, it showed ΔOD/G features similar to the reaction between SBDS and $SO_4^{\bullet-}$. The higher peak intensity at 290 nm observed for the reaction between $SO_4^{\bullet-}$ and SDBS is attributed to more favourable formation of benzyl radicals by $SO_4^{\bullet-}$. Therefore, the higher extent of mineralization of SDBS is not because of the conjugative effect of both $^{\bullet}OH$ and $SO_4^{\bullet-}$, but because of the preferential formation of benzyl type of radicals via the formation of benzene radical cation.

3.4.5. The influence of the nature of neutralizing acid on the radiolysis of STDWW

The pH of the STDWW solution did not appreciably change even after 50 kGy dose of radiolysis (Figure 3.36a) because of the lesser extent of formation of the organic acids from the mineralization of the organic components of STDWW. On the other hand, the pH of the STDWW decreased to 6.3 on irradiating the solution in presence of $K_2S_2O_8$ for the same dose (Figure 3.36b) because of the higher extent of formation of the organic acids from the mineralization of the organic components. The $SO_4^{\bullet-}$ efficiently oxidises the organic compounds and itself converts into SO_4^{2-}, which is a conjugate base of strong acids (HSO_4^-, H_2SO_4). Therefore, the pH of the solution significantly decreased during radiolysis in presence of $K_2S_2O_8$ *[107]*. This phenomenon led to the existence of the organic acids in their protonated form and therefore, the rate constants of these acids with $SO_4^{\bullet-}$ decreased leading to almost negligible extent of mineralization at higher doses than 50 kGy *[107]*. Moreover, the HCO_3^- ion concentration in equilibrium with CO_3^{2-} increases with decreasing the pH and it minimizes the scavenging effect as HCO_3^- *[108]*. However, the minimum COD achieved in the irradiated solution (50 kGy) in presence of $K_2S_2O_8$ was 1558 ppm, which was much above the permissible discharge limit (≤ 250 ppm).

The acetic acid, which was used to adjust the pH of the simulated dye solution, is an organic acid and it contributes significantly in the residual COD of the irradiated solution. Therefore, we did the radiolysis of STDWW in presence of $K_2S_2O_8$ by replacing the acetic acid (organic acid) by H_2SO_4 (mineral acid) in the pH adjustment step. The STDWW solution, where the pH was adjusted by diluted H_2SO_4 will be henceforth designated as modified simulated textile dye waste water (MSTDWW). The initial CODs of the STDWW and MSTDWW were calculated as 3128 and 1544 ppm,

respectively. It could itself give an idea about the contribution of the acetic acid in the total COD of the simulated solution.

Moreover, the extent of mineralization of MSTDWW increased to 84% upon gamma irradiation for 50 kGy in presence of $K_2S_2O_8$ and the pH of the solution drastically decreased to about 2.1. Despite the incomplete mineralization, The COD of MSTDWW could bring down to 245 ppm (which is below the recommended discharge limit) upon irradiation for about 60 kGy in presence of $K_2S_2O_8$. The pH of the irradiated solution was remained constant in the range 1.5–2.0 (Figure 3.36c).

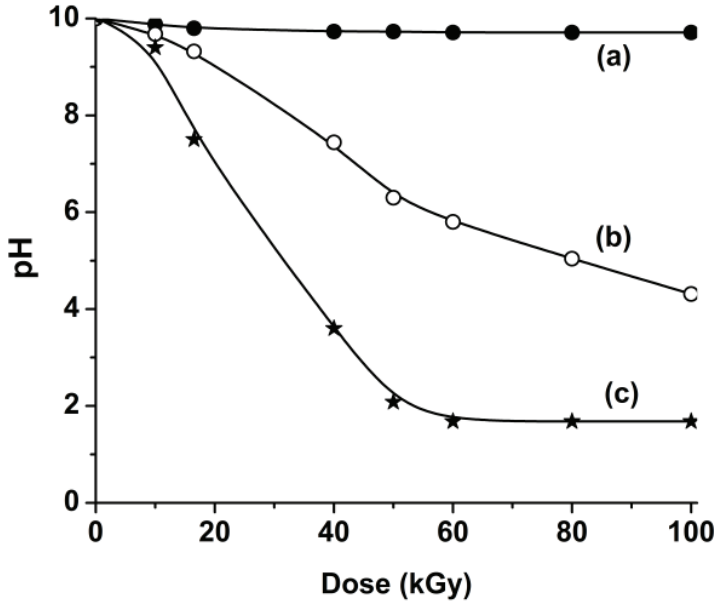

Figure 3.36 *Variation of pH as a function of dose during gamma radiolysis of STDWW in the (a) absence and (b) presence of $K_2S_2O_8$ and (c) MSTDWW in presence of $K_2S_2O_8$.*

Therefore, the use of H_2SO_4 in place of CH_3COOH in the pH adjustment step followed by the gamma radiolysis of STDWW in presence of $K_2S_2O_8$ is recommended for an effective effluent treatment process. Thus, further investigations on the process efficiency of radiolysis in comparison to other AOPs were performed on MSTDWW.

3.4.6. Radiolysis of MSTDWW in the presence of $K_2S_2O_8$

The mineralization of MSTDWW irradiated in the presence of 40 mM $K_2S_2O_8$ at different doses is shown in Figure 3.37a. It shows 20% and 75% mineralization at doses of 11 kGy and 60 kGy, respectively. It could be noted that, at the same time, only 16% and 54% mineralization was observed for the STDWW (pH adjusted with CH_3COOH). Furthermore, about 80% mineralization was observed for the gamma radiolysis of MSTDWW at the 60 kGy dose, while only 60% mineralization was observed for the gamma radiolysis of STDWW at 100 kGy (Figures 3.32b & 3.37a). Therefore, the nature of the pH adjusting acid influences the extent of the mineralization of MSTDWW with that of the STDWW. As discussed earlier, $K_2S_2O_8$ itself can produce $SO_4^{\bullet-}$ by thermal decomposition at 38-40 ºC, which is the usual temperature of the solution during gamma radiolysis. Therefore, the extent of mineralization of MSTDWW in the presence of 40 mM $K_2S_2O_8$ was studied at 40 ºC under room conditions (no irradiation), and here, no appreciable mineralization of MSTDWW was observed.

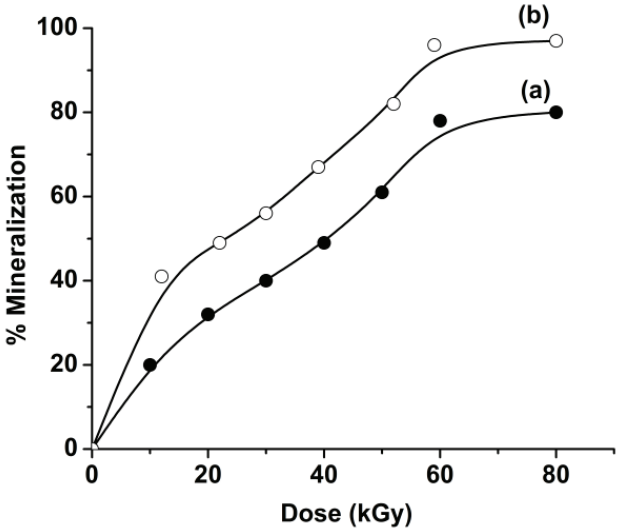

Figure 3.37 *Mineralization of MSTDWW in the presence of 40 mM $K_2S_2O_8$ during (a) gamma radiolysis and (b) EB radiolysis.*

The MSTDWW solution was irradiated at different doses by electron beam (EB) at pH 10 in the presence of 40 mM $K_2S_2O_8$. The extent of mineralization of MSTDWW increased with each dose by about 20% (Figure 3.37b). The high intensity electron beam rapidly deposits energy to the aqueous solution and elevates the temperature of the aqueous solution from ambient temperature *[109, 110]*. Therefore, it can be speculated that the high yield of $^{\bullet}OH$ and $SO_4^{\bullet-}$ (by the conjugated effects of radiolytic and thermal decompositions) enhances the % mineralization of MSTDWW to about 34% and 96% at 11 kGy and 60 kGy doses, respectively. At 60 kGy, the COD of the final solution was brought down to below 100 ppm, which is below the recommended limit of discharge (≤ 250 ppm).

3.4.7. Photocatalysis of MSTDWW

The photocatalysis of MSTDWW was carried out over different time intervals. However, only 30% mineralization of MSTDWW was observed after 10 hours of photocatalytic treatment (Figure 3.38a), and no appreciable change in the extent of mineralization was observed over longer times. It could be noted that only 24% mineralization of STDWW was observed under the same photocatalytic conditions (Figure 3.31a). It is important to mention that the TiO_2 nanoparticles made very stable suspensions with the aqueous solution of the individual components of MSTDWW. However, TiO_2 nanoparticles settled down rapidly in MSTDWW. The reason is quite similar as discussed in Section 3.4.1. Instead of molecular oxygen, $S_2O_8^{2-}$ can also take the CB electron from TiO_2 nanoparticles, thereby producing $SO_4^{\bullet-}$ (Eq. 3.5)

$$S_2O_8^{2-} + e^-_{CB} \rightarrow 2\ SO_4^{\bullet-} \qquad (3.5)$$

Therefore, the effect of $K_2S_2O_8$ on the photocatalytic degradation of MSTDWW was also investigated in the presence of 40 mM $K_2S_2O_8$. The extent of mineralization increased by about 10-12% during the photocatalysis of MSTDWW in the presence of

$K_2S_2O_8$ (Figure 3.38b). The increase in the %mineralization of MSTDWW during the photocatalysis in the presence of $K_2S_2O_8$ is attributed to: (i) the decrease in the probability of recombination of the photogenerated electrons and holes, and (ii) the formed $SO_4^{\bullet-}$ having higher mineralization efficiency. However, the application of this process is limited by the coulombic repulsion between the negatively charged surface of TiO_2 ($pH_{pzc} = 6.0 \pm 0.2$) and $S_2O_8^{2-}$ (at pH 10) and the rapid settlement of the catalyst in MSTDWW.

The photolysis (photochemical decomposition of $K_2S_2O_8$ in the absence of TiO_2) did not impart any enhancement in the extent of mineralization of MSTDWW (Figure 3.38c). This is speculated by the lower yield of $SO_4^{\bullet-}$ from the photolysis of $S_2O_8^{2-}$ with about 350 nm UV light *[111]*.

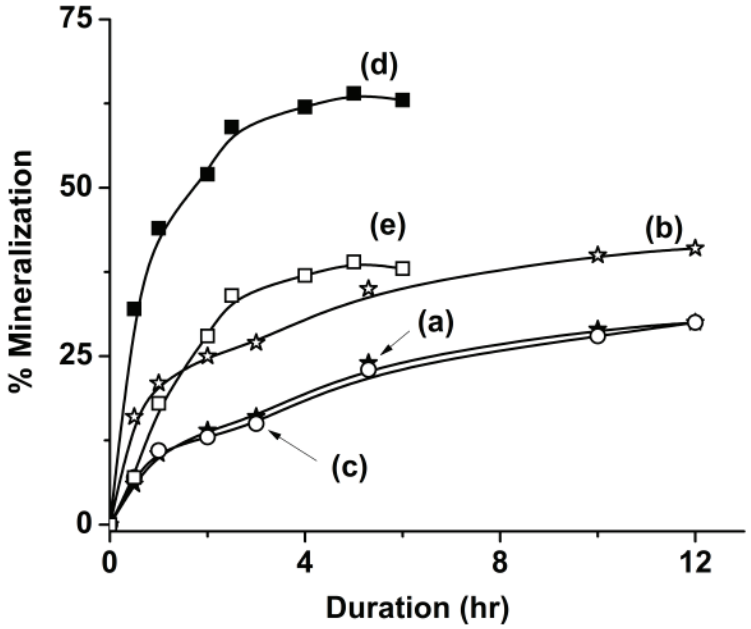

Figure 3.38 *Mineralization of MSTDWW over different durations in: (a) photocatalysis, (b) photocatalysis in the presence of 40 mM $K_2S_2O_8$, (c) photolysis in presence of 40 mM $K_2S_2O_8$, (d) ozonolysis, and (e) ozonolysis in the presence of 40 mM $K_2S_2O_8$.*

3.4.8. Ozonolysis of MSTDWW

The extent of mineralization of MSTDWW was studied at different durations of ozonolysis at pH 10. About 30% and 60% extent of mineralization of MSTDWW was achieved after 0.5 hours and 4 hours of ozonolysis, respectively. However, after 4 hours, no significant increase in the extent of mineralization was observed (Figure 3.38d). It should be noted that only 13% and 25% mineralization of STDWW was observed under the same ozonolytic conditions (Figure 3.31b). The effect of $K_2S_2O_8$ on the ozonolysis of MSTDWW was investigated in the presence of 40 mM $K_2S_2O_8$ (Figure 3.38e). The extent of mineralization decreased drastically in case of ozonolysis in the presence of $K_2S_2O_8$. The $K_2S_2O_8$ does not produce $SO_4^{\bullet-}$ during ozonolysis (in the absence of any radiation or thermal activation); instead, some of the $^{\bullet}OH$ radicals formed during ozonolysis will react with $K_2S_2O_8$ giving some products (Eq. 3.6) which may not react with components of MSTDWW.

$$^{\bullet}OH + K_2S_2O_8 \rightarrow \text{Products} \quad (3.6)$$

Therefore, the extent of %mineralization decreased during ozonolysis in presence of $K_2S_2O_8$.

3.4.9. Comparison of the process efficiencies of radiolysis, photocatalysis, and ozonolysis for the mineralization of MSTDWW

3.4.9.1. In terms of the OCC

The OCC of radiolysis (gamma and electron beam) (Eq. 3.4), photocatalysis/ photolysis (Eq. 3.2) and ozonolysis (Eq. 3.3) were calculated to compare the process efficiencies of different AOPs. It can be seen from Figure 3.39 that the lowest degree of mineralization of MSTDWW (to an extent of 28%) was observed in the photocatalysis and photolysis of $K_2S_2O_8$. Thus OCC values and the cost of the energy source and other

ancillary inputs of different AOPs were compared only for 28% mineralization of MSTDWW. It could be noted that the OCCs of radiolysis, photocatalysis, ozonolysis, and radiolysis (+$K_2S_2O_8$) of STDWW could be calculated only for 16% mineralization, which was the lowest observed degree of mineralization of STDWW (Figure 3.33). The OCC values of photocatalysis, photocatalysis (+$K_2S_2O_8$), photolysis in presence of $K_2S_2O_8$, ozonolysis, ozonolysis (+$K_2S_2O_8$), and gamma (+$K_2S_2O_8$) and EB (+$K_2S_2O_8$) radiolysis for 28% mineralization were calculated to be 6.29, 2.46, 7.63, 9.29, 38.83, 0.08, and 0.04 kg equivalent O_2 m^{-3}, respectively. EB radiolysis in the presence of $K_2S_2O_8$ showed a maximum chemical efficiency (about 96% mineralization) of the oxidants at 0.3 kg equivalent of O_2 m^{-3} OCC. About 78% mineralization was observed in gamma radiolysis, and less than 10% mineralizations were observed for others at 0.3 kg equivalent of O_2 m^{-3} OCC. It could be noted that 0.3 kg equivalent of O_2 m^{-3} OCC could mineralize only 54% of STDWW by gamma radiolysis in the presence of $K_2S_2O_8$ (Figure 3.33). Therefore, it could be safely concluded that the amount of oxidant required achieving the same extent of mineralization of MSTDWW by EB radiolysis was the least, compared to other processes studied here. Therefore, the OCC for a 28% mineralization of MSTDWW follows the order: EB (+$K_2S_2O_8$) radiolysis < gamma (+$K_2S_2O_8$) radiolysis < photocatalysis (+$K_2S_2O_8$) < photocatalysis ≈ photolysis in presence of $K_2S_2O_8$ < ozonolysis < ozonolysis (+$K_2S_2O_8$). The mechanism of enhancement in the extent of mineralization of STDWW (Section 3.4.4.), ibuprofen (Section 4.2) during radiolysis in the presence of $K_2S_2O_8$ has been studied in details. Since, only the nature of the pH adjusting acid changes, we speculate that the mechanism of mineralization of the components of MSTDWW was quite similar to that of STDWW.

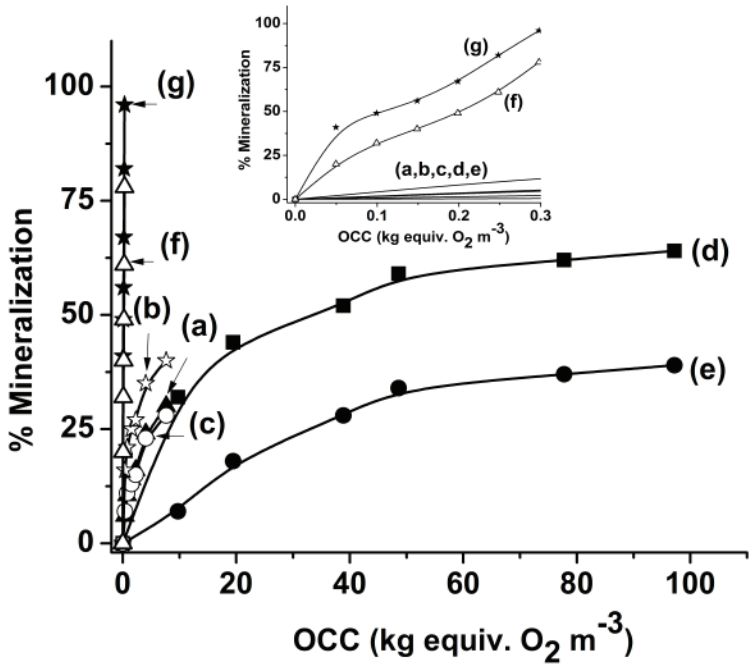

Figure 3.39 *Mineralization of MSTDWW with OCC for (a) photocatalysis, (b) photocatalysis in the presence of 40 mM $K_2S_2O_8$, (c) photolysis in presence of 40 mM $K_2S_2O_8$, (d) ozonolysis, (e) ozonolysis in the presence of 40 mM $K_2S_2O_8$, (f) gamma radiolysis in the presence of 40 mM $K_2S_2O_8$ and (g) EB radiolysis in the presence of 40 mM $K_2S_2O_8$.*

3.4.9.2. In terms of the cost of the energy source and other ancillary inputs

The efficiencies of EB (+$K_2S_2O_8$) and gamma (+$K_2S_2O_8$) radiolysis, photocatalysis (+$K_2S_2O_8$), and ozonolysis were evaluated in terms of the cost of energy and other ancillary inputs. The cost of the electrical energy required for EB (+$K_2S_2O_8$) radiolysis, photocatalysis (+$K_2S_2O_8$), and ozonolysis can be calculated using Eq. 3.7.

$$EEC = P \times \frac{t}{60} \times \frac{1000}{v} \qquad (3.7)$$

where EEC (in kWh m^{-3}) is the electric energy consumed (in kWh) to degrade a contaminant in unit volume (in m^3), P is the rated power (in kW) of the AOP system, t is the duration (in min) of treatment, and v is the volume (in L) of MSTDWW treated in

time t. The duration of treatment for 28% mineralization of MSTDWW by EB (+$K_2S_2O_8$) radiolysis, photocatalysis (+$K_2S_2O_8$), and ozonolysis were observed to be 0.6, 180, and 30 min, respectively. The cost of the electrical energy, along with the ancillary chemicals (if any), for these AOPs are summarized in Table 3.6. Among these processes, the costs involved in EB (+$K_2S_2O_8$) treatment were the lowest.

Table 3.6 *Comparison of the cost of energy and ancillary chemicals for different AOPs.*

	Ozonolysis	**Photocatalysis (+$K_2S_2O_8$)**	**Electron beam radiolysis**
Power employed in the process (kW)	0.08	0.128	1
Treatment time (min)	30	180	0.6
Volume of MSTDWW treated (L)[a]	0.04	0.26	1.9
EEC (kWh m^{-3}) of MSTDWW	1000	1477	5.3
Electrical energy cost (INR m^{-3}) of MSTDWW @INR 8.5 $(kWh)^{-1}$	8500	12554	45
Cost of additional chemicals or gas (INR m^{-3}) of MSTDWW	246000 (O_2 cylinder cost @ INR 164 m^{-3})	3000 (TiO_2 cost @ INR 3 g^{-1}) + 12975 ($K_2S_2O_8$ cost @ INR 1.2 g^{-1})	12975 ($K_2S_2O_8$ cost @ INR 1.2 g^{-1})
Total cost m^{-3} of MSTDWW	254500	28529	13020

[a] *Guided by the maximum volume capacity of the instrument to treat the MSTDWW under the same treatment condition.*

In the gamma radiolysis of MSTDWW (which did not involve electrical energy), the cost of the energy source could be estimated by accounting for five effective half-lives of ^{60}Co source using Eq. 3.8

$$CTP = I \times R \times \frac{t}{5\times365\times24\times t_{\frac{1}{2}}} \times \frac{1000}{v_{max}} \qquad (3.8)$$

where CTP (INR m^{-3}) is the average cost of the treatment process in Indian rupee (INR), I is the initial activity in Curie (Ci) of the ^{60}Co source, R is the price (in INR) of

^{60}Co source Ci^{-1}, t is the treatment time (in hours), $t_{1/2}$ is the half-life (hour) of ^{60}Co, and v_{max} is the maximum volume capacity (in L) of the gamma chamber that can be treated in time t. In our study, the initial activity of ^{60}Co was 10000 Ci, involving a cost of INR 70 Ci^{-1}, and volume of the gamma chamber was 5 L. Therefore, the cost for 28% mineralization using gamma radiolysis was calculated as INR 7931 m^{-3}. The total cost of gamma radiolysis ($+K_2S_2O_8$) for the treatment of MSTDWW was found to be INR 20906 m^{-3}. This is the first approach to calculate the equivalent cost of gamma radiolysis in comparison to other AOPs consuming electrical energy.

The above results showed that the cost involved in EB ($+K_2S_2O_8$) treatment was the lowest one among the studied AOPs for the mineralization of MSTDWW. It is important to note that the AOPs are emerging technologies currently being commercialized worldwide. A few UV/H_2O_2-based AOPs have been internationally commercialized for the treatment of drinking water and industrial water, using the advantage of both chemical and energy inputs *[112-115]*. There are few companies, such as AST clean water technologies, China; Trojan Technologies, Canada; Calgon Carbon Corporation and Xylem Global, US, who have brought some of the AOPs to international markets. In parallel, the radiation technology is internationally emerging for waste-water treatment *[116–118]*. Radiation-based pilot sludge treatment plants have been established in New Mexico, USA (Gamma); Weldel, Germany (EB); Verginia Key, USA (EB); Takasaki, Japan (EB); Sao Paulo, Brazil (EB); Tucuman, Argentina (Gamma); and Daejeon, Korea (EB) *[116-118]*. In addition, radiation-based commercial sludge treatment plants have also been established in Vadodara, India (Gamma), and Munich, Germany *[116-118]*. A pilot plant for treating 1000 m^3 day^{-1} of dyeing waste-water with EB has been constructed and operated since 1998 in Daegu, Korea, together with a biological treatment facility *[78, 79]*. Therefore, we understand

that the studies presented in this paper have a lot of scope to advance radiation-based technologies for the treatment of textile effluents. Furthermore, the EB has the ability to simultaneously disinfect the water during the degradation process *[119]*. At this stage, the used EB ($+K_2S_2O_8$) treatment process does not produce water suitable for reuse or for drinking. Hence, a multi-step treatment system would need to be designed in the near future.

CHAPTER 4

Degradation of 4-nitrophenol (4-NP) and Ibuprofen (IBP)

4.1. Radiolysis of aqueous solution of 4-Nitrtophenol

4.1.1. Structure of 4-Nitrophenol

The molecular structure of 4-Nitrophenol (4-NP) is shown in *Figure 4.1a*. A Lewis acid-base equilibrium between 4-NP and 4-Nitrophenate anion (4-NPAT) (Figure 4.1b) sets in the aqueous solution of 4-NP (Figure 4.1).

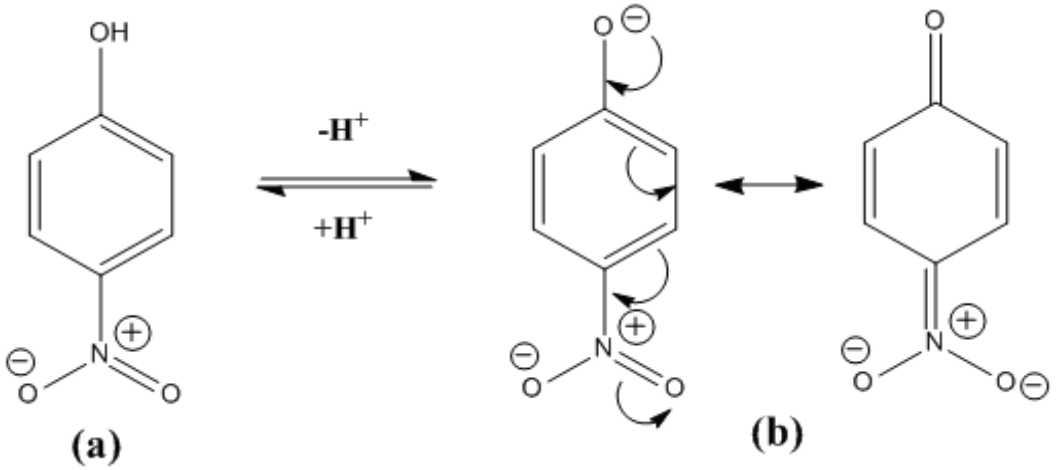

Figure 4.1 *Molecular structures of (a) 4-Nitrophenol and (b) 4-Nitrophenate anion.*

Figure 4.2a(i) shows the UV-visible spectrum of 0.1 mM 4-NP at pH 4. It shows two characteristics peak at 226 and 317 nm corresponding to the π-π^* and n-π^* transitions of 4-NP, respectively. The intensity of the peak at 317 nm decreased with increasing pH of the solution. Further, a new peak at 400 nm appeared and its intensity increased with increasing pH (Figure 4.2a). The absorbance peak at 400 nm corresponds to the π-π^* transition of the extended conjugation in 4-NPAT. The pK_a of 4-NP is calculated from the point of intersection of the plots of absorbance (at (i) 317 and (ii) 400 nm) as a function of pH (Figure 4.2b).

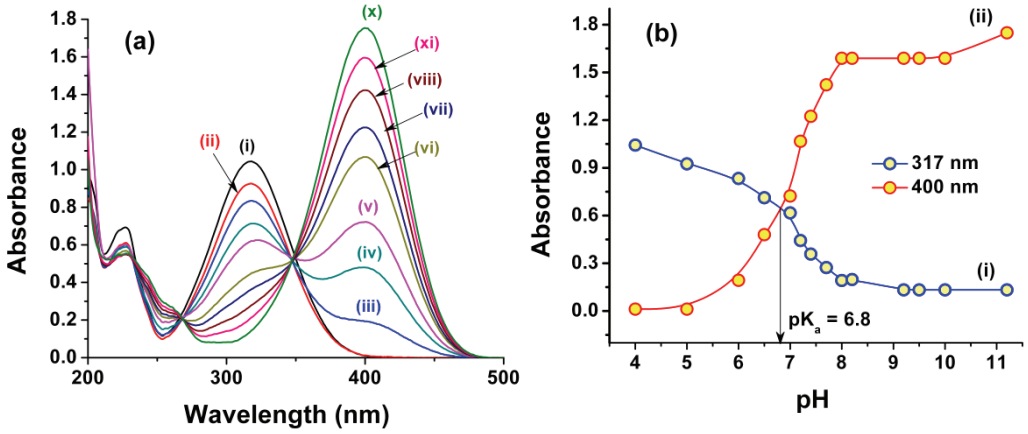

Figure 4.2 *(a) UV-visible absorbance spectra of 0.1 mM 4-NP at pH (i) 4.0, (ii) 5.0, (iii) 6.0, (iv) 6.5, (v) 7.0, (vi) 7.2, (vii) 7.4, (viii) 7.7, (ix) 8.0 and (x) 10.0. (b) Absorbance maxima at (i) 317 nm and (ii) 400 nm as a function of pH.*

4.1.2. Pulse radiolysis of 4-NP

Pulse radiolysis experiment was performed to understand the behaviour of the transient species produced by the reactions of 4-NP with different radicals. 4-NP has absorption up to 480 nm in pH range about 4-11. Therefore, the spectrum of the transient was corrected from the parent absorption by Eq. 2.5. The reaction between $^{\bullet}$OH and 4-NP was investigated by pulse radiolysis experiment employing 0.01 kGy/pulse in N_2O saturated, 0.1 mM 4-NP solution (at pHs 5.2 and 9.2). Figure 4.3 shows the corrected spectra of the transients produced by the reaction between $^{\bullet}$OH and 4-NP at pH (a) 5.2 and (b) 9.2. A strong absorption peak at 290 nm was observed at pH 5.2 (Figure 4.3a). On the other hand, two absorption bands at 300 and 400 nm were observed at pH 9.2 (Figure 4.3b). $^{\bullet}$OH is an electrophile. Hence it firstly forms a π-complex with the aromatic ring of 4-NP (Figure 4.4). This π-complex is very unstable and it readily disappears through three different paths. The π-complex readily

dehydrates to generate 4-nitrophenoxy radical (path (a) of Figure 4.4), which absorbs at ~400 nm *[120]*. This reaction is dominated in the alkaline solution. Therefore, the intensity of the transient at 400 nm increased at pH 9.2 (Figure 4.3b).

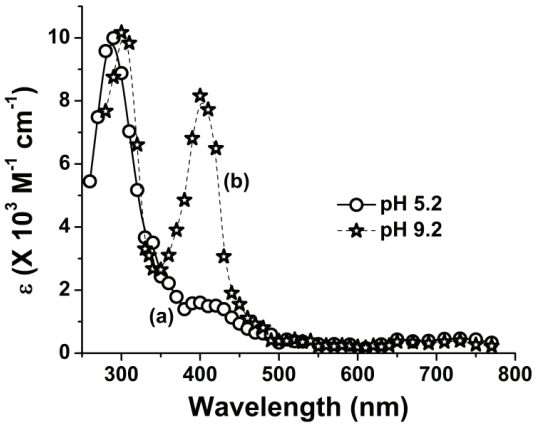

Figure 4.3 *Spectra of the transients produced by the reaction between •OH and 4-NP at pH (a) 5.2 and (b) 9.2.*

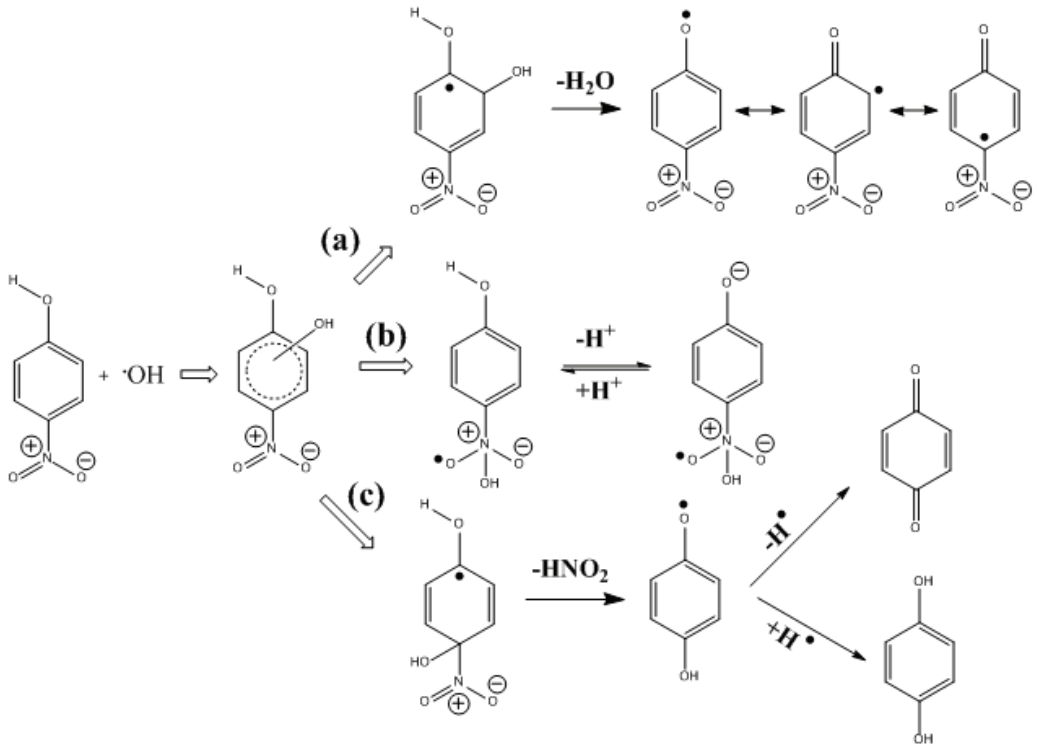

Figure 4.4 *The reactions between 4-NP and •OH.*

The transient peak at 289 nm represents the formation of $HOC_6H_4NO_3^{\bullet -}$ by reaction path (b) in Figure 4.4 *[121-123]*. To a minor extent, $^{\bullet}OH$ adds to the para-position of phenolic group (Reaction (c) of Figure 4.4), which is followed by rapid elimination of HNO_2, generating semiquinone radical. This radical is inclined to be reduced to generate p-benzoquinone or be oxidized to generate hydroquinone *[121]*. k_{φ} for the reaction of $^{\bullet}OH$ with 4-NP was determined in the presence of different concentrations of 4-NP. The bimolecular rate constant of $^{\bullet}OH$ with 4-NP was calculated as 4.1×10^9 M^{-1} s^{-1} (for pH 5.2) and 8.7×10^9 M^{-1} s^{-1} (for pH 9.2) from the slope of the plot of k_{φ} versus concentrations of 4-NP.

The reaction between $N_3^{\bullet}$ and 4-NP was investigated by pulse radiolysis experiment employing 0.01 kGy/pulse in N_2O saturated 0.1 mM 4-NP solution (at pHs 5.2 and 9.2) containing 20 mM NaN_3. Figure 4.5 shows the corrected spectra of the transients produced by the reaction between $N_3^{\bullet}$ and 4-NP at pH (a) 5.2 and (b) 9.2.

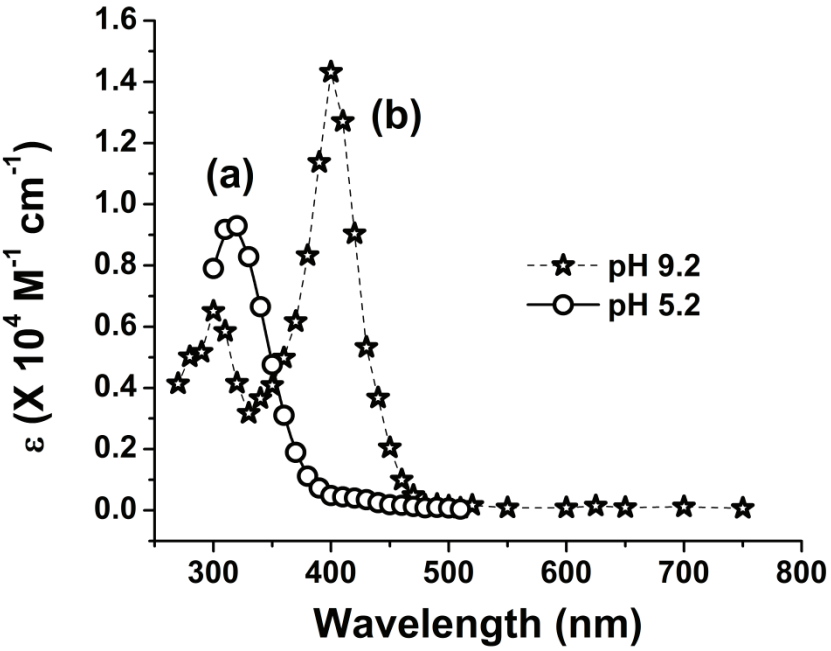

Figure 4.5 *Spectra of the transients produced by the reaction between $N_3^{\bullet}$ and 4-NP at pH (a) 5.2 and (b) 9.2.*

The broad peak at 315 nm represents the formation of semi-quinone radical anion at pH 5.2 (Figure 4.5a) *[124]*. On the other hand, the additional bands at 400 nm observed at pH 9.2 (Figure 4.5b) represents the 4-nitrophenoxy radical. . The bimolecular rate constant of $N_3^{\bullet}$ with 4-NP was calculated as 6.5×10^9 M^{-1} s^{-1} (for pH 9.2).

The reaction between e^-_{aq} and 4-NP was investigated by pulse radiolysis experiment employing 0.01 kGy/pulse in N_2 saturated 0.1 mM 4-NP solution (at pHs 5.2 and 9.2). Figure 4.6 shows the corrected spectra of the transients produced by the reaction between e^-_{aq} and 4-NP at pH (a) 5.2 and (b) 9.2. A strong absorption peak at 314 nm was observed at pH 5.2 (Figure 4.6a). The absorption band shifted to longer wavelength (400 nm) at pH 9.2 (Figure 4.6b).

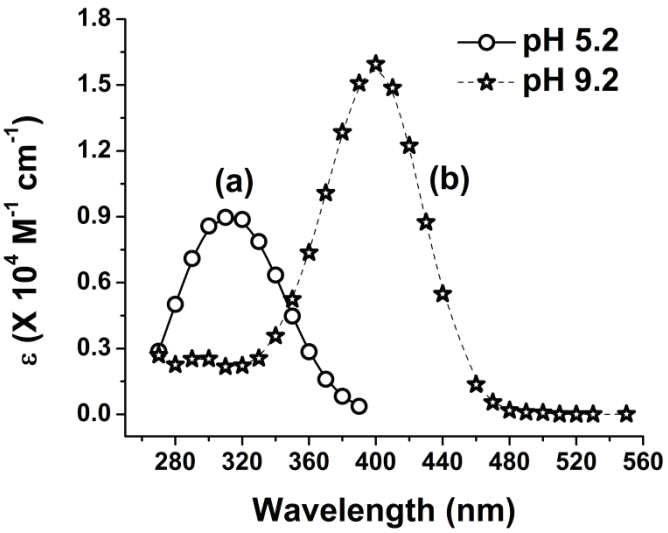

Figure 4.6 *Spectra of the transients produced by the reaction between e^-_{aq} and 4-NP at pH (a) 5.2 and (b) 9.2.*

The transient peak at 314 nm corresponds to the transient $HOC_6H_4NO_2^{\bullet-}$ (Figure 4.7a). Further, the absorption at 400 nm in alkaline solution represents the transient $^-OC_6H_4NO_2^{\bullet-}$ (Figure 4.7b). The bimolecular rate constant of the reaction between e^-_{aq} and 4-NP was calculated as 2.8×10^{10} and 2.0×10^{10} M^{-1} s^{-1} at pH 5.2 and 9.2,

respectively. The coulombic repulsion between e^-_{aq} and $^-OC_6H_4NO_2^{\bullet -}$ decreases the value of the rate constant at pH 9.2.

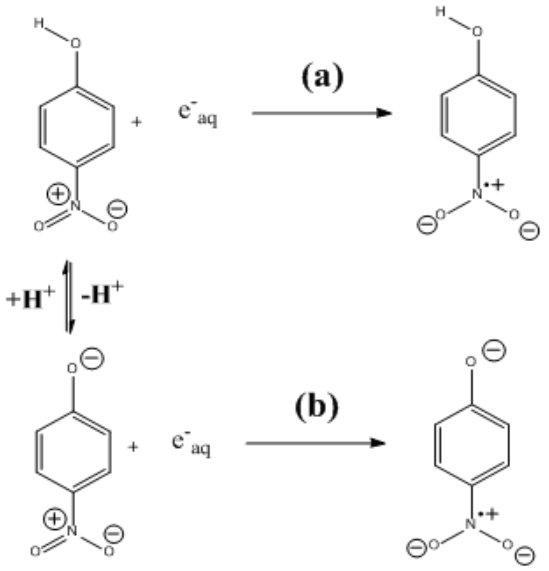

Figure 4.7 *The reaction between e^-_{aq} and 4-NP at pH (a) 5.2 and (b) 9.2.*

The reaction between 4-NP and 2-hydroxypropyl radicals was studied by pulse radiolysis experiment employing 0.01 kGy/pulse in N_2O saturated 0.5 mM 4-NP solution (at pHs 5.2) containing 0.5 M 2-propoanol. The corrected absorption spectrum of the transient species showed similar features as the spectrum shown in Figure 4.6a. Therefore, it can be concluded that 2-hydroxy propyl radical quantitatively transfers electron to 4-NP. The bimolecular rate constant is calculated as 1.3×10^9 M^{-1} s^{-1}.

Methyl viologen (MV^{2+}) is well-known oxidant having λ_{max} at 605 nm (ε = 12,800 M^{-1} cm^{-1}). The standard reduction potential (E_0) of MV^{2+}/ $MV^{\bullet +}$ is -0.45 V vs. NHE. Therefore, the reductant nature of $HOC_6H_4NO_2^{\bullet -}$ was checked by its electron transfer reaction to MV^{2+}. The transient species, $HOC_6H_4NO_2^{\bullet -}$, formed during pulse radiolysis of N_2 saturated 0.1 mM 4-NP solution (pH 5.2) containing 0.5 M ^{t}BuOH and 28 μM MV^{2+} decayed with time confirming the reduction of MV^{2+} by $HOC_6H_4NO_2^{\bullet -}$ as per Eq. 4.1.

$$HOC_6H_4NO_2^{\bullet-} + MV^{2+} \rightarrow HOC_6H_4NO_2 + MV^{+} \qquad (4.1)$$

The bimolecular rate constant was calculated as 5.3×10^8 M^{-1} s^{-1}. Hence the reduction potential of $HOC_6H_4NO_2^{\bullet-}$ is more negative than -0.45 V vs. NHE.

4.1.3. Steady state gamma radiolysis of 4-NP

The steady state degradation of aqueous solution of 4-NP was studied by monitoring the absorbance of 0.1 mM 4-NP solution at 317 nm under different irradiation conditions (Figure 4.8). About 84%, 97.6%, 98.5%, 99.5% and 100% decolouration at 317 nm of 4-NP was observed after radiolysis at 4.4 kGy dose in (i) N_2, (ii) air, (iii) O_2, (iv) N_2O and (v) (1:1) N_2O:O_2 purged solution (Figure 4.8). $^{\bullet}OH$ and e^-_{aq} are the predominant radicals in N_2 saturated solution. It showed least % decolouration among the studied systems. The % decolouration increased in air and oxygen saturated solution. The concentration of dissolved oxygen in air and oxygen saturated solutions are 0.24 and 1.2 mM, respectively. Therefore, it can be concluded that dissolved oxygen may be used during radiolysis in the degradation steps of 4-NP. Although the rate of % decolouration is slower at the initial stage, the % decolouration of 4-NP increased in N_2 purged solution containing ^{t}Bu-OH. This is attributed to the slow generation of the reduced product ($HOC_6H_4NO_2^{\bullet-}$), which is further effectively fragmented. The % decolouration slightly increased in N_2O saturated solution due to the oxidative degradation of 4-NP by $^{\bullet}OH$. The OH-adduct formed by the reaction between $^{\bullet}OH$ and 4-NP is more prone to degrade in presence of dissolved oxygen. Therefore, maximum (~ 100%) decolouration was observed for the radiolysis of 4-NP in (1:1) N_2O:O_2 purged solution.

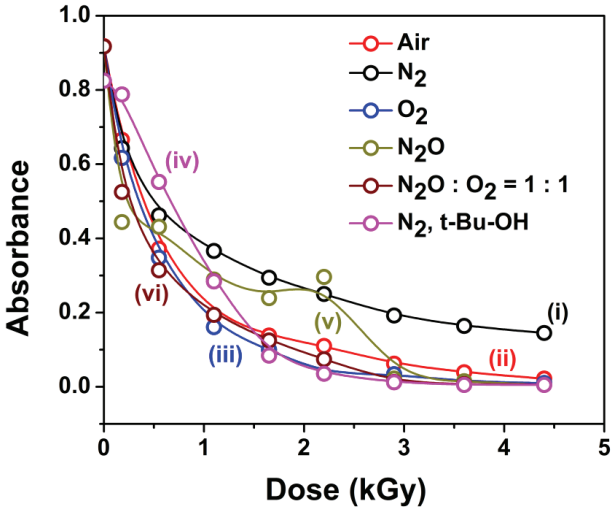

Figure 4.8 *% decolouration at 317 nm of 4-NP as a function of dose in 0.1 mM 4-NP solution purged with (i) N_2, (ii) air, (iii) O_2, (iv) N_2O and (v) (1:1) N_2O:O_2.*

4.2. Radiolysis of aqueous solution of Ibuprofen (IBP)

4.2.1. The variation of COD and TOC on gamma irradiation of aqueous IBP solution

Steady state gamma radiolysis of 1 mM aqueous solution of IBP was carried out at pH 7 for different absorbed doses. The (a) % COD removal and (b) % TOC removal of aqueous IBP solution as a function of absorbed doses is shown in Figure 4.9. Both the mineralization parameters increased with increasing the dose. For the same does, the extent of % COD removal is more compared to the extent of % TOC removal as similarly observed for the mineralization of RR-120 (Section 3.1.5). To the extent of 20% and 14% removal of COD and TOC were observed at 50 kGy and no further significant change in % COD removal or % TOC removal was observed at doses higher than 50 kGy. Therefore, $^{\bullet}OH$, the predominant oxidizing radical present in the reaction condition, can not alone effectively mineralize aqueous IBP solution. Hence an alternative AOP was investigated to increase the radiolytic mineralization efficacy of IBP.

Steady state gamma radiolysis of 1 mM aqueous solution of IBP was carried out at pH 7 for different absorbed doses in the presence of 20 mM $K_2S_2O_8$. About (c) 84% and (d) 82% removals of COD and TOC were observed in presence of $K_2S_2O_8$ at 50 kGy dose, respectively (Figure 4.9). During the radiolysis of aqueous IBP solution in presence of $K_2S_2O_8$, the e^-_{aq} and $^\bullet H$ react with $S_2O_8^{2-}$ in accordance with well established reactions (Eq. 1.34) producing $SO_4^{\bullet-}$. Thus in the presence of $K_2S_2O_8$, both $^\bullet OH$ and $SO_4^{\bullet-}$ are available to oxidize IBP.

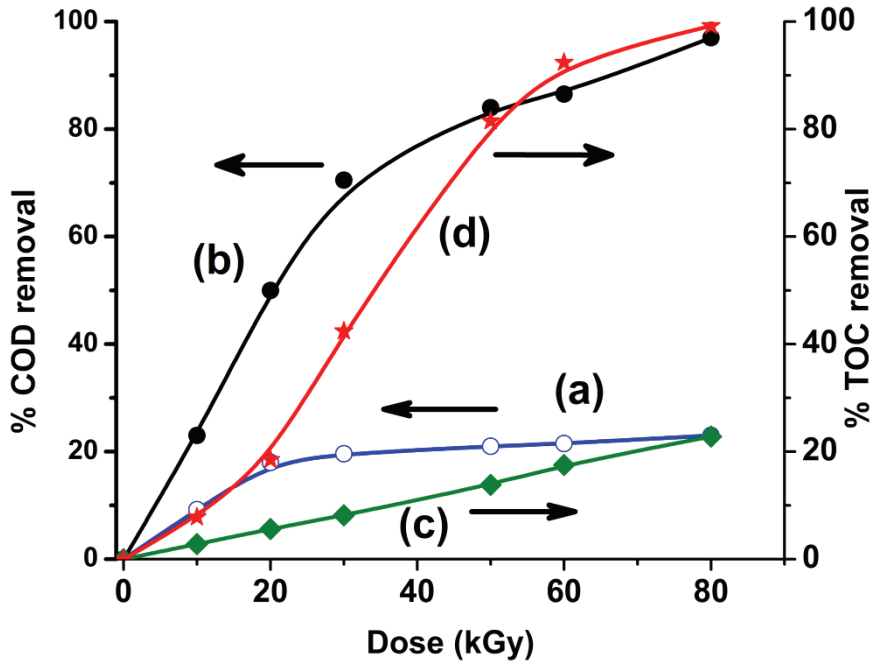

Figure 4.9 *(a, b) % COD removal and (c, d) % TOC removal in the absence (a, c) and in the presence (b, d) of $K_2S_2O_8$ during gamma radiolysis of IBP as a function of absorbed dose.*

Table 4.1 shows that the ratio of % COD removal of IBP in the presence and in the absence of $K_2S_2O_8$. It indicates that although in presence of $K_2S_2O_8$, the yield of oxidizing radicals increased by 2.2 times, the extent of mineralization was enhanced by more than 2.2 times. Therefore, it can be envisaged that the generated $SO_4^{\bullet-}$ reacts efficiently with IBP leading to the higher extent of mineralization. In this context, it

should be mentioned that $K_2S_2O_8$ itself may oxidize the organic pollutants. Therefore, the extent of mineralization of 1 mM aqueous solution of IBP in the presence of 20 mM $K_2S_2O_8$ was studied at room temperature for several hours without any irradiation. Under such condition no significant mineralization of IBP was observed. Therefore, $K_2S_2O_8$ could not oxidize IBP in absence of irradiation.

Table 4.1 *A comparative study of IBP mineralization during gamma radiolysis in the absence and the presence of* $K_2S_2O_8$.

Dose (kGy)	% decrease in COD in absence of $K_2S_2O_8$ (A ± σ)	% decrease in COD in presence of $K_2S_2O_8$ (B ± σ)	Ratio (B/A)
10	9.2 ± 0.5	23.0 ± 0.2	2.5
20	18.0 ± 0.2	50.0 ± 0.2	2.8
30	19.6 ± 0.1	70.5 ± 0.1	3.6
50	21.0 ± 0.2	84.0 ± 0.1	4.0
60	21.5 ± 0.3	86.5 ± 0.2	4.0
80	23.0 ± 0.1	97.0 ± 0.1	4.2

The IBP solutions were irradiated, both in the presence and absence of $K_2S_2O_8$, in an open condition at low dose rate and thus the partial replenishment of dissolved oxygen (DO) would always be in solution. The DO concentration, immediately after irradiation at 50 kGy, was calculated as about 2 ppm for both the solutions. Therefore, the DO concentration is not expected to affect the comparative mineralization of IBP.

4.2.2. Pulse radiolysis of IBP in the presence of radiolytically generated oxidizing species

The reaction between IBP and $^{\bullet}OH$ was investigated by pulse radiolysis technique equipped with optical detection measurement. The reaction of IBP with $^{\bullet}OH$ was studied in N_2O saturated 0.5 mM aqueous IBP solution at pH 7 by employing 14

Gy/pulse. Under this experimental condition e^-_{aq} is converted to $^\bullet OH$ by N_2O by following the reaction (1.29). The change in absorbance per unit G value (ΔOD/G) of the transient species formed by the reaction of IBP with $^\bullet OH$ at 2 μs time scale is shown in Figure 4.10a(i), where G($^\bullet OH$) = 5.4. The spectrum (Figure 4.10a(i)) shows strong characteristic absorptions at 270, 315 and 330 nm as similarly reported in the literature *[102,103, 125]*. In this context, it is important to mention that IBP itself has ground level absorption in 250-280 nm range; therefore, observed spectrum was corrected for parent absorption using Eq. (2.5). The corrected absorption spectrum of the transient is shown in Figure 4.10b(i), which clearly shows transient species also, has substantial absorption in the region from 250-280 nm.

The reaction of IBP with $SO_4^{\bullet-}$ was studied in N_2 purged 0.5 mM aqueous IBP solution containing 20 mM $K_2S_2O_8$ and 0.5 M ^{t}Bu-OH by employing 14 Gy / pulse at pH 7. $^\bullet OH$ is scavenged by ^{t}Bu-OH in accordance with reaction (1.35). The bimolecular rate constant for the reaction of $SO_4^{\bullet-}$ with IBP was calculated as 3.8×10^9 M^{-1} s^{-1} from the decay of $SO_4^{\bullet-}$ at 450 nm at pH 7. ΔOD/G of the transient species formed by the reaction of IBP with $SO_4^{\bullet-}$ at 2 μs time scale is shown in Figure 4.10a(ii),where G($SO_4^{\bullet-}$) = 2.7. The transient species formed by the reaction of IBP with $SO_4^{\bullet-}$ also showed absorption maxima at 270, 310-320 nm as similarly observed for the reaction of IBP with $^\bullet OH$. However, the intensity of the peak at 270 nm increased by about 4 times for the reaction with $SO_4^{\bullet-}$, whereas, simultaneously the intensity of the broad peaks at 310-320 nm decreased significantly. The observed spectrum was corrected for ground state absorption of solute (as discussed earlier) and the corrected absorption spectrum of the species is given in Figure 4.10b(ii).

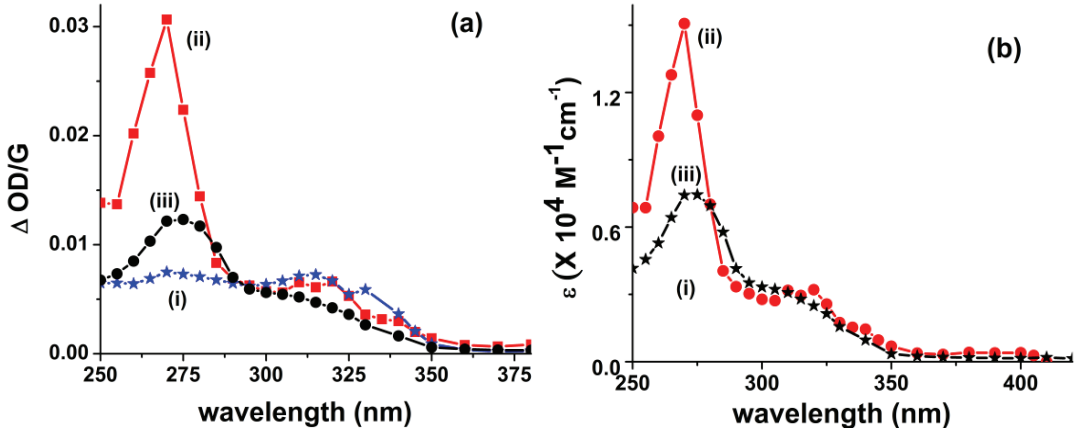

Figure 4.10 *(a) ΔOD/G plot and (b) corrected absorption spectra of the transient absorption spectra for reaction of IBP with (i) $^{\bullet}OH$, (ii) $SO_4^{\bullet-}$ (iii) $O^{\bullet-}$ at 14 Gy/pulse.*

The reaction of IBP with $O^{\bullet-}$ was studied in N_2O saturated 0.5 mM aqueous IBP solution at pH 13.5 by employing 14 Gy / pulse. $^{\bullet}OH$ is rapidly converted in strong alkaline solution to its conjugate base $O^{\bullet-}$ in accordance with reaction (1.23). The ΔOD/G of the transient species formed by the reaction of IBP with $O^{\bullet-}$ at 2 μs time scale is shown in Figure 4.10a(iii), where $G(O^{\bullet-}) = 5.4$. It also shows a peak at 275 nm with intensity lesser than peak observed for $SO_4^{\bullet-}$ reaction, but higher than the peak observed for $^{\bullet}OH$ reaction. However, no prominent peak was observed at 310-320 nm.

The overall results suggest that the radiolytic yield of each transients having characteristic peak depends on the type of radicals and solution composition. In this context, it is important to mention that the nature and the mechanism of formation of these transients are debatable. In a similar pulse radiolysis experiment of IBP with $^{\bullet}OH$ at pH 4.4, Illes et al. have observed higher intensity of the peak at 330 nm compared to the peak at about 280 nm and the authors assumed, on the basis of low intensity of absorbance, that the absorption around 285 nm corresponds to the hydroxyl-

cyclohexadienyl radical *[125]*. On the other hand, in pulse radiolyis of p-cumenesulfonate (a similar type of aryl structure) with •OH radical at pH 6.5, Osiewala et al. have observed higher intensity of the peak at 280 nm compared to the peak at 330 nm *[102]*. They have also confirmed that the peak around at 270-290 nm attributed to the benzyl type radical and broad peak at 300-350 nm corresponds to the formation of OH-adduct with the benzene ring. In our pulse radiolysis experiment for the reaction of IBP with •OH at pH 7, we have observed almost comparable intensities of the transient peaks at 270 nm and 315 nm. Therefore, we have studied the change in the transient peak intensities at 270, 315 and 330 nm by pulse radiolysis of IBP with •OH as a function of pH ranging from 4.4 to 9 (Figure 4.11). At pH 4.4, the intensity of the peak at 270 nm is lesser than the intensity of the peak at 315 nm. The intensity of the 270 nm peak increased, but 315 nm decreased with increasing pH and the intensities of both the peaks became almost comparable at pH 7. At pH > 7, the intensity of the peak at 270 nm became higher than the intensity of the peak at 315 nm. The peak intensity at 330 nm gradually decreased with increasing pH. At this point, it can be assumed that •OH radical first conjugates with the benzene ring of IBP forming the OH-adduct, which reacts with the water molecules leading to the formation of the benzene radical cation (Figure 4.12a). The benzene radical cation is unstable (life time < 0.1 μs) and it forms a benzyl type radical by dissociation of the weak benzylic C_α-hydrogen *[103]*. Both the intermediates viz. OH-adduct and benzyl type radicals are observed for the reaction of •OH. The dissociation of the weak benzylic C_α-hydrogen is pH dependent and it increases at higher pH. Apart from this above phenomenon, direct H-atom abstraction may also take place from the alkyl chain of IBP by •OH *[125]*.

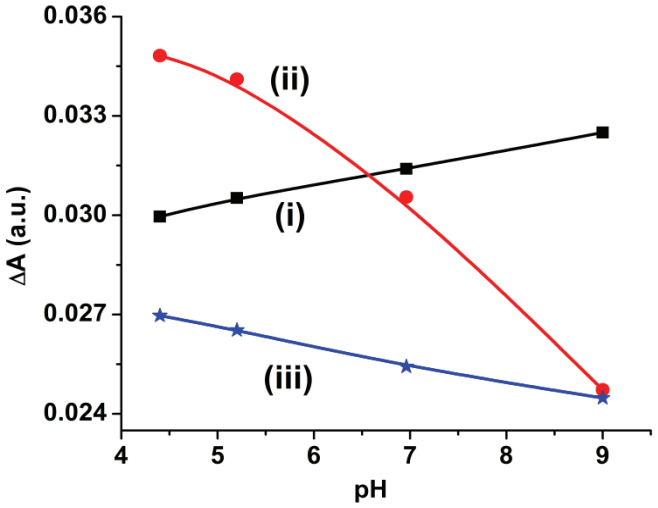

Figure 4.11 *Variation in the transient peak intensities at (i) 270, (ii) 315 and (iii) 330 nm, as a function of pH, by the reaction between IBP and •OH.*

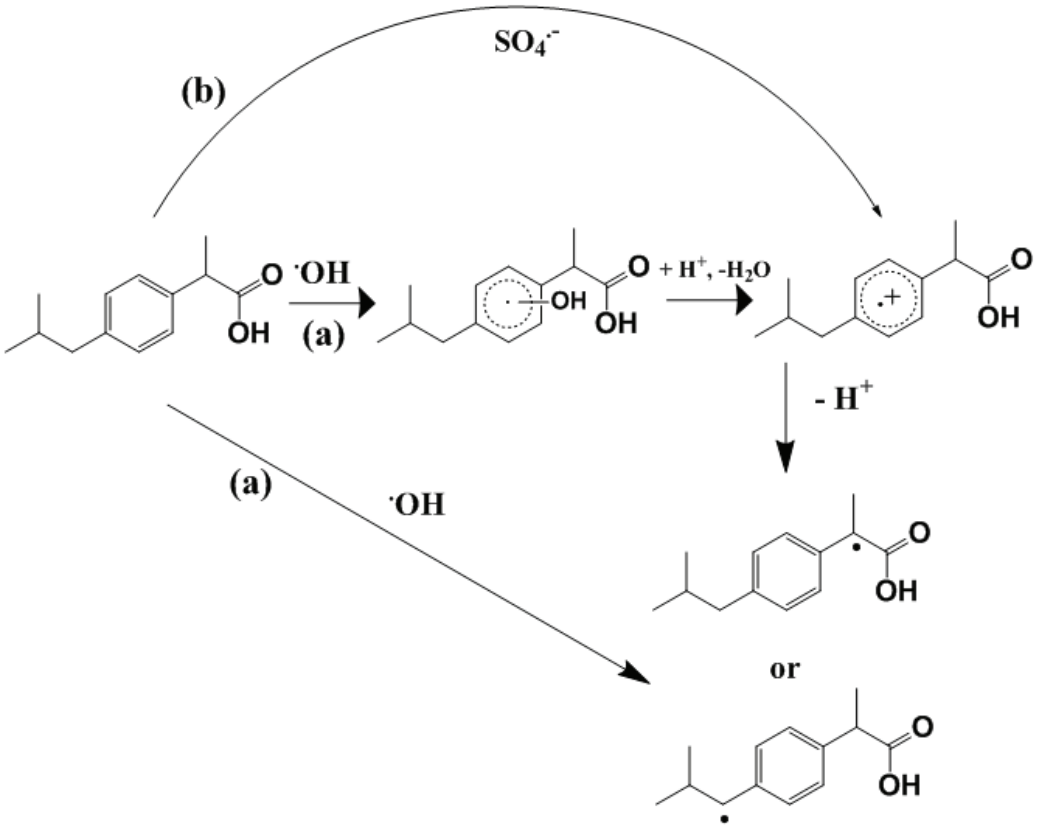

Figure 4.12 *Reaction scheme of IBP with (a) •OH and (b) $SO_4^{\bullet -}$.*

Figure 4.13 shows the formation traces of the transients having absorption peaks at 270 and 315 nm produced from the reactions of IBP with $^{\bullet}OH$ and $SO_4^{\bullet-}$ at pH 7. The yield of the transients (having absorption peaks at 270 and 315 nm) is almost same for the reaction of $^{\bullet}OH$ with IBP; whereas the yield of the transient (absorbing at 270 nm) is much higher compared to the yield of the transient (absorbing at 315 nm) for the reaction of $SO_4^{\bullet-}$ with IBP. This may be attributed to the direct formation of the benzene radical cation followed by the benzyl type radical (Figure 4.12b). That is why, the intensity of the peak corresponding to the benzylic radical (absorbing at 270 nm) increased significantly for the reaction of IBP with $SO_4^{\bullet-}$. However, the formation of OH-adduct (absorbing at 310-320 nm) can not be completely prevented because of incomplete scavenging of $^{\bullet}OH$ *[103]*. Figure 4.13a shows the decay profiles of the transients (absorbing at 315 nm) produced from the reaction of IBP with $^{\bullet}OH$ and $SO_4^{\bullet-}$. The slopes of the decay traces are almost similar for both the reactions. On the contrary, the rate of decay of the transient (absorbing at 270 nm) is much higher for the reaction of $SO_4^{\bullet-}$ in comparison to the rate of decay of the transient (absorbing also at 270 nm) for the reaction of $^{\bullet}OH$ (Figure 4.13b).

$O^{\bullet-}$ is a nucleophilic species. Therefore, it can not form adduct with the benzene ring, rather it is known to react via one electron oxidation producing benzene radical cation followed by benzyl type radicals by the dissociation of C_α-hydrogen (Figure 4.10a(iii)) *[106]*. Therefore, $O^{\bullet-}$ showed $\Delta OD/G$ feature similar to that of the reaction of $SO_4^{\bullet-}$.

Figure 4.14a shows the decay of transient species (absorbing at 270 nm) in the presence of O_2 and it suggests that the reaction between IBP and $SO_4^{\bullet-}$ produced carbon centered radical i.e. most likely benzyl type radicals. Figure 4.14b shows the decay of the transient at 270 nm at different concentration of $K_2S_2O_8$ and no significant

change was observed in the transient decay with increasing the concentration of $K_2S_2O_8$. The rate constant of the reaction of $K_2S_2O_8$ with IBP radical was estimated < 10^5 M^{-1} s^{-1}. Therefore, the reaction between $K_2S_2O_8$ and IBP radical could not be investigated under pulse radiolysis condition. However, during the gamma radiolysis, the reactivity of IBP radical would be expected to be more for the reaction with $K_2S_2O_8$. Therefore, $K_2S_2O_8$ can oxidize IBP radical under gamma radiolysis.

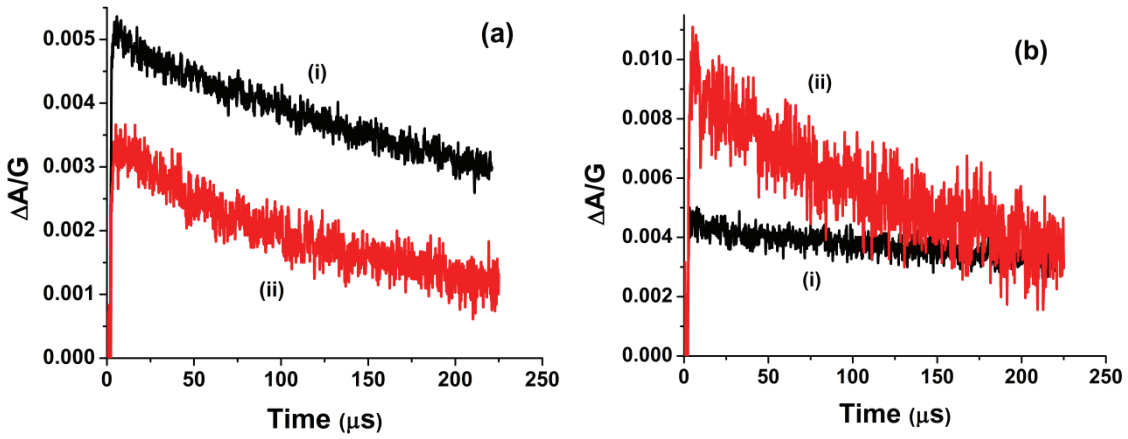

Figure 4.13 *Decay profiles of the transients absorbing at (a) 315 and (b) 270 nm for the reaction of IBP with (i) $^{\bullet}OH$ and (ii) $SO_4^{\bullet-}$.*

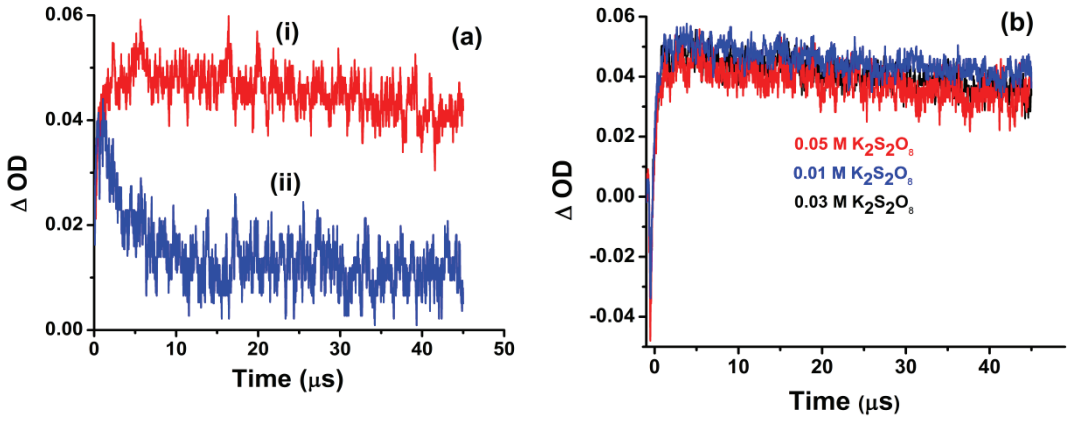

Figure 4.14 *Decay profiles of the transients absorbing at 270 nm for the reaction of IBP with $SO_4^{\bullet-}$ in (a) absence (i) and presence (ii) of O_2 and (b) at different concentrations of $K_2S_2O_8$.*

4.2.3. Gamma radiolysis studies of IBP in presence of radiolytically generated oxidizing species

Section 4.2.2 describes the pulse radiolysis studies of IBP in the presence and in the absence of $K_2S_2O_8$ and it shows the production of benzyl and cyclohexadienyl type of radical having absorption at 270 and 315, 330 nm, respectively. Further gamma radiolysis of IBP under similar conditions produces stable intermediate products having absorption at 260 nm. In order to study the rate of product formation, the relative absorbance of the products with reference to the parent absorption (ΔA) were plotted as a function of dose both in the absence and in the presence of $K_2S_2O_8$ (Figure 4.15a and b). Figure 4.15a shows that ΔA increases with dose up to 5.8 kGy followed by a slow decrease in ΔA with further increasing dose. On the contrary, Figure 4.15b shows an increase in ΔA values only up to 1.4 kGy and then it decreases rapidly at higher doses. It suggests that low doses are required for the fragmentation of the intermediate products formed during the radiolysis of IBP in the presence of $K_2S_2O_8$ as compared to fragmentation in the absence of $K_2S_2O_8$. Figure 4.15c shows the relative absorbance of the intermediate products with reference to the parent absorption per unit yield of the oxidant ((ΔA)/G of oxidant) both in the absence and in the presence of $K_2S_2O_8$. Here we should mention that the yields of oxidant were taken as 2.7 ($G(^{\bullet}OH)$) in the absence of $K_2S_2O_8$ and 6 ($G(^{\bullet}OH) + G(SO_4^{\bullet-})$) in the presence of $K_2S_2O_8$. Though the presence of $K_2S_2O_8$ increases the yield of the oxidizing radicals by a factor of 2.2, but the (ΔA)/G value at 260 nm was significantly changed to about 5 times at each dose in the presence of $K_2S_2O_8$. Therefore, it suggests that, while reacting with IBP, $SO_4^{\bullet-}$ produces major intermediates which get further fragmented. Therefore, $SO_4^{\bullet-}$ is a better mineralizing agent for IBP compared to $^{\bullet}OH$ radical at pH 7.

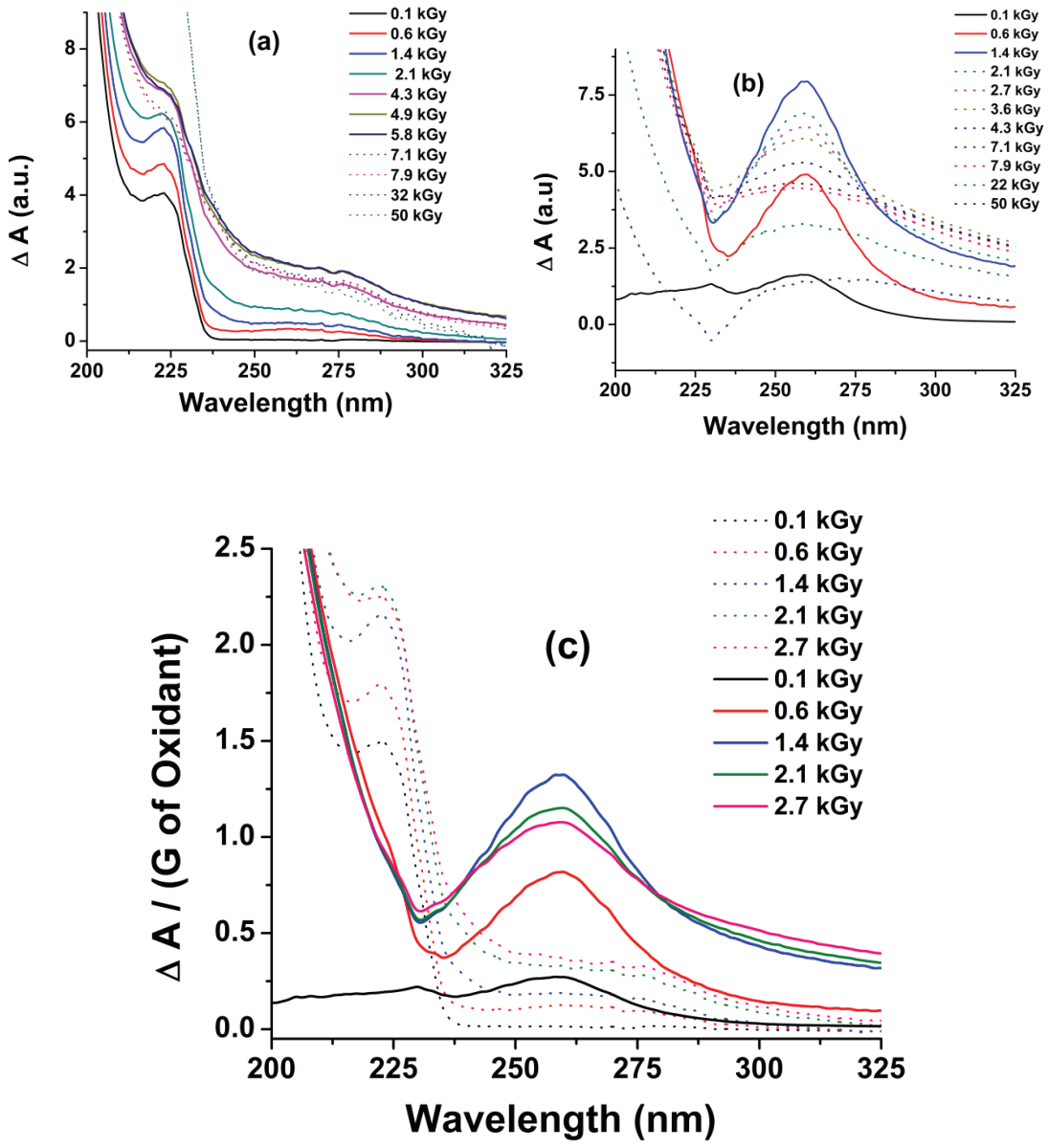

Figure 4.15 *The relative absorbance, with reference to the parent absorption (ΔA), of the products formed by steady state gamma radiolysis of IBP as a function of dose in (a) absence and (b) presence of $K_2S_2O_8$; (c) relative absorbance of the intermediate products with reference to the parent absorption per unit yield of the oxidant ((ΔA)/G of oxidant) at selected doses in the absence (dotted lines) and the presence (solid lines) of $K_2S_2O_8$.*

SUMMARY

Summary

The work reported in this thesis describes the results of interaction of high energy radiation with organic pollutants present in waste water. Various findings of the work indicate that radiation technology can be successfully used for degradation of organic pollutants such as RR-120 dye, ibuprofen and 4-nitrophenol present in waste water to safe level. It has been observed that only irradiation may not lead to an adoptable approach for overcoming the pollutant concentration in the waste water. To have a viable solution, radiation technology along with biological treatment was studied. Various experiments were conducted using chemical methods and instrumental techniques like HPLC, GC-MS, FTIR and ESI-MS to investigate the mechanism of degradation and efficiencies of the various applied methods for degradation of pollutants present in waste water. It was observed that biodegradability of the textile dye solution increased after irradiation pretreatment. This was attributed to improved efficacy of biological medium on radiation fragmented textiles dyes evidenced by enzymatic activity studies using laccase, azoreductase and tyrosinase. The results demonstrate that irradiating the RR-120 solution with a lower dose (≤ 1 kGy) and then microbial treatment of the irradiated solution with Pseudomonas *sp.* SUK1 under static condition increased the overall decolouration and degradation of RR-120 dye solution which can meet the discharge limits. The conducted toxicity tests on plant seed (*Phaseolus mungo*) using irradiated and biologically treated water samples did not alter seed germination property. Highly coloured or turbid effluents could also be treated with radiation technology with respect to the other advanced oxidation processes.

Irradiation of aromatic organic pollutants in the presence of $K_2S_2O_8$ and H_2SO_4 was found to be more effective in achieving the discharge limits of the effluents at lower radiation dose. During the radiolysis of water in presence of $K_2S_2O_8$, $SO_4^{\bullet-}$ radicals are produced in situ. The $SO_4^{\bullet-}$ radicals degrade the aromatic organic pollutants molecules via benzyl type of radicals which are generated on irradiation of the solution containing persulfate. This was evidenced by carrying out extensive studies using pulse radiolysis experiments under various radiolytic conditions. The same methodology also help in efficient degradation of ibuprofen and Nitro phenol in waste water using radiation technology.

The effluents do not contain only principal ingredients but also laden with various other additives contributing to high COD, BOD values. For the mineralization of the simulated textile effluent treatment, the equivalent oxidation capacity of radiation technology was compared with other advanced oxidation processes such as photolysis, photocatalysis and ozonolysis. The best oxidation efficiency was found for the electron beam irradiation process in the presence of $K_2S_2O_8$ compared to the other AOPs. The study infers that radiation technology can be successfully employed to degrade RR-120, IBP and 4-NP in waste water to achieve discharge limits in an effective, economic and scalable method.

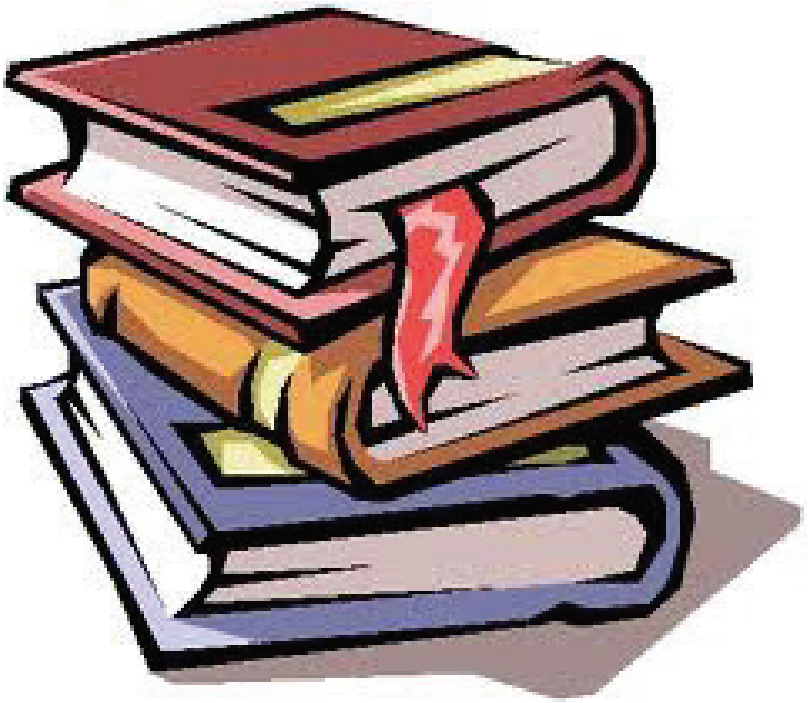

BIBLIOGRAPHY

References

1. F. Rafi, W. Franklin, C.E. Cerniglia, Azoreductase activity of anaerobic bacteria isolated from human intestinal microflora, *Appl. Environ. Microbiol.*, **56**, 1990, 2146-2151.
2. I. Arslan, I.A. Balcioglu, D.W. Bahnemann, Heterogeneous photocatalytic treatment of simulated dyehouse effluents using novel TiO_2-photocatalysts, *Appl. Catal. B: Environ.*, **26**, 2000, 193-206.
3. T. Sauer, G. Cesconet, H.J. Jose, R.F.P.M. Moreira, Kinetics of photocatalytic degradation of reactive dyes in a TiO_2 slurry reactor, *J. Photochem. Photobiol. A*, **149**, 2002, 147-154.
4. E.N. Abrahart, *Dyes and their intermediates*, 1977, New York (NY): Chemical Publishing. p. 1-12.
5. ETAD
6. J. Garcia-Montano, *Combination of advanced oxidation processes and biological treatments for commercial reactive azo dyes removal*, Ph.D. Thesis, 2007, Universitat Autonoma De Barcelona.
7. H.-Y. Shu, C.-R. Huang, Degradation of commercial ago dyes in water using ozonation and UV enhanced ozonation process, *Chemosphere*, **31**, 1995, 3813-3825.
8. H. Ollgaard, L. Frost, J. Galster, O.C. Hansen, *Survey of azo-colorants in Denmark: Consumption, use, health and environmental aspects*, Copenhagen (DK): Ministry of Environment and Energy, 1998, Danish Environmental Protection Agency.

9. H.S. Freeman, D. Hinks, J. Esancy, *Genotoxicity of azo dyes: Bases and implications*. In: A.T. Peters, H.S. Freeman (Eds), *Physico-chemical principles of color chemistry*, 1996, Advances in Color Chemistry Series, vol. 4, Blackie Academic & Professional. p. 254-292.
10. I. Arslan, I.A. Balcioglu, Degradation of commercial reactive dyestuffs by heterogenous and homogenous advanced oxidation processes: a comparative study, *Dyes Pigm.*, **43**, 1999, 95-108.
11. M. Koch, A. Yediler, D. Lienert, G. Insel, A. Kettrup, Ozonation of hydrolyzed azo dye reactive yellow 84 (CI), *Chemosphere*, **46**, 2002, 109-113.
12. R.T. Williams, *Human pharmaceuticals: Assessing the impacts on aquatic ecosystems*, Society of Environmental Toxicology and Chemistry (SETAC), 2008, p. 392.
13. M. Cleuvers, Mixture toxicity of the anti-inflammatory drugs diclofenac, ibuprofen, naproxen, and acetylsalicylic acid, *Ecotoxicol. Environ. Saf.*, **59**, 2004, 309-315.
14. S. Connors, R. Lanza, A. Sirocki, *Removal of ibuprofen from drinking water using adsorption*, 2013, Web Reports of WPI.
15. K. Fent, A. Weston, D. Caminada, Ecotoxicology of human pharmaceuticals, *Aquat. Toxicol.*, **76**, 2006, 122-159.
16. E. Zuccato, S. Castiglioni, R. Fanelli, G.Reitano, R.Bagnati, C.Chibrando, D. Calamari, Pharmaceuticals in the environment in Italy: causes, occurrence, effects and control, *Environ. Sci. Pollut. Res.*, **13**, 2006, 15-21.
17. S. Schnell, N.C. Bols, C. Barata, C. Porte, Single and combined toxicity of pharmaceuticals and personal care products (PPCPs) on the rainbow trout liver cell line RTL-W1, *Aquat. Toxicol.*, **93**, 2009, 244-252.

18. F. Mendez-Arriaga, R.A. Torres-Palmaa, C. Petriera, S. Esplugas, J. Gimenezd, C. Pulgarin, Ultrasonic treatment of water contaminated with ibuprofen, *Water Res.*, **42**, 2008, 4243-4248.

19. N. Kreuzinger, M. Clara, B. Srenn, H. Kroiss, Relevance of the sludge retention time (SRT) as design criteria for wastewater treatment plants for the removal of endocrine disruptors and pharmaceutical from wastewater, *Water. Sci. Technol.*, **50**, 2004, 149-156.

20. S. Weiss, T. Reemtsma, Membrane bioreactors for municipal wastewater treatment-available option to reduce the amount of polar pollutants discharged into surface waters, *Water Res.*, **42**, 2008, 3837-3847.

21. P.C. Kearney, D.D. Kaufman, *Herbicides: chemistry, degradation and mode of action*, 1976, Marcel Dekker. Inc., New York.

22. N.G. McCormick, F.E. Feeherry, H.S. Levinson, Microbial transformation of 2, 4, 6-trinitrotoluene and other nitroaromatic compounds, *Appl. Environ. Microbiol.*, **31**, 1976, 949-958.

23. R.P. Schwarzenbach, R. Stierli, B.R. Folsom J. Zeyer, Compound properties relevant for assessing the environmental partitioning of nitrophenols, *Environ. Sci. Technol.*, **22**, 1988, 83-92.

24. M.A. Callahan, M.W. Slimak, N.W. Gabel, J.P. May, C.F. Fowler, J.R. Freed, P. Jennings, R.L. Durfee, F.C. Whitmore, B. Maestri, W.R. Mabey, B.R. Holt, C. Gould, *Water related environmental fate of 129 priority pollutants*, 1979, EPA report-440/4-79-029. U.S. Environmental Protection Agency, Washington, D.C.

25. L.H. Keith, W.A. Telliard, Priority pollutants: I-a perspective view, *Environ. Sci. Technol.*, **13**, 1979, 416-423.

26. S. Kumar, K.G. Mukerji, R. Lai, Molecular aspects of pesticide degradation by microorganisms, *Crit. Rev. Microbiol.*, **22**, 1996, 1-26.

27. T. Golab, W.A. Allthaus, H.L. Wooten, Fate of [^{14}C]trifluralin in soil, *J. Agric. Food. Chem.*, **27**, 1979, 163-179.

28. D. Grosjean, Reactions of o-cresol and nitrocresol with NO_2 in sunlight and with ozone-nitrogen dioxide mixtures in the dark, *Environ. Sci. Technol.*, **19**, 1985, 968-974.

29. S. Basheer, *Studies on biodegradation of nitrophenol isomers by mixed bacterial cultures*, Ph. D Thesis, 2003, Fermentation Technology & Bioengineering Department Central Food Technological Research Institute, Mysore.

30. D. Georgiou, A. Aivazidis, J. Hatiras, K. Gimouhopoulas, Treatment of cotton textile wastewater using lime and ferrous sulphate, *Water Res.*, **37**, 2003, 2248-2250.

31. G.M. Shaul, C.R. Dempsey, K.A. Dostal, *Fate of water soluble azo dyes in the activated sludge process*, 1988, Water Engineering Research Laboratory, Cincinnati, OH EPA/600/S2-88/30.

32. A. Pandey, P. Singh, L. Iyengar, Bacterial decolorization and degradation of azo dyes, *Int. Biodeter. Biodegr.*, **59**, 2007, 73-84.

33. T.-H. Kim, J.-K. Lee, M.-J. Lee, Biodegradability enhancement of textile wastewater by electron beam irradiation, *Radiat. Phys. Chem.*, **76**, 2007, 1037-1041.

34. C.I. Pearce, J.R. Lloyd, J.T. Guthrie, The removal of colour from textile wastewater using whole bacterial cells: a review, *Dyes Pigm.*, **58**, 2003, 179-196.

35. F. Emami, A.R. Tehrani-Bagha, K. Gharanjig, Influence of operational parameters on the decolorization of an azo reactive dye (C.I. Reactive Red 120) by fenton process, *J. Color Sci. Tech.*, **4**, 2010, 105-114.

36. K. Singh, S. Arora, Removal of synthetic textile dyes fom wastewaters: A critical review on present treatment technologies, *Crit. Rev. Env. Sci. Tec.*, **41**, 2011, 807-878.

37. M. Neamtu, I. Siminiceanu, A. Yediler, A. Kettrup, Kinetics of decolorization and mineralization of reactive azo dyes in aqueous solution by the UV/H_2O_2 oxidation, *Dyes Pigm.*, **53**, 2002, 93-99.

38. I.-H. Cho, K.-D. Zoh, Photocatalytic degradation of azo dye (Reactive Red 120) in TiO_2/UV system: Optimization and modeling using a response surface methodology (RSM) based on the central composite design, *Dyes Pigm.*, **75**, 2007, 533-543.

39. R.V. Grieken, J. Marugán, C. Sordo, P. Martínez, C. Pablos, Photocatalytic inactivation of bacteria in water using suspended and immobilized silver-TiO_2, *Appl. Catal. B: Environ.*, **93**, 2009, 112-118.

40. P.R. Gogate, A.B. Pandit, Reviews of imperative technologies for wastewater treatment. I: oxidation technologies at ambient conditions, *Adv. Environ. Res.*, **8**, 2004, 501-551.

41. J.P. Scott, D. Ollis, Integrated chemical and biological oxidation processes for water treatment, review and recommendations, *Environ. Prog.*, **14**, 1995, 88-103.

42. M. Cerón-Rivera, M.M. Dávila-Jiménez, M.P. Elizalde-González, Degradation of the textile dyes Basic yellow 28 and Reactive black 5 using diamond and metal alloys electrodes, *Chemosphere*, **55**, 2004, 1-10.

43. M. Muthukumar, D. Sargunamani, M. Senthilkumar, N. Selvakumai, Studies on decolouration, toxity and the possibility for recycling of acid dye effluents using ozone treatment, *Dyes Pigm.*, **64**, 2005, 39-44.

44. J. Gonzalez-Garcia, V. Saez, I. Tudela, M.I. Díez-Garcia, M. D. Esclapez, O. Louisnard, Sonochemical treatment of water polluted by chlorinated organo compounds. A Review, *Water*, **2**, **2010**, 28-74.

45. A.O. Ibhadon, P. Fitzpatrick, Heterogeneous photocatalysis: recent advances and applications, *Catalysts*, **3**, 2013, 189-218.

46. B. Kasprzyk-Hordern, M. Ziołek, J. Nawrocki, Catalytic ozonation and methods of enhancing molecular ozone reactions in water treatment, *Appl. Catal. B: Environ.*, **46**, 2003, 639-669.

47. J.W.T. Spinks, R.J. Woods, *An Introduction to radiation chemistry*, Third Edition, 1990, John Wiley and Sons, New York.

48. J.H. Baxendale, F. Busi (eds), *The study of fast processes and transient species by electron pulse radiolysis*, 1982, Reidel, Dordrecht.

49. Farhathaziz, M.A.J. Rodgers (eds), *Radiation chemistry: Principle and application*, 1987, VCH, New York.

50. H.A. Bethe, J. Ashkin, *Experimental Nuclear Physics*, Vol. 1, E. Segre (Ed.), 1953, Wiley, New York, pp.166-357.

51. N.W. Hölm, *Radiation Dosimetry*, F.H. Attix, E. Tochilin (Eds.), Vol. 3, 1969, Academic, New York, Chapter 33.

52. G.V. Buxton, C.L. Greenstock, W.P. Hellman, A.B. Ross, Critical review of rate constants for reactions of hydrated electrons, hydrogen atoms and hydroxyl radicals in aqueous solution, *J. Phys. Chem. Ref. Data*, **17**, 1988, 513-886.

53. E. Hayon, J.J. Weiss, Proc. Second U.N. Conference on Peaceful Uses of Atomic Energy, Geneva, **29**, 1959, 80.

54. E. J. Hart, J.W. Boag, Absorption spectrum of the hydrated electron in water and in aqueous solutions, *J. Amer. Chem. Soc.*, **84**, 1962, 4090-4095.

55. M.S. Matheson, L.M. Dorfman, *Pulse radiolysis*, 1969, M.I.T. Press, Cambridge, Mass.

56. G.V. Buxton, *Radiation Chemistry; Principles and Application*, 1987, Farhataziz, M.A.J. Rodgers (Eds), VCH, Weinheim, p. 341.

57. H.A. Schwarz, R.W. Dosdson, Equilibrium between hydroxyl radicals and thallium(II) and the oxidation potential of OH(aq), *J. Phys. Chem.*, **88**, 1984, 3643-3647.

58. P. Pagsberg, H. Christensen, J. Rabani, G. Nilsson, J. Fenger, S.O. Nielsen, Far-ultraviolet spectra of hydrogen and hydroxyl radicals from pulse radiolysis of aqueous solutions. Direct measurement of the rate of H + H, *J. Phys. Chem.*, **73**, 1969, 1029-1038.

59. E. M. Fielden, in *The Study of Fast Processes and Transient Species by Electron Pulse Radiolysis*, J.H. Baxendale, F. Busi (Eds.), 1982, Riedel, United States, p. 59.

60. L.D. Margerum, R.W. Murray, T.J. Meyer, Transient storage of photochemically produced oxidative and reductive equivalents in soluble redox polymers, *J. Phys. Chem.*, **90**, 1986, 728-730.

61. K.S.S. Sarma, S.A. Khader, M. Assadullah, S. Sabharwal, L.N. Bandi, D.S. Lavale, 2 MeV Electron Beam Accelerator at Navi Mumbai-A status Report on the facility characteristics and material processing, *Proc. DAE-BRNS Indian Particle Accelerator Conference* 2003, Indore, Feb. 2003, pp. 292-293.

62. P.G. Benny, T. P. Selvam, K.S.S. Sarma, Comparison of graphite calorimeter dosimetry system with Monte Carlo simulation at an industrial electron beam accelerator, *Nucl. Instrum. Meth. A*, **703**, 2013, 98-101.

63. A.J. Swallow, *Radiation Chemistry: An introduction*, Longman, 1973, London.

64. H. Chen, S. Hopper, C. Cerniglia, Biochemical and molecular characterization of an azoreductase from Staphylococcus aureus, a tetrameric NADPH-dependent flavoprotein, *Soc. Gen. Microbiol.*, **151**, 2005, 1433-1441.

65. H.W. Duckworth, J.E. Coleman, Physicochemical and kinetic properties of mushroom tyrosinase, *J. Biol. Chem.*, **245**, 1970, 1613-1625.

66. S.D. Kalme, G.K. Parshetti, S.U. Jadhav, S.P. Govindwar, Biodegradation of benzidine based dye Direct Blue-6 by Pseudomonas desmolyticum NCIM 2112, *Bioresour. Technol.*, **98**, 2007, 1405-1410.

67. M. Salokhe, S. Govindwar, Effect of carbon source on the biotransformation enzymes in Serratiamarcescens, *World J. Microbiol. Biotechol.*, **15**, 1999, 229-232.

68. W. Feng, D. Nansheng, H. Helin, Degradation mechanism of azo dye C.I. reactive red 2 by iron powder reduction and photooxidation in aqueous solutions, *Chemosphere*, **41**, 2000, 1233-1238.

69. K.K. Sharma, P. O'Neill, J. Oakes, S.N. Batchelor, B.S.M. Rao, One-electron oxidation and reduction of different tautomeric forms of azo dyes: a pulse radiolysis study, *J. Phys. Chem. A*, **107**, 2003, 7619-7628.

70. L. Wojnarovits, T. Palfi, E. Takacs, S.S. Emmi, Reactivity differences of hydroxyl radicals and hydrated electrons in destructing azo dyes, *Radiat. Phys. Chem.*, **74**, 2005, 239-246.

71. N.K. Vel-Leitner, P. Beger, P. Gehringer, γ- irradiation for the removal of atrazine in aqueous solution containing humic substances, *Radiat. Phys. Chem.*, **55**, 1999, 317-322.

72. C.C.I. Guaratini, A.G. Fogg, M.V.B. Zanoni, Assessment of the application of cathodic stripping voltammetry to the analysis of diazo reactive dyes and their hydrolysis products, *Dyes Pigm.*, **50**, 2001, 211-221.

73. C.M. Foldvary, L. Wojnarovits, Role of reactive intermediates in the radiolytic degradation of Acid Red 1 in aqueous solution, *Radiat. Phys. Chem.*, **78**, 2009, 13-18.

74. M. Wang, R. Yang, W. Wang, Z. Shen, S. Bian, Z. Zhu, Radiation-induced decomposition and decolouration of reactive dyes in the presence of H_2O_2, *Radiat. Phys. Chem.*, **75**, 2006, 286-291.

75. A. Telke, D. Kalyani, J. Jadhav, S. Govindwar, Kinetics and mechanism of Reactive Red 141 degradation by a bacterial isolate Rhizobium radiobacter MTCC 8161, *Acta Chim. Slov.*, **55**, 2008, 320-329.

76. R.G. Saratale, G.D. Saratale, J.S. Chang, S.P. Govindwar, Bacterial decolorization and degradation of azo dyes: a review, *J. Taiwan Inst. Chem. Engrs.*, **42**, 2011, 138-157.

77. J. Garcia-Montano, F. Torrades, J.A. Garcia-Hortal, X. Domenech, J. Peral, Combining photo-Fenton process with aerobic sequencing batch reactor for commercial hetero-bireactive dye removal, *Appl. Catal. B: Environ.*, **67**, 2006, 86-92.

78. B. Han, J. Ko, J. Kim, Y. Kim, W. Chung, I.E. Makarov, A.V. Ponomarev, A.K. Pikaev, Combined electron-beam and biological treatment of dyeing

complex wastewater. Pilot plant experiments, *Radiat. Phys. Chem.*, **64**, 2002, 53-59.

79. B. Han, J.K. Kim, Y. Kim, J.S. Choi, K.Y. Jeong, Operation of industrial-scale electron beam wastewater treatment plant, *Radiat. Phys. Chem.*, **81**, 2012, 1475-1478.
80. V.K. Garg, P. Kaushik, Influence of textile mill wastewater irrigation on the growth of sorghum cultivars, *Appl. Ecol. Environ. Res.*, **6**, 2008, 1-12.
81. J.P. Jadhav, G.K. Parshetti, S.D. Kalme, S.P. Govindwar, Decolourization of azo dye Methyl Red by Saccharomyces cerevisiae MTCC 463, *Chemosphere*, **68**, 2007, 394-400.
82. J.P. Jadhav, D.C. Kalyani, A.A. Telke, S.S. Phugare, S.P. Govindwar, Evaluation of the efficacy of a bacterial consortium for the removal of color, reduction of heavy metals, and toxicity from textile dye effluent, *Bioresour. Technol.*, **101**, 2010, 165-173.
83. A. Aleboyeh, H. Aleboyeh, Y. Moussa, Critical effect of hydrogen peroxide in photochemical oxidative decolorization of dyes: Acid Orange 8, Acid Blue 74 and Methyl Orange, *Dyes Pigments*, **57**, 2003, 67-75.
84. J.T. Spadaro, L. Isabelle, V. Renganathan, Hydroxyl radical mediated degradation of azo dyes: evidence for benzene generation, *Environ. Sci. Technol.*, **28**, 1994, 1389–1393.
85. S. Hammamia, N. Bellakhal, N. Oturan, M.A. Oturan, M. Dachraoui, Degradation of Acid Orange 7 by electrochemically generated $^{\bullet}$OH radicals in acidic aqueous medium using a boron-doped diamond or platinum anode: a mechanistic study, *Chemosphere*, **73**, 2008, 678-684.

86. M.M. Tauber, G.M. Gubitz, A. Rehorek, Degradation of azo dyes by oxidative processes – laccase and ultrasound treatment, *Bioresour. Technol.*, **99**, 2008. 4213-4220.

87. N. Dura, M.A. Rosa, A.D. Annibale, L. Gianfreda, Applications of laccases and tyrosinases (phenoloxidases) immobilized on different supports: a review, *Enzyme Microb. Technol.*, **31**, 2002, 907-931.

88. A. Stolz, Basic and applied aspects in the microbial degradation of azo dyes, *Appl. Microbiol. Biotechnol.*, **56**, 2001, 69-80.

89. I. Arslan, Treatability of a simulated disperse dye-bath by ferrous iron coagulation, ozonation, and ferrous iron-catalyzed ozonation, *J. Hazard. Mater.*, **85**, 2001, 229-241.

90. I. Arslan-Alanton, I. Alaton, Degradation of xenobiotics originating from the textile preparation, dyeing, and finishing industry using ozonation and advanced oxidation, *Ecotoxicol. Environ. Saf.*, **68**, 2007, 98-107.

91. R.O. Cristovao, A.P.M. Tavares, J.M. Loureiro, R.A.R. Boaventura, E.A. Macedo, Treatment and kinetic modelling of a simulated dye house effluent by enzymatic catalysis, *Bioresour. Technol.*, **100**, 2009, 6236-6242.

92. U.G. Akapon, B.H. Hameed, Parameters affecting the photocatalytic degradation of dyes using TiO_2-based photocatalysts: A review, *J. Hazard. Mater.*, **170**, 2009, 520-529.

93. C. Jiang-Lin, L. Wen-Hua, Z. Jian-Qing, C. Chu-Nan, Adsorption Behavior and Photooxidation Kinetics of OH^- at TiO_2 Thin Film Electrodes, *Acta Phys.-Chim. Sin.*, **20**, 2004, 735-739.

94. J. Hoigne, H. Bader, The role of hydroxyl radical reactions in ozonation processes in aqueous solutions, *Water Res.*, **10**, 1976, 377-386.

95. J. Paul (Guin), D.B. Naik, Y.K. Bhardwaj, L. Varshney, Studies on oxidative radiolysis of ibuprofen in presence of potassium persulfate, *Radiat. Phys. Chem.*, **100**, 2014, 38-44.

96. R.V. Bensasson, E.J. Land, T.G. Truscott, *Flash Photolysis and Pulse Radiolysis*, Pergamon Press, Oxford, 1983, pp. 1-19.

97. J. Paul, D.B. Naik, S. Sabharwal, High energy induced decoloration and mineralization of Reactive Red 120 dye in aqueous solution: A steady state and pulse radiolysis study, *Radiat. Phys. Chem.*, **79**, 2010, 770-776.

98. S. Liang, H.-W. Su, Identification of sulfate and hydroxyl radicals in thermally activated persulfate, *Ind. Eng. Chem. Res.*, **48**, 2009, 5558- 5562.

99. J. Criquet, N.K.V. Leitner, Radiolysis of acetic acid aqueous solutions-Effect of pH and persulfate addition, *Chem. Eng. J.*, **174**, 2011, 504-509.

100. P. Canizares, R. Paz, C. Saez, M.A. Radrigo, Costs of the electrochemical oxidation of wastewaters: A comparison with ozonation and Fenton oxidation processes, *J. Environ. Manage.*, **90**, 2009, 410-420.

101. J. Mendez-Diaz, M. Sanchez-Polo, J. Rivera-Utrilla, S. Canonica, U. V. Gunten, Advanced oxidation of the surfactant SDBS by means of hydroxyl and sulphate radicals, *Chem. Eng. J.*, **163**, 2010, 300-306.

102. L. Osiewala, A. Socha, M. Wolszczak, J. Rynkowski, Radiolysis of sodium p-cumenesulfonate in aqueous solution, *Radiat. Phys. Chem.*, **87**, 2013, 71-81.

103. S.M. Dockheer, L. Gubler, W.H. Koppenol, Reactions of the tetraoxidosulfate(•) and hydroxyl radicals with poly(sodium α-methylstyrene sulfonate), *Phys. Chem. Chem. Phys.*, **15**, 2013, 4975-4983.

104. P. Neta, V. Madhavan, H. Zemel, R.W. Fessenden, Rate constants and mechanism of reaction of $SO_4^{\bullet-}$ with aromatic compounds, *J. Am. Chem. Soc.*, **99**, 1977, 163-164.

105. H. Zemel, R.W. Fessenden, The mechanism of reaction of $SO_4^{\bullet-}$ with some derivatives of benzoic acid, *J. Phys. Chem.*, **82**, 1978, 2670-2676.

106. S. Venu, D.B. Naik, S.K. Sarkar, U.K. Aravind, A. Nijamudheen, C.T. Aravindakumar, Oxidation reactions of thymol: A pulse radiolysis and theoretical study, *J. Phys. Chem. A*, **117**, 2013, 291-299.

107. J. Criquet, N.K.V. Leitner, Degradation of acetic acid with sulfate radical generated by persulfate ions photolysis, Chemosphere, **77**, 2009, 194-200.

108. I. Grcic, S. Papic, N. Koprivanak, I. Kovacic, Kinetic modeling and synergy quantification in sono and photooxidative treatment of simulated dyehouse effluent, *Water Res.*, **46**, 2012, 5683-5695.

109. M.F. Desrosiers, J.M. Puhl, Absorbed-dose/dose-rate dependence studies for the alanine-EPR dosimetry system, *Radiat. Phys. Chem.*, **78**, 2009, 461-463.

110. L.A.W. Abdou, O.A. Hakeim, M.S. Mahmoud, A.M. El-Naggar, Comparative study between the efficiency of electron beam and gamma irradiation for treatment of dye solutions, *Chem. Eng. J.*, **168**, 2011, 752-758.

111. Y. Guo, J. Zhou, X. Lou, R. Liu, D. Xiao, C. Fang, Z. Wang, J. Liu, Enhanced degradation of Tetrabromobisphenol A in water by a UV/base/persulfate system: Kinetics and intermediates, *Chem. Eng. J.*, **254**, 2014, 538-544.

112. J.C. Kruithof, IUVA News, **7**, 2005, 17-20.

113. B.J. Martijn, P.C. Kamp, J.C. Kruithof, *UV/H_2O_2 treatment an essential barrier in a multi barrier approach for organic contaminant control*, PWN Publications, http://www.pwntechnologies.nl/resources/ papers.

114. B.J. Martijn, J.C. Kruithof, L.P.M. Rosenthal, *Design and implementation of UV/H_2O_2 treatment in a full scale drinking water treatment plant*, PWN Publications, http://www.pwntechnologies.nl/resources/papers.

115. G.F. Ijpelaar, D.J.H. Harmsen, M. Heringa, *Techneau Report*, D2.4.1.1, May, 2007.

116. IAEA Scientific Report, *Radiation Processing : Environmental Applications*, 2007, ISBN 92-0-100507-5, IAEA, Vienna.

117. IAEA Scientific Report, *Radiation Treatment of Polluted Water and Wastewater*, 2008, IAEA-TECHDOC-1598, IAEA, Vienna.

118. W.J. Cooper, R.D. Curry, K.E. O'Shea, *Environmental applications of ionizing radiation*, John Wiley, 1998.

119. Y.A. Maruthi, N.L. Das, K. Hossain, K.S.S. Sarma, K.P. Rawat, S. Sabharwal, Disinfection and reduction of organic load of sewage water by electron beam radiation, *Afr. J. Environ. Sci. Technol.*, **5**, 2011, 545-552.

120. S. Zhao, H. Ma, M. Wang, C. Cao, S. Yao, Study on the role of hydroperoxyl radical in degradation of p-nitrophenol attacked by hydroxyl radical using photolytical technique, *J. Photoch. Photobio. A Chem.*, **259**, 2013, 17-24.

121. A. Streitwieser (Jr.), R.W. Taft (Editors); *Progress in Physical Organic Chemistry*, Vol. 7; John Wiley and Sons, Inc., 1970, USA, pp. 229-335.

122. B. Cercek, M. Ebert, Radiolytic transients from p-nitrophenol and their inter- and intramolecular reactions, *Adv. Chem. Ser.*, **81**, 1968, 210-221.

123. H.J.V. Linde, A pulse radiolytic study of aqueous nitroaniline solutions, *Radiat. Phys. Chem.*, **10**, 1977, 199-206.

124. P. Neta, J. Grodkowski, Rate Constants for Reactions of Phenoxyl Radicals in Solution, *J. Phys. Chem. Ref. Data*, **34**, 2005, 109-199.

125. E. Illes, E. Takacs, A. Dombi, K. Gajda-Schrantz, G. Racz, K. Gonter, L. Wojnarovits, Hydroxyl radical induced degradation of ibuprofen, *Sci. Total Environ.*, **447**, 2013, 286-292.

.....The End